Generation of dense plasmas and strong currents with intense, ultra-short laser pulses

Habilitationsschrift

Jens Osterholz

Heinrich-Heine-Universität Düsseldorf
Februar 2009

Abstract

The physics of dense plasmas is an important field of research with relevance to applied and fundamental science. Due to the rapid progress in laser technology, novel experiments investigating the properties of dense plasmas in the laboratory have become possible in the recent years. Although these experiments have strongly contributed to our understanding of the physics of dense plasmas, there are still many open questions.

In the first part of this work, radiative properties and the equation of state (EOS) of dense plasmas with relevance to astrophysics and fusion research are investigated. Thin layers of dense plasmas with temperatures of 200 eV are produced by isochoric heating of solids with high contrast, sub-10-fs laser pulses. The XUV emission from the plasmas generated from different target materials is analyzed in detail. Separate absorption measurements confirm a plasma scale length of the order of one nanometer during the interaction. The thickness of the plasma layer of about 10 nm is limited by the penetration depth of the laser into the solid target. For the production of thicker samples, a second method based on isochoric heating with laser driven proton beams is pursued. Dense plasmas with a temperature of 20 eV are produced. In the experiments, the expansion and the temperature of the plasma are measured with high temporal resolution. In this way, the EOS along the release isentrope is derived.

In the second part of this work, the generation and the transport of strong currents of laser driven, relativistic electron beams, which are important in fusion research and ultra-fast x-ray science, are investigated over a wide range of experimental parameters. This includes experiments with very short laser pulses with a duration of only 40 fs and very intense pulses with a power in the petawatt regime. Depending on the experimental conditions, different acceleration mechanisms are identified. The effects of self-generated magnetic fields and instabilities are analyzed. Special attention is given to the optimization of the target design for the generation of high electron fluxes. Different types of cone targets are investigated. The potential of these targets for a controlled transport of the electron beams is demonstrated.

Zusammenfassung

Die Physik dichter Plasmen ist ein wichtiges Forschungsgebiet mit Relevanz für die angewandte Wissenschaft und die Grundlagenforschung. Aufgrund der großen Fortschritte in der Lasertechnologie sind in den vergangenen Jahren völlig neuartige Experimente zur Untersuchung dichter Plasmen im Labor möglich geworden. Obwohl solche Experimente stark zu unserem Verständnis dichter Plasmen beigetragen haben, sind viele Fragen noch nicht hinreichend beantwortet.

Im ersten Teil dieser Arbeit werden die Emission von XUV Strahlung und die Zustandsgleichung dichter Plasmen, wie sie in der Astrophysik und in der Fusionsforschung von Bedeutung sind, untersucht. Dünne Schichten dichter Plasmen mit einer Temperatur von 200 eV werden durch isochores Heizen von Festkörpern mit sub-10-fs Laserpulsen mit einem hohen Kontrast erzeugt. Die XUV Emission dieser Plasmen wird im Detail analysiert. Separate Absorptionsmessungen bestätigen eine extrem kleine Skalenlänge in der Größenordnung von einem Nanometer während der Wechselwirkung.

Zur Erzeugung dichter Plasmen mit größeren Schichtdicken und mit Temperaturen von bis zu 20 eV wird ein zweites Verfahren, basierend auf isochorem Heizen mit Laser-getriebenen Protonenstrahlen, angewandt. Die Expansion und die Temperatur werden mit hoher Zeitauflösung gemessen. Auf diese Weise wird die Zustandsgleichung entlang der Expansions-Isentropen ermittelt.

Im zweiten Teil dieser Arbeit werden die Erzeugung und der Transport starker, Laser getriebener Ströme von relativistischen Elektronen, wie sie in der Fusionsforschung und bei der Entwicklung schneller Röntgenquellen von großer Bedeutung sind, über einen großen Bereich experimenteller Parameter untersucht. Dazu gehören Versuche mit sehr kurzen Laserpulsen mit einer Dauer von nur 40 fs und mit sehr intensiven Pulsen mit Leistungen im Petawatt Bereich. In Abhängigkeit von den experimentellen Bedingungen werden verschiedene Beschleunigungsmechanismen beobachtet. Der Einfluss von selbst-generierten magnetischen Feldern und Instabilitäten wird untersucht. Besondere Aufmerksamkeit wird der Optimierung der Targets für die Erzeugung starker Flussdichten von Elektronen gewidmet. Dazu werden verschiedene Arten von konischen Targets verwendet. Das Potenzial dieser Targets für einen kontrollierten Transport von hochenergetischen Elektronenstrahlen wird demonstriert.

Contents

1 Introduction

The physics of dense plasmas has become a major field of research with increasing interest over the past years. A detailed understanding of the physics of dense plasmas is crucial, e.g., in astrophysics, fusion research and the development of ultrafast x-ray sources. Radiative properties of dense plasmas play an important role for the energy transport in the interior of stars. The generation and the transport of strong currents in dense plasmas are crucial in the fast ignitor scheme of inertial confinement fusion. Ultrashort x-ray flashes produced in dense plasmas allow for the observation of fast processes in crystallographic structures with an unprecedented time resolution.

Many laboratory experiments investigating dense plasmas have become possible due to the tremendous progress in the development of high power laser systems in the recent decades. The radiative properties and the equations of state of matter were investigated under conditions found in the interior of stars or giant planets. The complex processes involved in the transport of high currents of electrons in dense plasmas were studied. Advanced target geometries were developed to control the propagation of the electron beams and to produce high fluxes of electrons.

In the recent years, these experiments have greatly contributed to the understanding of high energy density matter. Important scaling laws and numerous processes involved in the interaction of intense laser pulses with dense plasmas have been identified. However, a large number of phenomena are not yet fully understood, and there are still many open questions. In this work, important novel aspects of the physics of dense plasmas with relevance to astrophysics, fusion research, atomic physics and ultrafast x-ray science are investigated. Novel techniques generating dense plasmas for measurements of radiative properties and equations of state are presented. The generation and transport of strong currents in laser irradiated solids is studied in great detail over a wide range of parameters.

This work is organized as follows: In Chapter 2, some examples highlighting the role of the physics of dense plasmas for applied and fundamental science is discussed. In

Chapter 3, the potential of different classes of laser systems for the production of dense plasmas and strong currents is investigated. Chapter 4 is an introduction to the interaction of intense laser pulses with matter. The experimental results are presented in the Chapters 5 and 6.

In Chapter 5, radiative properties and the equation of state of dense plasmas are investigated. Two novel methods for the production of dense plasmas in different physical regimes are presented. The first method is based on isochoric heating of solid targets by direct irradiation with few-cycle, high contrast laser pulses. Dense plasmas with temperatures of about 200 eV are produced. XUV spectra obtained from different target materials are analyzed in detail. In the second method, dense plasmas are generated by isochoric heating of solids with laser-driven proton beams. Equation of state measurements are demonstrated for dense aluminium plasmas with temperatures of about 20 eV.

In Chapter 6, the generation of strong currents in laser irradiated solids is investigated over a wide range of experimental parameters. The transport of the electron beams in dense plasmas is characterized in great detail. Special attention is given to the optimization of the target for a controlled transport of high electron fluxes relevant for laser driven x-ray sources and fusion research.

The work closes with a summary and an outlook in Chapter 7.

2 The physics of dense plasmas

The physics of dense plasmas has gained an enormous interest due to its relevance to fundamental and applied science. The goal of this chapter is to highlight important aspects of this field of research. The role of dense plasmas for topical research is discussed in the context of ultrafast x-ray science, astrophysics, warm dense matter and inertial confinement fusion.

2.1 Astrophysics

Dense plasmas are found in the interior of stars, giant planets, brown dwarfs and accretion discs. As the inner structure of astronomic objects is not directly accessible, our models rely to the most part on computer simulations. Parameters such as the opacity and the equation of state (EOS) are required as an input for these calculations. In the recent years, laboratory experiments measuring these quantities in laser produced, dense plasmas have become an important tool for astrophysics.

To discuss the relevance of the EOS in the context of astrophysics, the phase diagram of hydrogen calculated with the free energy model as described in [202] is shown in Fig. 2.1. Model calculations of the temperature-pressure profiles of Jupiter, a brown dwarf and a dwarf star are indicated by the dotted lines. Jupiter has an outer shell of molecular H_2. The pressure in the center of Jupiter is assumed to be 40 Mbar at a temperature of a few eV. It is believed that there is a transition to metallic hydrogen at $r=0.75R_J$ (R_J: Jupiter radius) at a pressure of approximately 2 Mbar. In the computer models, the dimension of the boundary between the molecular hydrogen mantle and nonatomic core plays an important role. A sharp boundary caused by a first order phase transition would reduce the convective heat transfer and thus result in a higher core temperature in the computer models. In addition, the position of the boundary is relevant for the magnetic field which is generated by currents in the planet’s interior. Because the currents cannot be transported in the molecular hydrogen mantle, the position of the boundary determines which part of the planet contributes to the magnetic field generation.

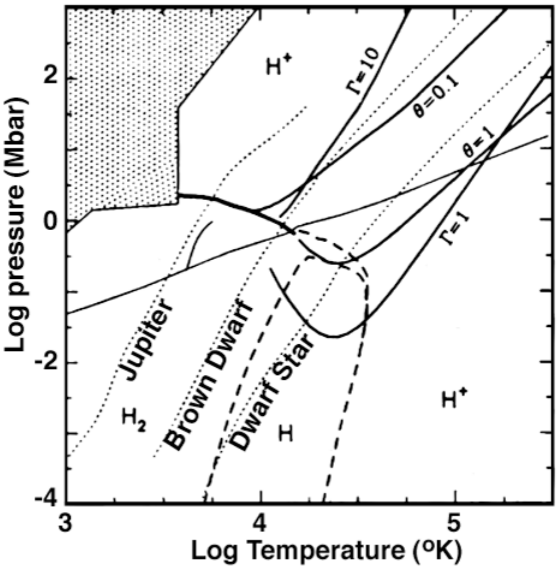

Fig. 2.1: *Phase diagram of hydrogen calculated with the free energy model [202]. The temperature-pressure profiles of Jupiter, a brown dwarf and a dwarf star are indicated by the dotted lines. In addition, curves of constant coupling parameter Γ and degeneracy parameter θ (see Chapter 2.2) are shown. The regions dominated by molecular, atomic and ionized hydrogen are indicated by the dashed lines corresponding to 50% dissociation or ionization. Plot from Reference [202].*

Besides the EOS, the opacity of dense plasmas, defined as a weighted average of the absorption coefficient, is an important parameter in astrophysics. Fig. 2.2 shows the inner structure of the sun [212]. The core is surrounded by the radiative zone and the convective zone. The energy transport in the radiative zone is basically through high energetic photons in the XUV and x-ray spectral range and is determined by the opacity of the stellar matter in this region.

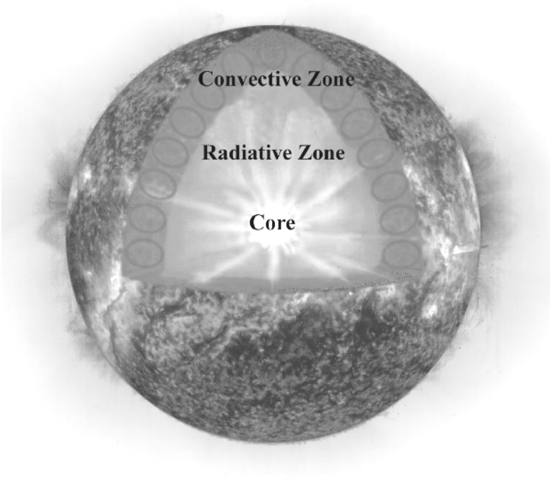

Fig. 2.2: *Schematic drawing of the interior of the sun. The core is surrounded by the radiative zone and the convective zone. The energy transport in the radiative zone is determined by the opacity of the stellar matter in this region. Image from Reference [212].*

The opacity is related to a number of radiative transitions, where the electrons final and initial states can be free-free, bound-free or bound-bound. Historically, early models have neglected the contribution of bound-bound transitions to the opacity because their calculation is complex due to the large number of atomic levels involved. However, a closer analysis has revealed that bound-bound transitions become important in regions where the plasma is only partially ionized. For the heavier elements, e.g. iron, this is the case throughout the whole radiative zone down to the core. A first attempt to account for the bound-bound transitions resulted in the Los Alamos Astrophysical Opacity Library [111] which was to a large extent based on detailed configuration accounting (DCA) methods. More precise calculations with improved EOS and atomic physics were carried out at Lawrence Livermore National Laboratory within the OPAL project [114, 115] and more recently by the Opacity Project (OP) [205]. These projects were carried out in close collaboration with laboratory experiments and have contributed to a more detailed understanding of astrophysics. This is illustrated in Fig. 2.3, showing experimental data of the XUV transmission through a laser produced iron plasma and results from DCA and OPAL calculations [186].

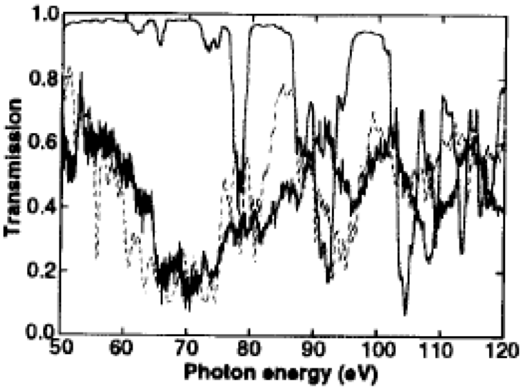

Fig. 2.3: *Transmission of XUV radiation through an iron plasma in the energy range between 50 and 120 eV [186]. Fat solid line: Experiment with laser-produced iron plasma. Dashed line: OPAL calculation. Solid line: DCA calculation. The experiment is in good agreement with the OPAL calculation. The iron opacity plays an important role in the cycle of some variable stars. Plot from Reference [186].*

In Fig. 2.3, there is a good overall agreement between the experimental data and the OPAL calculations, whereas it significantly deviates from the DCA calculations.

The opacities are closely related to the pulsation of some variable stars such as the Cepheids. When there is a sharp increase of opacity with temperature, the contraction of a star leads to an increase of the opacity in the radiation zone. The energy will be trapped in the center, resulting in an increase of temperature and pressure, and finally leading to expansion and an increase of brightness. As the star expands, it cools down and falls back through its equilibrium state through the gravitational forces. The OPAL opacities have rendered possible detailed understanding of the Cepheid periods. These examples demonstrate the potential of laboratory experiments for astrophysics.

2.2 Warm dense matter

The term warm dense matter (WDM) is used for matter at the convergence of condensed matter and dense plasma. WDM states are relevant in astrophysics, planetary physics and inertial confinement fusion. The WDM regime ranges roughly from temperatures between 1 and 100 eV and from densities between 0.1 and 10 times solid. A definition of WDM is sometimes given in terms of the ion-ion coupling parameter Γ_{ii} and the degeneracy parameter θ. The ion-ion coupling parameter is defined as the ratio of the average Coulomb energy to the kinetic energy of the ions in the plasma. For an one-component plasma, it is obtained [113]

$$\Gamma_{ii} = \frac{(Ze)^2}{r_i k T_i} \ . \tag{2.1}$$

Here, Ze is the ion charge, k is the Boltzmann constant, T_i is the ion temperature, $r_i = (4\pi n_i/3)^{-1/3}$ is the ion sphere radius and n_i is the ion density. The degeneracy parameter, defined as the ratio of the electron temperature to the Fermi temperature $E_F = \hbar^2\,(3\pi^2 n_e)^{2/3}/(2m_e)$, is

$$\theta = \frac{kT_e}{E_F} \ . \tag{2.2}$$

Here, $\hbar = h/2\pi$, h is the Planck constant, m_e is the electron mass, T_e is the electron temperature and n_e is the electron density. In WDM states, the coupling parameter Γ_{ii} is typically close to or larger than unity and the degeneracy parameter θ is close to 1. The first condition means that the plasma ions are strongly coupled, whereas the second condition indicates that the electrons are in a partially degenerate state.

As an example, the diagram in Fig. 2.4 shows lines of constant values of the ion-ion coupling parameters (Γ_{ii}=1, 10 and 100, respectively) in density-temperature space for aluminium. The dashed blue line indicates a temperature equal to the Fermi temperature, i.e. θ=1. The WDM regime is highlighted in grey. The values of Γ_{ii} and θ were calculated based on a quotidian equation of state [125].

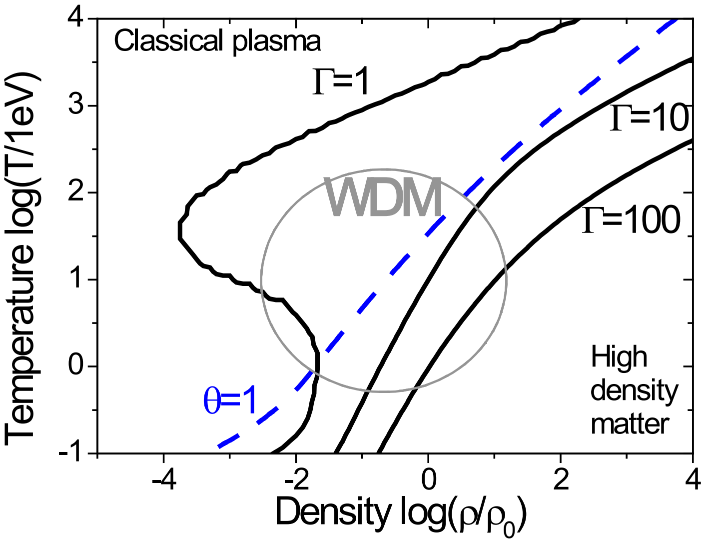

Fig. 2.4: *Density-temperature phase diagram of aluminium. The solid black lines indicate constant values of the ion-ion coupling parameter (Γ_{ii}=1, 10 and 100, respectively). The dashed blue line represents a constant value of the degeneracy parameter of θ=1. The position of the warm dense matter regime in density-temperature space is highlighted.*

The number of electrons in the Debye sphere $N_D = (4/3)\pi n_e \lambda_D^3$ is an important scaling parameter in classical plasma physics [134]. Here, $\lambda_D = (\varepsilon_0 kT/e^2 n_e)^{1/2}$ is the Debye length and n_e is the electron density. When the number of electrons in the Debye sphere is large, i.e.

$$N_D \gg 1 \quad , \tag{2.3}$$

the Coulomb interaction between particles can be treated perturbatively, and collisions between particles are uncorrelated. The reciprocal value, $1/N_d$, is an important expansion parameter in this perturbative approach.

In strongly coupled plasmas, the number of electrons in the Debye sphere is small, and the Coulomb interaction cannot be treated perturbatively, anymore. The numerical treatment is complex because correlations between particles become important, and the plasma exhibits short range order. Because the temperature of WDM states is close to the Fermi temperature (θ~1), excited states are significantly populated, in contrast to condensed matter where θ<<1. Quantum effects are important because the free electrons are partially degenerate. Under these conditions, classical plasma physics and condensed matter physics fail to describe WDM states, and new approaches are required. Although a number of theoretical models have been developed [113], a closed description over the whole WDM parameter range is not yet available.

Besides the complexity of the theoretical treatment of WDM, it turns out that experiments are challenging. Measurements in this regime require the preparation of WDM states under well-defined conditions. Experimental methods for the generation of WDM states include strong shocks [53], isochoric heating with laser [170] or particle beams [171], quasi-isentropic compression [63] and static compression in conjunction with laser heating [69]. Although experiments have strongly contributed to gain some insight into the nature of WDM, comprehensive studies over the whole range of temperatures and densities are still missing.

2.3 Inertial confinement fusion

The concept of inertial confinement fusion driven by intense laser beams was published for the first time in 1972 [167]. The idea is to compress a millimeter scale spherical pellet filled with a fuel consisting of deuterium and tritium by symmetrically focusing laser beams onto its surface. Due to the thermal pressure, the shell is rapidly ablated, driving spherically converging shocks to the center of the pellet. Provided that high densities and temperatures can be achieved, the conditions for thermonuclear fusion will be reached.

More than three decades of research have revealed that the realization of this concept poses enormous requirements on the driving laser energy and symmetry [149,150]. A number of issues making the compression less efficient have not been considered in the original work. Today, in most laboratories the hot-spot scenario is pursued where the nuclear burn will be ignited in a small volume in the center of the pellet [8]. It is estimated that a positive energy gain in a fusion pellet requires driving laser energies in the order of 1 Megajoule. Two laser systems capable of delivering this enormous energy on a nanosecond scale are currently under construction.

The fast ignitor (FI) scheme was suggested to reduce the requirements of the driving laser by generating the hot-spot with an additional external energy source. In the FI scheme in Reference [222], it is proposed to transport the energy into the compressed core by a laser-driven electron beam. In the first step, the pellet is compressed to a density of 300 g/cm^3. In the second step, a laser pulse with a duration of several 100 picoseconds drills a channel into the corona to the compressed core. In the third step, another laser pulse with an intensity in the petawatt regime propagates through the channel and generates a population of electrons with a temperature of about 1 MeV. The electrons are stopped by collisions in the compressed core and generate a hot-spot with a temperature of 5-10 keV. A closer analysis has shown that a huge energy of about 20 kJ has to be transported by the electron beam [7]. This energy translates into an enormous current of 1 GA. The transport of such strong currents exceeding the Alfvén limit is widely unexplored. It is assumed that currents above the Alfvén limit can be transported in plasma when the self-generated magnetic fields are compensated by counter propagating currents. However, this configuration of two counter propagating currents is susceptible to instabilities, which can dramatically affect the transport of the electron beam.

To avoid some of these issues, alternative FI schemes have been proposed. A promising approach is the concept of cone guiding. As shown in Fig. 2.5, a re-entrant cone is attached to the fusion pellet. The population of hot electrons required to produce the hot-spot are generated by a laser beam focused into the cone. It has been demonstrated that high fluxes of electrons can be achieved at the tip of the cone [133]. This effect is related to optical guiding of the laser pulse and guiding of the electrons by the electric sheath fields and the self-generated magnetic fields at the inner cone surfaces. Cone guided fast ignition does not require a laser beam drilling a hole to the core of the pellet. It has been demonstrated that the fusion neutron yield can be enhanced by a factor of 1000 with a heating pulse with a power in the petawatt range [132].

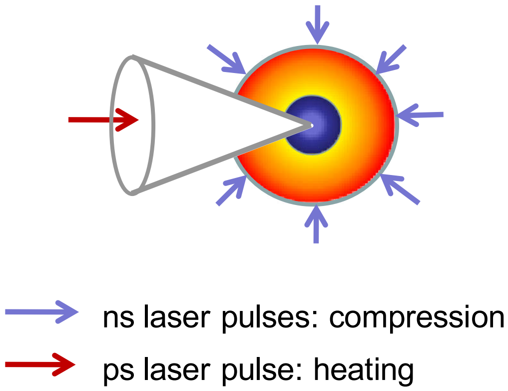

Fig. 2.5: *Cone-guided fast ignition. A pellet is compressed by ns laser pulses to a density of about 300 g/cm*^{3}*. A re-entrant cone is attached to the pellet. A strong beam of MeV electrons is generated by focusing a ps laser pulse into the cone. The electrons are emitted from the tip of the cone and are then absorbed in the center of the compressed pellet by collisions.*

The progress in ICF research is closely related to our understanding of the physics of dense plasmas. The compression of the fusion pellet is basically determined by radiative hydrodynamics. Therefore, the knowledge of the equation of state and the opacity of the dense plasma in the pellet is crucial for a prediction of the performance. The transport of the huge current proposed in the fast ignitor scheme is widely unexplored. A large number of studies have investigated the complex processes involved. Many of these studies do not require a complete inertial confinement infrastructure. In particular, experiments on electron transport, EOS and radiative properties of dense plasmas can be carried out at smaller facilities, and the collaboration between large scale laboratories with smaller facilities has been essential for the progress in ICF research.

2.4 Ultrafast x-ray science

Dense plasmas with temperatures in the range of 100 – 1000 eV are produced when ultra-short, intense laser pulses are incident onto solids. The interaction is accompanied by the generation of populations of supra-thermal electrons with MeV temperatures. Under these conditions, bremsstrahlung is generated over a wide spectral range. In addition, ionic resonance lines in the x-ray and XUV range and characteristic x-rays from inner shell transitions are emitted. The duration of the x-ray pulses can be extremely short, close to the laser pulse duration. This short pulse duration makes x-ray diffraction experiments with an unprecedented temporal resolution possible. Pump probe experiments using laser generated x-rays have investigated ultrafast processes such as the lattice dynamics of crystalline samples, nonthermal melting or phase transitions [190]. An example for a pump probe experiment investigating coherent lattice vibrations in a bismuth crystal is shown in Fig. 2.6 [213]. Lattice vibrations are excited with a femtosecond laser pulse incident onto the surface of the bismuth sample. A short pulse of x-rays is produced from a thin titanium wire irradiated with an intense, ultrashort laser pulse with a defined delay. Fig. 2.6 shows the intensity of the titanium K_α Bragg reflex from the (222) plane as a function of the delay. The oscillations of the reflectivity are related to the coherent lattice vibrations with a period of 467 fs.

In addition, the potential of laser produced x-rays for biomedical imaging has been demonstrated in a number of studies [128, 221]. In combination with time gated imaging techniques, the short duration of laser based x-ray sources allows for the reduction of radiation exposure in medical applications.

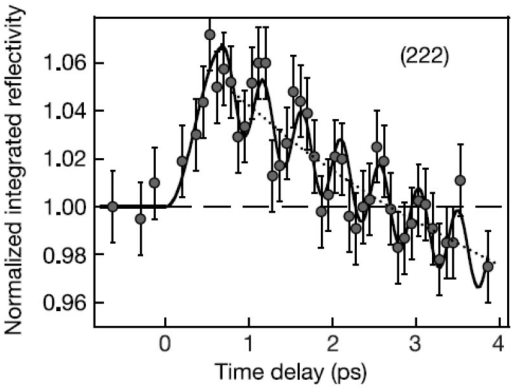

Fig. 2.6: *Pump-probe experiment investigating coherent lattice vibrations in a bismuth crystal [213]. The vibrations are excited by irradiation with a femtosecond laser pulse. The x-ray probe is generated by focusing an intense laser pulse onto a titanium wire. The plot shows the intensity of the x-ray probe reflected at the (222) plane as a function of the delay between pump and probe. Plot from Reference [213].*

3 Generation of ultrashort, intense laser pulses

Many of the experiments on dense plasmas carried out in the recent years have become possible through the development of high power laser systems generating ultraintense pulses with sub-picosecond durations. In the 1960s, Q-switching and mode locking were important milestones for increasing the peak intensities of short laser pulses. In the period from the beginning of the 1970s to the mid 1980s, only little progress was made. The reasons for this stagnation were difficulties in the amplification of the laser pulses caused by nonlinear processes in the optical components. The breakthrough towards higher intensities came in 1985 when the technique of chirped pulse amplification was invented [219]. The principle of chirped pulse amplification is shown in Fig. 3.1. The low energy pulses from an oscillator are stretched in time by a factor of 10^3-10^5. Due to the longer pulse duration, the intensity becomes smaller and non-linear effects in the amplifier media can be reduced to an acceptable level. Amplifier media with high saturation fluences such as titanium:sapphire or neodymium:glass increase the pulse energy by several orders of magnitude. Instead of conventional amplifier media, CPA has also been implemented using optical parametric amplifiers (OPCPAs). After the amplification, the pulses are re-compressed, ideally to their original duration.

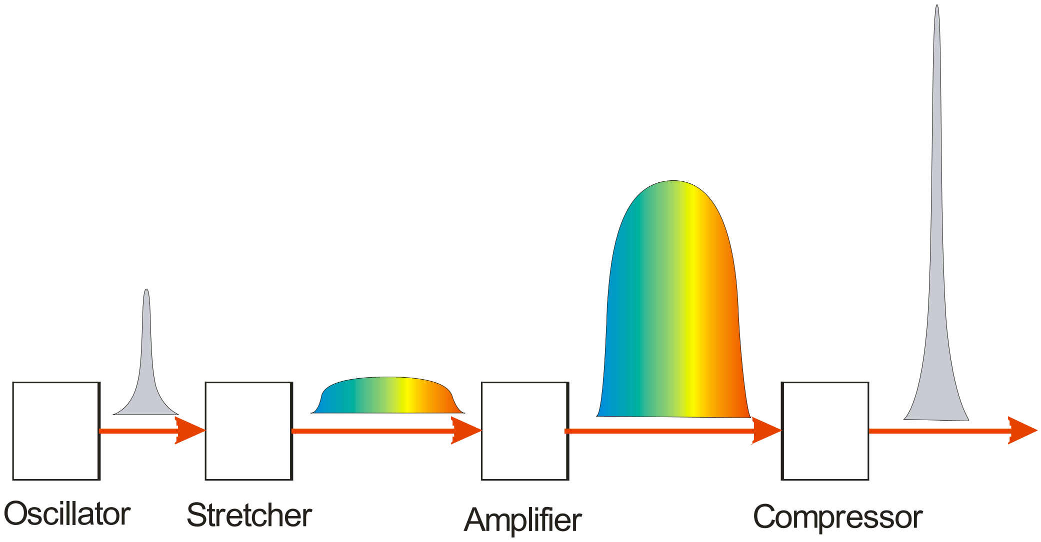

Fig. 3.1: *Principle of chirped pulse amplification.*

These days, table-top laser systems generating peak intensities in excess of 100 terawatt are routinely available in many laboratories. A number of petawatt lasers are operational, and new petawatt lasers are currently constructed in several laboratories. Future laser systems aiming at intensities in the Exawatt level are being planned. The ultrahigh energy densities and electromagnetic fields in combination with pulse durations on a femtosecond scale have made laboratory experiments in a completely new regime possible and have opened new opportunities for fundamental physics and technical applications. The development of the maximum laser intensities over the past decades with an extrapolation to the near future is shown in Fig. **3.2** [224].

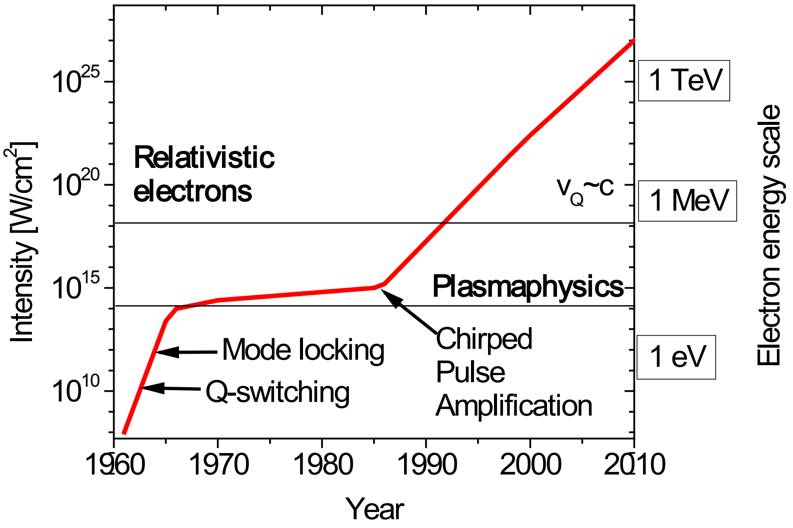

Fig. 3.2: *Development of maximum laser intensities over the past decades with an extrapolation to the future after [224]. On the right axis, typical energy scales of electrons in the laser field are shown.*

The maximum energy which can be extracted from an amplifier medium is roughly given by the saturation fluence [209]

$$F_S = h\nu / \sigma \quad , \tag{3.1}$$

where h is the Planck constant, ν is the frequency of the lasing transition and σ is the induced emission cross section. The minimum pulse duration which can be achieved is limited by the amplifier's gain bandwidth. For a laser pulse with a Gaussian shape in time, the relationship between pulse duration $\Delta\tau$ and bandwidth $\Delta\lambda$ is [209]

$$\Delta\tau \cdot \Delta\lambda \geq \frac{2\ln 2}{\pi}\frac{\lambda^2}{c} \quad . \tag{3.2}$$

In praxis, the bandwidth of the output pulses is smaller than the gain bandwidth of the amplifier medium due to the effect of gain narrowing. Gain narrowing can, at least partially, be compensated by shaping the spectrum of the seed pulses. In modern titanium:sapphire amplifiers, a bandwidth of more than 40 nm corresponding to a pulse duration of about 25 fs can be achieved. Taking advantage of the high gain bandwidth of non-collinear optical parametric amplifiers (NOPAs), intense few-cycle pulses with durations of less than 10 fs can be produced [176, 230].

In experiments, laser pulses are focussed by parabolic mirrors to achieve high intensities. For laser pulses with a Gaussian profile, the diffraction limited focus diameter defined by the 1/e^2 radius in intensity is [209]

$$w_0 = \frac{4\lambda}{\pi} \times \frac{f}{d} \quad . \tag{3.3}$$

Here, λ is the laser wavelength, f is the parabolic mirror focal length and d the initial beam diameter. This spot size corresponds to an average intensity of

$$I_0 = \left(1 - e^2\right) \times \frac{P}{w_0^2 \pi} \tag{3.4}$$

in the focal region. In praxis, the focal spot size is often larger because the profile of the laser beam deviates from Gaussian, and phase front distortions make the pulses less focusable. Using high aperture focussing optics in combination with adaptive optics, it has been demonstrated that focal spot sizes with an area in the order of λ^2 are possible [165].

Assuming a bandwidth limited pulse with duration $\tau = 1/\Delta\nu$ focussed down to a spot with an area of λ^2, this corresponds to an intensity of

$$I_{th} = \frac{h\nu^3 \Delta\nu}{c^2 \sigma} \tag{3.5}$$

per unit area of the amplifying medium. The intensities in Fig. 3.2 were estimated using Equation (3.5) assuming reasonable values for the size of the amplifier media.

3.1 Pulse contrast and preplasma formation

In laser amplifiers, the energy is stored in the amplifier crystals for durations in the order of microseconds before it is released to the seed pulse. Some leakage of the stored energy through the amplifier chains cannot be avoided, leading to the emission of electromagnetic radiation before the main pulse. Several processes can potentially contribute to the leakage. Amplified spontaneous emission (ASE) leads to a pedestal with a duration typically on a time scale in the order of nanoseconds before the main pulse. The leakage of oscillator pulses through optical shutters (pockels cells) in the amplifier chain and reflections in optical components lead to prepulses. Finally, nonlinear optical effects (e.g. self-phase modulation) in the optical components affect the spectral phase of the chirped laser pulse. Due to the associated higher order dispersion, the pulses cannot be perfectly recompressed and wings close to the laser peak are produced.

In most high power laser systems, the intensity of the light leaking through the amplifier chain is sufficient to generate a preplasma before the main pulse interacts with the target. Experiments have shown that the preplasma scale length significantly affects the interaction. Therefore, the knowledge of the prepulse intensity expressed in terms of the pulse contrast is an important parameter. Denoting the intensity of the radiation leaking through the laser system in a certain period before the main pulse by I_{Leak} and the main pulse peak intensity by I_0, the contrast is defined as I_0 / I_{Leak}.

3.2 Classes of laser systems

Laser technology has been rapidly developing in the recent years. Depending on the application, laser systems are being optimized in terms of repetition frequency, pulse duration, peak intensity, pulse energy and contrast. In this work, experiments were carried out with different laser systems. On the one hand, this allows for the investigation of the interaction over a wide range of experimental parameters. On the other hand, optimized laser conditions can be achieved for a specific application. Here, a brief description of some of the laser systems used in this work is presented.

3.2.1 Sub-10-fs laser systems

For the production of dense plasmas and for studies of optical field ionization at high intensities, laser systems with extremely short pulse durations less than 10 fs and an optimized contrast are required. For this kind of experiments, a laser system similar to that described in [103] was set up at our laboratory at the Institute for Laser and Plasmaphysics in Düsseldorf. A schematic of the laser system is shown in Fig. 3.3. The pulses from a titanium:sapphire oscillator are stretched in a SF57 glass block. A precise control of the pulse duration and the higher order dispersion was achieved using an acousto-optical dispersive programmable filter (Dazzler). After 9 passes through a titanium:sapphire crystal pumped with a frequency doubled Nd:YLF laser at a repetition rate of 1 kHz, the pulses are amplified to an energy of 1 mJ with a pulse duration of 25 fs.

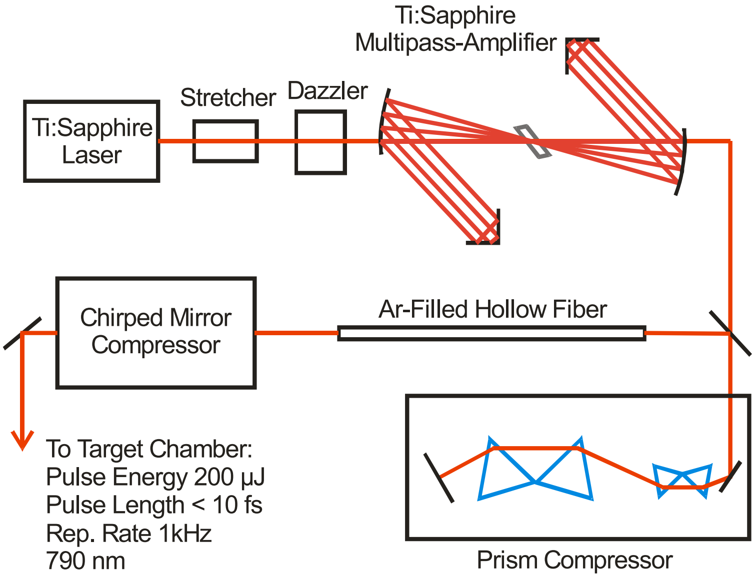

Fig. 3.3: *Drawing of the sub-10-fs laser system used for the generation of dense plasmas.*

The pulse duration is further reduced by a second compressor consisting of a noble-gas filled hollow-fiber and a set of eight chirped mirrors [43]. Due to self-phase modulation in the fiber, the spectral width of the laser pulses is increased by a factor of 3. The spectra measured before and after the fiber are shown in Fig. 3.4 (a). The pulses are then compressed to a length of less than 10 fs by the chirped mirror compressor. The temporal shape calculated from the spectrum assuming a bandwidth limited pulse duration is shown in Fig. 3.4 (b). The corresponding pulse duration is 7 fs (FWHM).

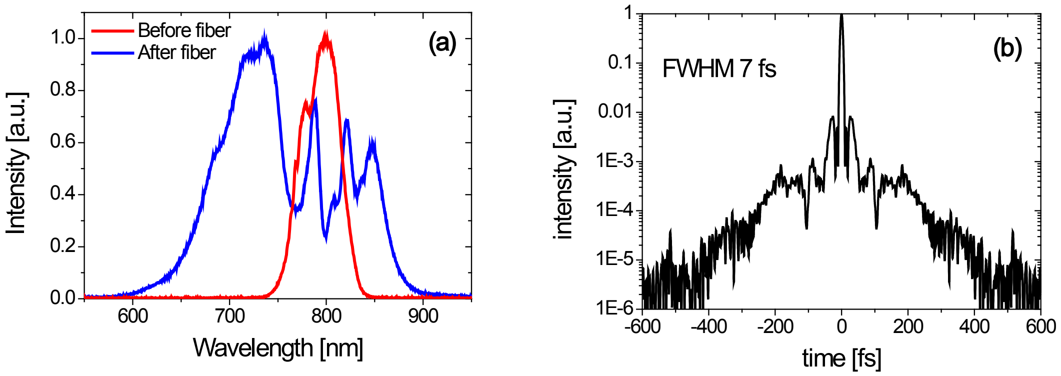

Fig. 3.4: *Spectrum of the laser pulse before and after the noble gas filled hollow fiber (a). Self-phase modulation increases the bandwidth by a factor of 3, resulting in a bandwidth limited pulse duration of less than 10 fs after the chirped mirror compressor (b).*

This value is close to the value of 8 fs which was measured with a second order autocorrelator. The contrast was measured before the hollow fiber with a third order autocorrelator. The result is shown in Fig. 3.5. The contrast was better than 10^5 for the period 1.3 ps before the laser pulse and the ASE contrast is in the order of 10^8.

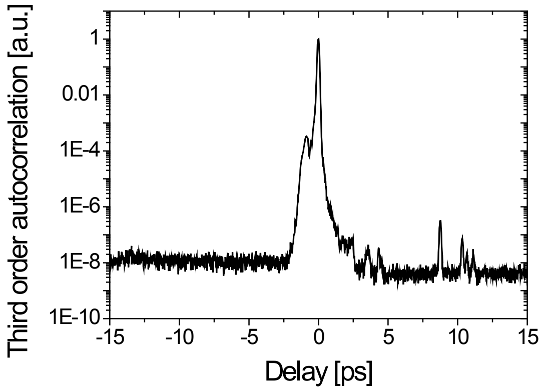

Fig. 3.5: *Third order autocorrelation of the titanium:sapphire laser system measured before the fiber.*

Due to their low intensity, the prepulses will not be spectrally broadened in the hollow fiber and consequently they are not further compressed. Therefore it is expected that the prepulse contrast is further improved by a factor of approximately 3 after the second compressor. Due to the transmission losses in the compressors and in the optics in the beam line, the energy on the target reduces to 200 µJ.

The peak intensity which can be achieved with this technique is limited by the energy that can be transported through the fiber. Here, peak intensities of the order of 10^{16} W/cm^2 were achieved. Few-cycle-pulses with higher intensities exceeding 10^{18} W/cm^2 were recently demonstrated using OPCPA amplifiers [176, 230]. These systems will allow for experiments in a new regime of laser plasma interactions in the near future.

3.2.2 Table top, terawatt laser systems

The generation of strong currents in solid targets requires laser pulses at relativistic intensities exceeding 10^{18} W/cm^2. Laser pulses with powers of more than 100 TW at a repetition frequency of 10 Hz can be generated with table-top titanium:sapphire multipass amplifier systems. The compact size of this type laser system, the high repetition frequency and the short pulse duration make this kind of laser system interesting for many research institutions.

Some of the experiments investigating the transport of strong currents in dense plasmas have been carried out at the THOR laser facility at the Texas Center for High Intensity Laser Science at the Universtity of Texas at Austin. THOR is a CPA titanium:sapphire laser system generating pulses with an energy of up to 700 mJ on target and a FWHM duration of 40 fs. Fig. 3.6 shows the setup of the laser. The pulses of a titanium:sapphire oscillator are stretched to a duration of 600 ps. The pulses are amplified in a regenerative amplifier and two multipass amplifiers to an energy of 1.2 J. After compression in a vacuum compressor, laser pulses with a duration of 40 fs and an energy of 700 mJ on target are available.

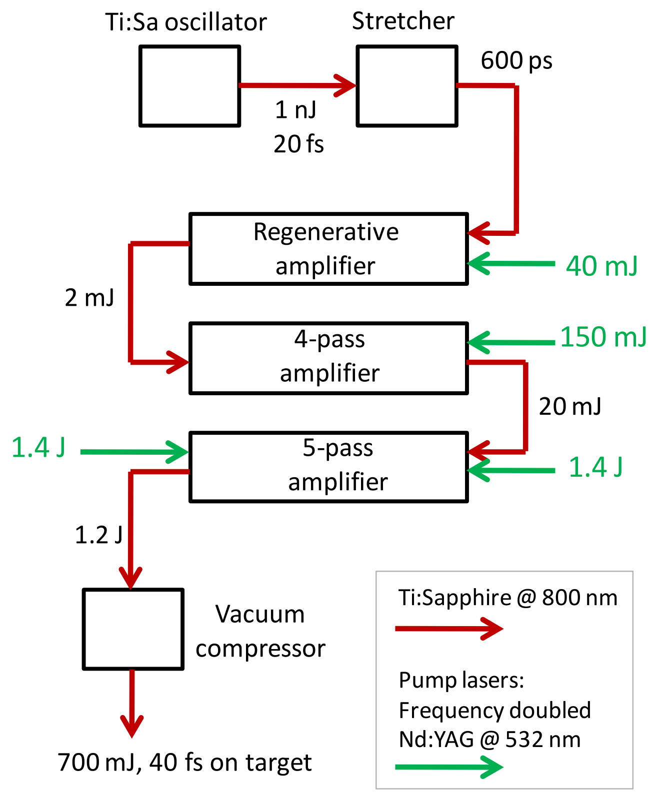

Fig. 3.6: *Schematic drawing of THOR laser.*

Because the preplasma scale length is an important parameter for the electron acceleration, the pulse contrast of THOR was characterized using a third order autocorrelator. The result is displayed in Fig. 3.7, showing a number of pre- and postpulses.

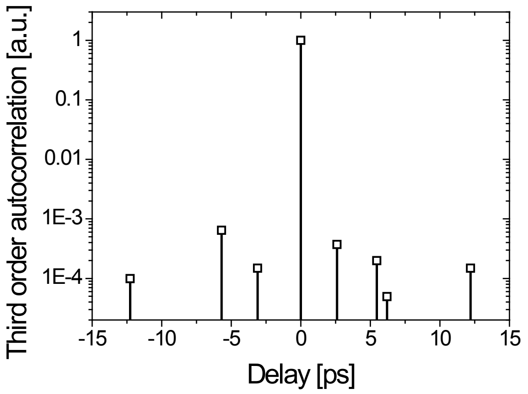

Fig. 3.7: *Third order autocorrelation obtained from THOR laser. The plot shows the main pulse at t=0 and a number of pre- and postpulses. The prepulses generate a preplasma with a scale length of 3.5 µm.*

A detailed study of the effect of the prepulses on the interaction of THOR with solids has been carried out in [220]. The conversion efficiency from laser energy in hard x-rays has been measured using planar silicon targets at different angles of incidence.

The maximum conversion efficiency was found for an angle of 10°. According to the theory of linear resonance absorption (see Chapter 4.4.3), this value corresponds to a preplasma scale length of 3.5 μm.

3.2.3 Petawatt laser systems

Some applications, such as ultrabright backlighters or the generation of strong currents needed in fusion research, require laser powers in the petawatt regime. The first petawatt laser was realized in 1996 by implementing CPA on one of the beamlines of NOVA laser at Lawrence Livermore National Laboratory [173]. Since then, petawatt lasers with improved designs were planned and set up in a number of laboratories [54, 58, 175, 204, 236].

In this work, experiments investigating the electron transport in dense plasmas relevant to fusion research were carried out using the VULCAN petawatt laser at Rutherford Appleton Laboratory. The pre-amplifier is based on OPCPA and generates broadband pulses with an energy of 10 mJ. In the main amplifier chain, a combination of Nd:silicate and Nd:phosphate amplifyer media are used. Laser pulses with energies of 500 J and durations of 500 fs are delivered on target [54]. The maximum repetition rate is limited by the heat load of the glass amplifiers to about one shot in 20 minutes.

4 Interaction of intense laser pulses with matter

A great variety of processes is involved in the interaction of intense laser pulses with matter. The plasma formation is induced by optical field ionization and impact ionization. A large number of collisional and collisionless heating processes contribute to the energy transfer from the laser to the plasma. Relativistic effects and strong quasistatic electric and magnetic fields generated during the interaction significantly affect the plasma dynamics. Populations of hot electrons and collisional radiative processes have an important impact on the energy transport in the plasma. In this chapter, some of the processes relevant in this work and their consequences for laser plasma interaction are discussed in more detail.

4.1 Ionization of matter in intense laser fields

Optical field ionization plays an important role for the plasma formation when intense laser pulses interact with matter. To characterize the ionization processes, it is userful to introduce the Keldysh parameter γ [123, 172]

$$\gamma = \sqrt{\frac{I_P}{2U_P}} \quad . \tag{4.1}$$

Here, I_P is the ionization potential and U_P is the ponderomotive potential of the laser (see Equation (4.10)). For $\gamma > 1$, the electric field of the laser can be considered as a small perturbation of the Coulomb field seen by the bound electrons. In this regime, the atom is ionized either by absorption of a single photon with an energy close to the ionization potential or by multiphoton ionization, i.e. the simultaneous absorption of a number of n lower energetic photons. The n-photon cross section σ_n is defined through

$$\Gamma_n = \sigma_n I_L^n \quad , \tag{4.2}$$

where Γ_n is the n-photon ionization rate.

Experiments have shown that the atom can absorb a larger number of photons than necessary for ionization [1, 95]. The energy of the excess photons is converted into kinetic energy of the freed electron. This process is called above threshold ionization (ATI).

For small values of the Keldysh parameter, $\gamma \ll 1$, the field of the laser significantly affects the Coulomb potential of the atom and a perturbative treatment is not possible, anymore. Electrons can escape from the atom by tunnel ionization. The theory of tunnel ionization has been developed for hydrogen-like atoms and ions by Keldysh [123] and has been extended to more complex atoms by Ammosov, Delone and Krainov (ADK) [4]. The ionization rates obtained from the ADK theory have been confirmed experimentally over a wide range of laser intensities [10].

At a certain threshold, the laser intensity is strong enough to suppress the Coulomb barrier below the ionization energy. In this regime, electrons are instantaneously released from the atom by barrier suppression ionization (BSI). The appearance intensity I_{app} at which BSI occurs is given by [90]

$$I_{app} = \frac{c\pi^2\varepsilon_0^3}{2e^6}\frac{I_p^4}{Z^2} \quad . \tag{4.3}$$

For a hydrogen atom with Z=1, the appearance intensity is $I_{app} = 1.37\times10^{14}$ W/cm^2

As soon as a population of free electrons is generated by optical field ionization, electron impact ionization becomes important. At high density, impact ionization results in an ionization avalanche and strongly affects the ionization dynamics. [25, 119]. An empirical formula for the impact ionization cross section is found for example in References [153, 154]. The cross sections strongly depend on the electron density and temperature.

4.2 Motion of electrons in intense laser fields

In an electromagnetic field, charged particles are accelerated by the Coulomb force and the Lorentz force. Due to their highest charge to mass ratio, electrons experience the strongest acceleration. The force on a single electron is given by

$$\frac{d\vec{p}}{dt} = -e\left(\vec{E} + \vec{\upsilon} \times \vec{B}\right) \quad . \tag{4.4}$$

Here, ***E*** and ***B*** are the electric and magnetic field, ***v*** is the velocity and ***p*** the momentum of the electron. In a monochromatic, plane wave, the electric and magnetic fields are periodic functions in time. At low intensity, the Lorentz force related to the magnetic field in Equation (4.4) is negligible. For a linearly polarized wave, the electron oscillates perpendicular to the wave vector and gains a peak momentum p_0 with

$$\frac{p_0}{mc^2} = a_0 \quad , \tag{4.5}$$

where a_0 is the normalized vector potential

$$a_0 = \frac{eA_0}{mc^2} = \frac{eE_0}{\omega mc} \quad , \tag{4.6}$$

A_0 and E_0 are the vector potential and electric field amplitudes, respectively. In the non-relativistic regime ($a_0 << 1$), this corresponds to the peak velocity

$$\frac{\upsilon_0}{c} \approx a_0 \quad . \tag{4.7}$$

At high intensity, when a_0 exceeds 1, the electrons quiver velocity approaches the speed of light and the Lorentz force cannot be neglected anymore. An electron which was initially at rest in the laboratory frame drifts in laser direction with a velocity

$$\frac{\upsilon_D}{c} = \frac{a_0^2}{4 + a_0^2} \quad . \tag{4.8}$$

In the co-moving reference frame, the motion of the electron has a figure 8 shape as shown in Fig. 4.1. For linear polarization, the Lorentz factor averaged over one oscillation period is

$$\bar{\gamma} = \sqrt{1 + a_0^2/2} \quad . \tag{4.9}$$

In a plane electromagnetic wave that is varying slowly in time, the electron interacts adiabatically with the electromagnetic field. Under these conditions, the electron does not gain energy from the electromagnetic wave. When the electron was initially at rest, it will be at rest again when the wave has passed by.

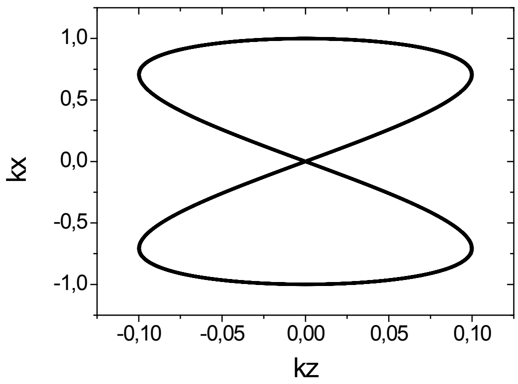

Fig. 4.1: *Figure 8 motion of an electron in a laser field with $a_0=1$ in the co-moving reference frame. The laser propagates in z-direction and is linearly polarized in x-direction. The wavenumber is k.*

The situation is different when the electron interacts with a tightly focussed laser beam. The strong gradients of the electromagnetic field in the focus result in complex electron trajectories [182]. The effects of the field gradients on the motion of the electron can be expressed in terms of the ponderomotive potential U_p. In the non-relativistic regime, the ponderomotive force has been investigated in great detail in [109]. A number of studies have shown that the formalism can be extended to the relativistic regime [17, 182], resulting in

$$U_p = \frac{mc^2}{4\bar{\gamma}} a_0^2 \quad . \tag{4.10}$$

The cycle averaged force on the electron is given by the negative gradient of the ponderomotive potential. In a laser focus, an electron will be pushed towards regions with low intensities and gains an energy $E = mc^2(\gamma - 1)$ which is of the order of the ponderomotive potential. The angle at which the electron is emitted from the laser focus is

$$\cos\theta = \sqrt{\frac{\gamma - 1}{\gamma + 1}} \quad . \tag{4.11}$$

Equation (4.11) has been confirmed in experiments measuring the energies and emission angles of electrons originating from different ionization stages of rare gases [159].

4.3 Propagation of laser pulses in underdense plasmas

Due to the electromagnetic interaction of the charged particles in plasmas, many phenomena are of collective nature. A prominent example is the collective oscillation of electrons at the plasmas frequency ω_p

$$\omega_p = \sqrt{\frac{e^2 n_e}{\varepsilon_0 \bar{\gamma} m_e}} \quad . \tag{4.12}$$

Here, e is the electron charge, n_e is the electron density, ε_0 is the dielectric constant, $\bar{\gamma}$ is the Lorentz factor of the electrons averaged over one oscillation period and m_e is the electron mass.

Laser pulses can only propagate in underdense plasmas, i.e. when the plasma frequency is smaller than the laser frequency ω_L. For a given laser frequency ω_L, the plasma is underdense when the electron density is smaller than the critical density n_c

$$n_c = \frac{\varepsilon_0 \bar{\gamma} m_e \omega_L^2}{e^2} = \frac{\omega_L^2}{\omega_p^2} n_e \quad . \tag{4.13}$$

At low intensity, the propagation of the laser pulse in a collisionless plasma can be described by a linear wave equation. The dispersion relation is

$$\omega^2 = \omega_p^2 + c^2 k^2 \quad , \tag{4.14}$$

corresponding to a refractive index n of

$$n = \sqrt{1 - \left(\omega_p / \omega_L\right)^2} = \sqrt{1 - n_e / n_c} \quad . \tag{4.15}$$

At high intensity, the interaction of the laser pulse with the plasma becomes non-linear. In this regime, a large number of phenomena such as stimulated Raman or Brillouin scattering, self-amplitude modulation, modulational and filamentation instabilities or self-focusing result from the interaction of the laser pulse with the plasma. Self-focusing, for example, is a consequence of the ponderomotive force and the relativistic motion of the electrons in the laser field. The ponderomotive force pushes electrons away from regions of high intensity, leading to the formation of a channel which can be fully depleted of electrons. The electron density n_e in the channel is given by [215]

$$n_e / n_0 = 1 + k_p^{-2} \nabla_\perp^2 \gamma \quad . \tag{4.16}$$

Here, n_0 is the ambient electron density, $k_p = \omega_p / c$ is the ambient plasma wave number and γ is the cycle averaged Lorentz factor of the electrons. In addition, according to Equation (4.12), the plasma frequency is smaller on the laser axis where the intensity is high. Both effects contribute to an increase of the refractive index on the laser axis, and the plasma acts on the laser beam like a converging lens. The detailed analysis shows that self-focusing dominates over diffraction when the laser power exceeds a threshold of

$$P_{SF} = 17\,\mathrm{GW} \times \frac{n_c}{n_e} \quad . \tag{4.17}$$

For laser powers above this threshold, the laser pulse collapses to a filament extending over distances significantly larger than the Rayleigh length [181]. Self-focusing and filamentation have been investigated in a number of experiments by imaging the self-emission from the channel, the transmitted light or by optical probing [30, 72, 74, 82]. Recently the strong electric fields associated with the channel have been directly observed by the proton projection imaging technique [120].

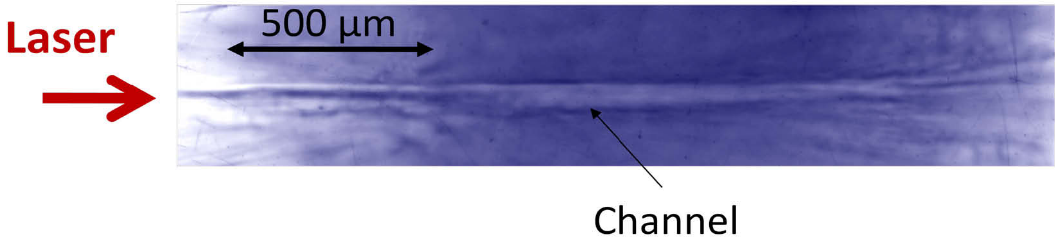

Fig. 4.2: *Observation of the quasistatic electric fields in an ion channel using proton radiography [120]. The channel was generated by the ponderomotive force of an intense laser pulse propagating through a gas target.*

4.4 Interaction of intense laser pulses with dense plasmas

Laser pulses cannot propagate in overdense plasmas. When a laser pulse is incident onto an overdense plasma, a fraction of the laser pulse will be reflected close to the critical surface. In addition, several processes of collective or collisional nature contribute to the absorption of laser energy. The interaction significantly depends on the experimental conditions, as for instance the laser intensity, pulse duration, polarization, plasma density and plasma scale length. A large number of experimental studies were carried out to investigate the effect of these parameters on the absorption of intense laser pulses in dense plasmas [33, 127, 179, 191, 201].

For laser pulses with low intensities up to the order of 10^{14} W/cm^2, collisional processes play an important role for the absorption. At high intensities, the electrons quiver velocity approaches the speed of light and collisional absorption becomes less important. The high values of the absorption in this regime are due to collisionless processes such as vacuum heating, $\boldsymbol{j} \times \boldsymbol{B}$ heating or resonance absorption. In the following chapters various absorption processes in dense plasmas are summarized.

4.4.1 Normal skin effect

At low intensities ($I \leq 10^{14}$ W/cm^2), when there is a sharp boundary between the vacuum and the overdense plasma, energy is absorbed due to collisions in a thin skin layer in the plasma. For a perfect step profile with the plasma-vacuum boundary at z=0

$$n_e = \begin{cases} 0, z<0 \\ n_0 > n_c, z \geq 0 \end{cases} , \tag{4.18}$$

the absorption can be calculated with the Fresnel formulae [35]. Due to preplasma formation and the expansion of the plasma during the interaction, the condition of a step profile is never strictly fulfilled for laser plasma interactions. Nonetheless, it is interesting to investigate the normal skin effect as a limiting case.

The absorption by the normal skin effect is determined by two parameters: the electron density n_e and their collision frequency ν. Because both parameters depend on the temperature, heating by the laser pulse and thermal conduction have to be taken into account. Different types of collisions are relevant in different stages of the interaction of ultrashort laser pulses with solids. In the initial state of the interaction, when the target is cold, there are contributions from electron-phonon collisions. At high temperatures, electron-ion collisions are relevant for the interaction. In addition, there are contributions of electron-electron collisions [191]. The electron-ion collision frequency ν_{ei} can be calculated with the Spitzer-Harm formula

$$\nu_{ei} = \frac{4}{3}\sqrt{2\pi}\,\frac{n_e Z e^4}{m^2 \upsilon_{te}^3}\ln\Lambda \quad . \tag{4.19}$$

Here, ln Λ is the Coulomb logarithm, Z is the ion charge, m is the electron mass and $\upsilon_{te} = \sqrt{kT/m}$ is the thermal velocity of the electrons. According to Equation (4.19), collisional absorption becomes weak when the thermal velocity of the electrons is high.

According to the Drude model, the relative permittivity ε for an electromagnetic wave with frequency ω is related to the collision frequency ν by [35]

$$\varepsilon = 1 - \frac{\omega_p^2}{\omega^2\left(1 + i\nu/\omega\right)} \quad . \tag{4.20}$$

The reflectivity R defined as the ratio of the reflected to the incident intensity depends on the polarization. The Fresnel formulae for p- and s-polarization are [35]

$$\begin{aligned} R_s &= \left|\frac{\sin(\theta - \theta_t)}{\sin(\theta + \theta_t)}\right|^2 \\ R_p &= \left|\frac{\tan(\theta - \theta_t)}{\tan(\theta + \theta_t)}\right|^2 \end{aligned} \quad . \tag{4.21}$$

Here, θ is the angle of incidence and θ_t is defined by Snellius' law

$$\theta_t = \sin^{-1}\left(\frac{\sin\theta}{n}\right) \quad . \tag{4.22}$$

The index of refraction n is related to the permittivity through

$$n = \sqrt{\varepsilon} \quad . \tag{4.23}$$

The fraction of energy absorbed by the normal skin effect f_{NSE} is

$$f_{NSE} = 1 - R \quad . \tag{4.24}$$

In the overdense region of the plasma, the electric field decays exponentially on a spatial scale given by the electron skin depth δ_s

$$\delta_s = \frac{c}{\omega_p} \left|1 + i\nu_{ei}/\omega\right|^{1/2} \quad . \tag{4.25}$$

The Fresnel formulae have been used to analyze the absorption of intense, ultrashort laser pulses measured in experiments. Typically, the finite plasma scale length in the experiments results in deviations from the Fresnel formulae [73, 191]. For a more precise calculation of collisional absorption, the expansion of the plasma during the interaction has to be taken into account. Hydrocodes have been successfully used to calculate the absorption of laser pulses in steep density gradient plasmas. Further details are discussed in Chapter 4.11.1.

The high values of the absorption observed in steep density gradients at intensities exceeding 10^{16} W/cm^2 cannot be explained by collisional processes, anymore. In this regime, collisionless processes described more in detail in Chapter 4.4.5 become important.

4.4.2 Inverse bremsstrahlung

In the case of long plasma scale lengths ($L>\lambda$), inverse bremsstrahlung in the underdense region of the plasma contributes to collisional absorption of the laser pulse. The propagation of an electromagnetic wave in the collisonal plasma can be described using the Helmholtz equations. Assuming a plasma density gradient in z-direction and an incident electromagnetic wave linearly polarized in x-direction (s-polarization) propagating in the y-z plane at an angle θ with respect to the z-axis as shown in Fig. 4.3 (a), the Helmholtz equation for the electric field is [35]

$$\frac{\partial^2 E_x}{\partial z^2} + \frac{\omega^2}{c^2}\left(\varepsilon - \sin^2\theta\right)E_x = 0 \quad . \tag{4.26}$$

For a linear density profile where the density ramps from 0 to n_c over a distance L, the x-component of the electric field has the shape of an Airy function as shown in Fig. 4.3 (b), whereas the y- and z-components are zero. At oblique incidence, the turning point of the electromagnetic wave is at a distance d before the critical density. Behind the turning point, the electric field is evanescent. For a collisionless plasma, the turning point is at ε=sin(θ).

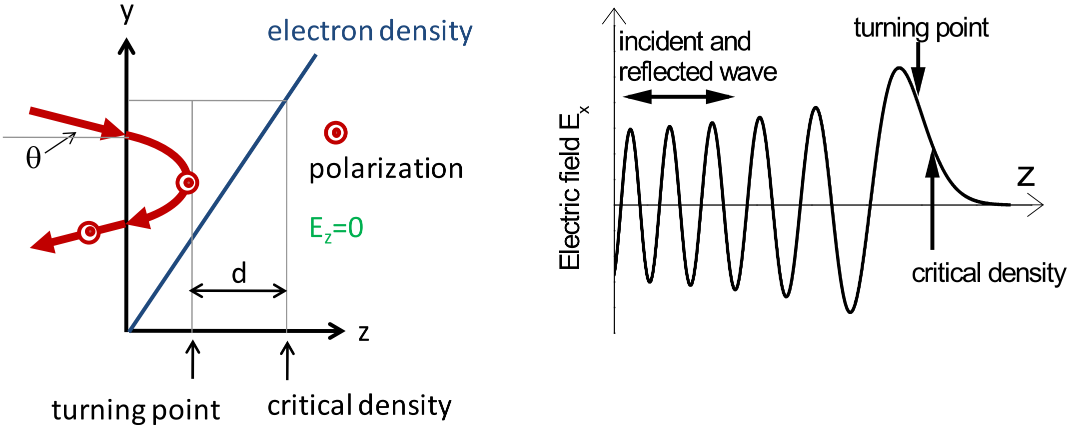

(a) (b)

Fig. 4.3: Reflection of an s-polarized electromagnetic wave by an overdense plasma with a linear density profile. At oblique incidence at an angle θ with respect to the z-axis, the turning point of the wave is at a distance d before the critical density (a). (b) shows the x-component of the electric field. Beyond the turning point, the field is evanescent.

The calculation yields a contribution of

$$f_{IB} = 1 - \exp\left(-\frac{32\nu_{ei}L}{15c}\cos^5\theta\right) \tag{4.27}$$

from inverse bremsstrahlung to the absorption [68, 140].

4.4.3 Resonance absorption

The situation for a p-polarized laser pulse at oblique incidence is shown in Fig. 4.4. At the turning point, the electric field has a component parallel to the density gradient. The electric field tunnels to the critical density layer where the laser frequency equals the plasma frequency. The z-component of the electric field is strongly enhanced, produces charge separations and resonantly drives plasma waves. This collisionless process is called resonance absorption.

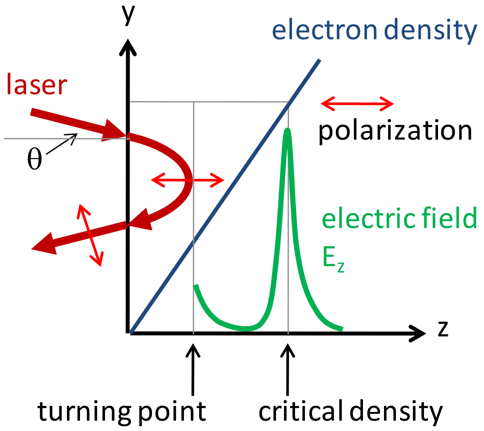

Fig. 4.4: *Resonance absorption occurs when a p-polarized laser pulse is obliquely incident onto a plasma density gradient. Unlike s-polarization, the z-component of the electric field does not vanish at the turning point. The green line represents the amplitude of the z-component of the electric field beyond the turning point. The field tunnels to the critical density layer, where plasma waves are resonantly driven.*

An analytic expression for the fraction of laser energy absorbed by resonance absorption is given in [92, 174]

$$f_{RA} \approx 36\tau^2 \frac{\mathrm{Ai}^3(\tau)}{|\mathrm{Ai}'(\tau)|} \quad . \tag{4.28}$$

Here, $\tau = (\omega L/c)^{1/3}\sin\theta$, Ai is the Airy function and Ai′ it's derivative. The absorption vanishes at τ=0 and approaches zero for $\tau\approx2$. The maximum absorption of $f_{RA}\approx0.5$ is at $\tau\approx0.8$. For a given scale length L, the angle of incidence for maximum absorption is $\theta_{max} \approx \arcsin\left[0.8 \times (c/\omega L)^{1/3}\right]$. As shown in Fig. 4.5, θ_{max} increases for small values of the scale length and approaches 90° at $L/\lambda \approx 0.081$. This result indicates that the theory of linear resonance absorption is not valid for very small values of the scale length. The reason for the breakdown of the linear resonance absorption at small scale lengths is discussed in the Chapter 4.4.5.

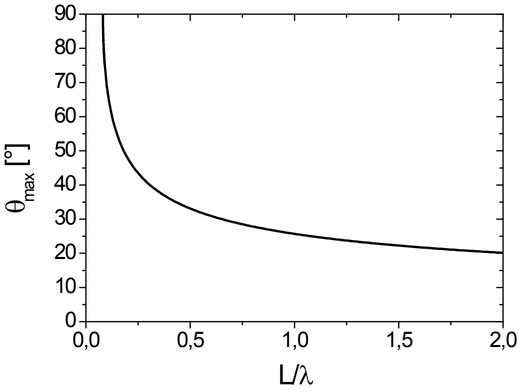

Fig. 4.5: *Angle of maximal resonance absorption versus density scale length. For small values of the scale length, the angle of maximum absorption shifts towards 90° (grazing incidence).*

4.4.4 *J* × *B* heating

As pointed out in [139], the high frequency component of the ponderomotive force of a laser pulse, which is proportional to ***j*** × ***B***, gives rise to another collisionless heating mechanism termed ***j*** × ***B*** heating. For a linearly polarized electromagnetic wave propagating in z-direction, the z-component of the ponderomotive force is

$$f_z = -\frac{m}{4}\frac{d}{dx}\upsilon_{osc}^2\left(1-\cos 2\omega t\right) \quad . \tag{4.29}$$

The first term on the right side of Equation (4.29) represents the DC component of the ponderomotive force. At high intensities, it plays an important role for the interaction as it is involved in density profile steepening and hole boring [90]. The second term is a high frequency component leading to heating of the electrons. Bunches of electrons are accelerated 2 times per laser cycle, predominantly in the direction of the laser. Ponderomotive heating works for any polarization except for circular. The contribution of ***j*** × ***B*** heating to the absorption and the scaling of the hot electron temperature with the laser intensity have been studied in detail in PIC simulations by Wilks [243].

4.4.5 Collisionless absorption processes in steep density profiles

For extremely small values of the plasma scale length, linear resonance absorption cannot contribute to the energy transfer from the laser to the plasma. The amplitude of the displacement of an electron close to the critical density is $z_0 = eE_d / m\omega^2$. Here, E_d is the driving electric field at the critical density layer. When the amplitude exceeds the plasma scale length, linear plasma waves cannot be driven, anymore. In steep density profiles other collisionless processes such as such as vacuum heating [43, 89], Brunel heating [38], anomalous skin layer absorption [246], sheath inverse bremsstrahlung [40] and anharmonic resonance absorption [161] become important. In the following paragraphs, two models relevant in this work are discussed.

4.4.6 Vacuum heating

When the electrons excursion length exceeds the plasma scale length, vacuum heating becomes important [89]. In steep density gradients, electrons in the underdense region of the plasma vacuum boundary are directly exposed to the laser field. An electron arriving at the boundary at a certain phase of the laser field will be accelerated away from the boundary and will then be reinjected into the overdense region of the plasma in the next half cycle of the laser. Because the laser field is strongly attenuated on a length given by the electron skin depth in the overdense plasma, the electron keeps on propagating into the target with the energy is has gained from the laser pulse. Brunel has investigated vacuum heating in a capacitor model neglecting magnetic fields and assuming a step profile [38]. The calculation yields a value of

$$f_{VH} = \frac{1}{\pi a_0} f \left[\left(1 + \alpha^2 a_0^2 \sin^2 \theta\right)^{1/2} - 1 \right] \frac{\sin\theta}{\cos\theta} \tag{4.30}$$

for the absorption f_{VH} by vacuum heating. The field amplification factor α is

$$\alpha = 1 + \left(1 - \eta_a\right)^{1/2} \tag{4.31}$$

and

$$\eta_a = \frac{4}{\pi} a_0 \frac{\sin^3 \theta}{\cos\theta} \quad . \tag{4.32}$$

Equation (4.30) predicts a strong absorption of up to 100% at grazing incidence.

The model of vacuum heating has been refined by computer simulations taking into account magnetic fields and more realistic density profiles [89]. The results are significantly different from the capacitor approximation and show a complex transition from vacuum heating to resonance absorption for increasing values of the density scale length. One reason for the deviation of the computer simulations from the capacitor approximation is the existence of surface currents generating magnetic fields which inhibit the reinjection of electrons into the target.[89]

4.4.7 Anharmonic resonance absorption

The concept of anharmonic resonance can be explained by a very fundamental physical image. For a harmonic oscillator, the cycle duration does not depend on the amplitude of the excursion, resulting in a constant eigenfrequency ω_0. A driving frequency close to ω_0 is required to drive the oscillator in resonance. The situation changes when the oscillation becomes anharmonic. The cycle duration and thus the eigenfrequency depend on the amplitude. Consequently, the oscillator can be driven to resonance with a driving frequency smaller than the initial eigenfrequency, provided that the driver strength is sufficient.

This model has recently been applied to investigate the absorption of intense laser pulses in steep density profiles [161]. For small amplitudes, the eigenfrequency of the electron fluid in the plasma is equal to the plasma frequency ω_{p0}. In the linear regime, plasma waves are resonantly driven only close to the critical density layer. The situation becomes different when the motion of the electron fluid becomes anharmonic at high laser intensities. For a single plasma layer with thickness d, the eigenfrequency ω_0 of the electron fluid decreases like [161]

$$\omega_0 = (\pi/4) \times \sqrt{\frac{\omega_{p0}^2 d}{\xi_0}} \quad . \tag{4.33}$$

Here, ξ_0 is the amplitude of the displacement of the electron fluid. Consequently, electrons can be driven to resonance with a driver frequency below the original plasma frequency.

An important prediction is the existence of a threshold for anharmonic resonance absorption. For a single plasma layer, the threshold for the electric field to drive the anharmonic resonance is [161]

$$E_{Th} = m_e \omega_p^2 d/(4e) \quad . \tag{4.34}$$

In computer simulations, it was confirmed that a large fraction of the electrons accelerated by intense laser pulses in steep density profiles exhibit a characteristic resonance behavior [161].

4.5 Generation of strong currents in dense plasmas

In Chapter 4.4, a number of processes contributing to the absorption of ultrashort, intense laser pulses in dense plasmas have been discussed. A fraction of the absorbed energy will be transferred to the electrons. The final kinetic energy of an individual electron depends on a number of stochastic factors such as the initial position of the electron and the laser intensity during the acceleration. Therefore, the energy distribution of an ensemble of N_0 heated electrons is typically broad and can often be described by a Boltzmann distribution with temperature T

$$\frac{dN}{dE} = \frac{N_0}{kT} \exp\left(-\frac{E}{kT}\right) \ . \tag{4.35}$$

Collisional processes generate a bulk population of thermal electrons with a temperature T_b. At high intenities, collisionless processes such as resonance absorption or $\boldsymbol{j} \times \boldsymbol{B}$ heating generate directed beams of electrons with a temperature T_h that is significantly larger than the bulk electron temperature. The existence of two electron populations with different temperatures T_b and T_h has been confirmed in experiments investigating the energy spectra of the electrons emitted from laser irradiated, solid targets [90, 200]. The generation of a beam of suprathermal electrons by collisionless processes is of immense importance for laser plasma interaction. Many phenomena such as target normal sheath acceleration (see Chapter 4.7) or the emission of high energetic x-rays are related to the strong currents associated with the hot electrons.

The characteristics of the hot electron population are closely related to the predominant acceleration process. In the case of resonance absorption, the laser drives plasma waves at the critical surface layer. Electrons are then heated in the strong fields of the plasma wave by Landau damping [68, 140] or by wave breaking [23, 24]. In this way, a beam of electrons bunched at the laser frequency is injected into the target at an angle close to the target normal. An empirical formula for the temperature of the hot electrons as a function of the laser intensity is given in Reference [18]:

$$T_{RA} = 0.1 \times (I_{17}\lambda_L^2)^{1/3}\text{MeV} \quad . \tag{4.36}$$

Here, I_{17} is the laser intensity in units of 10^{17} W/cm^2 and λ_L is the laser wavelength in microns.

For the case of $\boldsymbol{j} \times \boldsymbol{B}$ heating, the electrons are predominantly accelerated into the laser direction. Because the ponderomotive force has a component oscillating at twice the laser frequency ω_L (see Equation (4.29)), the electrons are bunched at $2\omega_L$. A scaling law for the hot electron temperature has been found by Wilks [243]:

$$T_{PM} = 0.511 \times \left[(1 + I_{18}\lambda_L^2/1.37)^{1/2} - 1\right]\text{MeV} \quad . \tag{4.37}$$

Here, I_{18} is the laser intensity in units of 10^{18} W/cm^2.

The laser driven electron beams transport strong currents into the target. To estimate these currents, a Boltzmann energy distribution with temperature T_h is assumed. The total number of electrons N_0 is related to the beam energy E_{Beam} by $N_0 = E_{Beam}/kT_h$. The beam energy can be calculated from the conversion efficiency η from the laser into hot electrons according to $E_{Beam} = E_{laser} \times \eta$. Typical values for the conversion efficiency are in the range of 15-40% [18, 227]. The current close to the interaction zone is approximately $I \approx eN_0/\tau$, where τ is the laser pulse duration. For a 30 fs laser pulse with an energy of 1 J, a conversion efficiency of η=20% and a hot electron temperature of T_h=1 MeV, the total number of electrons is about $N_0 \approx 10^{12}$, corresponding to a current of about 6 MA. It is noted that this value is significantly above the Alfvén limit introduced in Chapter 4.6.3. Due to velocity dispersion, the current will decrease as the electron beam propagates through the target. These aspects of electron beam transport are analyzed in detail in the following chapter.

4.6 Transport of strong currents in dense plasmas

For some applications such as the fast ignitor scheme in inertial confinement fusion or advanced x-ray sources, the transport of laser driven currents in the target is of fundamental importance. Bunching of electrons, return currents, self-generated magnetic fields and electromagnetic instabilities are important issues. In the following chapters, important aspects of the electron transport in dense plasmas relevant in this work are investigated.

4.6.1 Bunching of laser driven electron beams

As discussed in Chapter 4.5, some collective heating mechanisms as e.g. resonance absorption or $\boldsymbol{j} \times \boldsymbol{B}$ heating, produce bunched electron beams. The propagation of a laser driven, bunched electron beam in a metal foil is shown schematically in Fig. 4.6. In the interaction zone, electron bunches with a longitudinal dimension significantly smaller than the laser wavelength are generated. Due to velocity dispersion, the longitudinal dimension of the bunches increases as they propagate through the target. An important consequence of electron bunching is the emission of coherent transition radiation (CTR) from the rear surface as discussed in detail in Chapter 4.6.2.

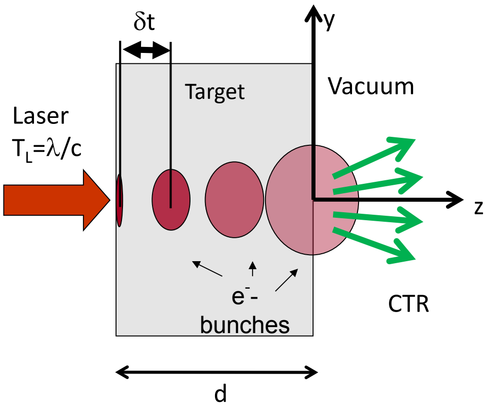

Fig. 4.6: *Schematic drawing of the transport of a laser driven, bunched electron beam in a solid target. The delay between two bunches is δt. Due to velocity dispersion, the duration of the electron bunches increases as they propagate through the target. The green arrows indicate the emission of coherent transition radiation (CTR) from the target rear surface (see chapter 4.6.2). The black arrows represent the coordinate system used in the transport model.*

In this chapter, the currents associated with the bunched electron beam are investigated. Therefore, we follow a transport model developed in [251, 252]. In this model, collisions of the fast electrons in the target are neglected and a ballistic transport is assumed. Under these conditions, the distribution function *f(t,**r**,**v**)* defined as the electron density in phase space satisfies the transport equation

$$\frac{\partial f}{\partial t}+\vec{v}\cdot\nabla f=0 \quad . \tag{4.38}$$

The components of the velocity and position vectors are $\vec{v}=(\vec{w},u)=(v_x,v_y,v_z)$ and $\vec{r}=(\vec{\rho},z)=(x,y,z)$, respectively. The target rear surface is in the x-y plane at *z*=0, the front surface is at *z*=-*d*, as indicated in Fig. 4.6. For a δ-like electron pulse with a transversal Gaussian profile with radius *a*, the initial distribution function is

$$f(0,\vec{r},\vec{v})=\frac{1}{2\pi a^2}\delta(z+d)\exp\left(-\frac{\rho^2}{2a^2}\right)f_v(\vec{v}) \quad , \tag{4.39}$$

where $f_v(\boldsymbol{v})$ denotes the velocity distribution and $\rho=\sqrt{x^2+y^2}$. In the following calculations, a relativistic 1-dimensional Maxwellian velocity distribution

$$f_v(\beta)=\frac{\beta mc^2}{kT(1-\beta^2)^{3/2}}\exp(-\varepsilon/kT) \tag{4.40}$$

is assumed, where $\varepsilon=mc^2\left[(1-\beta^2)^{-1/2}-1\right]$ is the electron's kinetic energy and *T* is the longitudinal beam temperature. Energy spectra for different values of the temperature *T* between 200 keV and 2 MeV are plotted in Fig. 4.7. At high temperature, a large number of the electrons propagate with a velocity close to the speed of light *c*. Consequently, there is a peak in the velocity distribution close to *c*.

The distribution function $f_\tau(\tau)$ describing the electrons phase space density after propagation of a distance *d* at time *τ* follows as

$$f_\tau(\tau,\vec{\rho},\vec{v})=\frac{1}{2\pi a^2}\delta(\tau-d/u)\exp\left(-\frac{(\vec{\rho}-\vec{w}\tau)^2}{2a^2}\right)f_v(\vec{v}) \quad . \tag{4.41}$$

The current associated with the electrons at *z*=*d* as a function of time is

$$j(\tau)=eN\int d\rho dv f_\tau(\tau,\vec{\rho},\vec{v}) \quad . \tag{4.42}$$

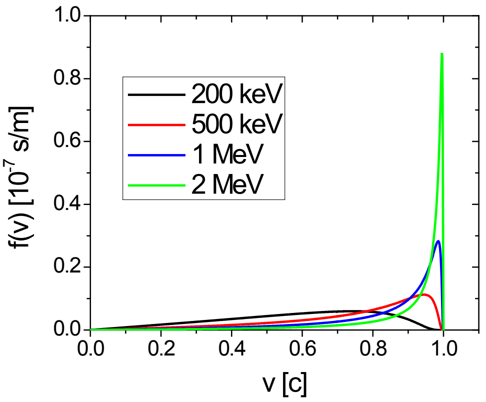

Fig. 4.7: *Relativistic Maxwellian velocity distributions for electrons with different temperatures between 200 keV and 2 MeV. For the higher temperatures, the velocity distribution is peaked at a velocity close to the speed of light.*

It is instructive of investigate the effect of velocity dispersion on the current using Equations (4.41) and (4.42). In Fig. 4.8, the current associated with a single bunch of electrons with a Maxwellian velocity distribution is shown for different propagation lengths between 10 and 100 µm. In the calculations, the electron bunch is initially δ-shaped and is injected into the target in the z-direction at *t*=0. The electron temperature is 1 MeV. Because the energy spectrum is broad, velocity dispersion results in a decrease of the peak current and broadening of the electron bunches as they propagate through the target.

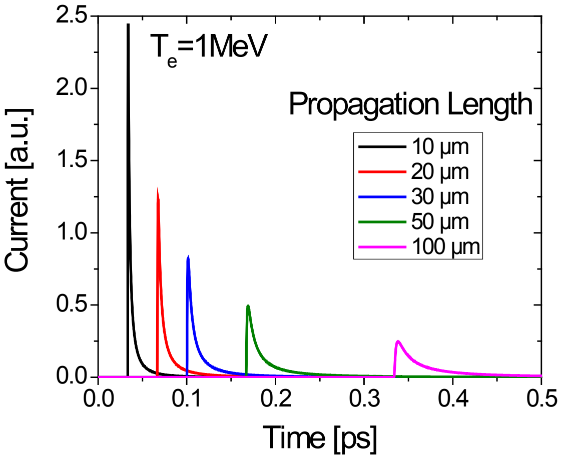

Fig. 4.8: *Current associated with an electron bunch with a Maxwellian velocity distribution for different propagation distances. Due to velocity dispersion, the width of the electron bunch increases, whereas the peak current decreases for long propagation distances.*

In high intensity laser interaction with dense plasmas, multiple electron bunches are accelerated at the front surface. This situation is illustrated in Fig. 4.9 showing the current produced by a total number of 100 identical electron bunches with a temperature of 1 MeV at the rear side of a foil with 10 µm thickness. In the calculation, the delay between adjacent electron bunches is 1.76 fs. This delay corresponds to the injection of two electron bunches per laser cycle (as expected for ***j*** × ***B*** heating) for a laser wavelength of 1053 nm. The time *t*=0 corresponds to the injection of the first electron bunch into the target.

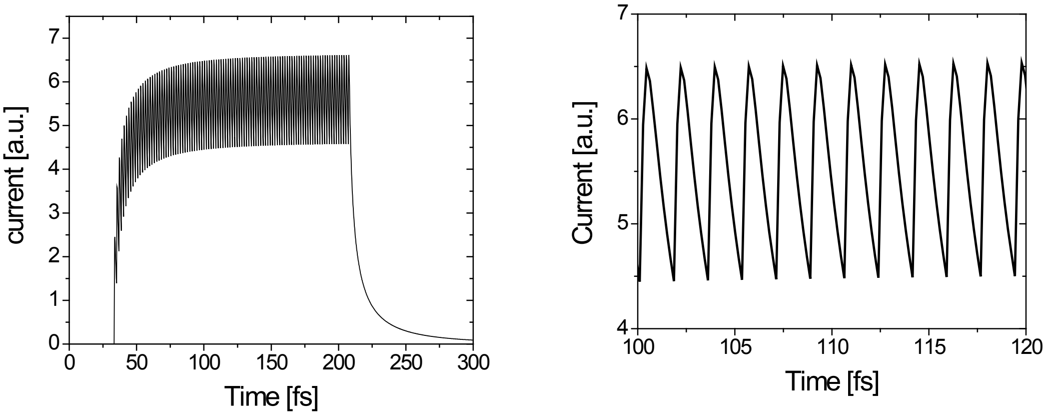

Fig. 4.9: *Current produced at the rear surface of a 10 µm thick foil by a total number of 100 electron bunches. The right hand side shows a detailed view for the time interval from 100 to 120 fs.*

4.6.2 Optical transition radiation

Optical transition radiation (OTR) is emitted when charged particles cross the boundary between two media with different optical properties [86, 91]. The emission of radiation is related to the temporal change of the polarization in the vicinity of the charged particles as they cross the boundary [117]. Transition radiation has been studied extensively in particle accelerators in the x-ray [45, 46, 248], optical [155, 168, 240] and far-infrared region [99, 208, 239]. More recently, transition radiation has been used to investigate transport of laser driven electron beams in planar foil targets [16, 48, 85, 118, 199, 253]. As shown in Fig. 4.6, transition radiation is generated when the electrons cross the boundary between the target rear surface and the vacuum.

In the case of a constant flux of particles, the contributions of the individual particles add up incoherently and the OTR fluence is proportional to the number N of particles. The situation is different when the particle beam is bunched as shown in Fig. 4.6. In this case, the contributions of the individual bunches add up coherently. The fluence of the coherent transition radiation (CTR) is proportional to N^2.

As discussed in Chapter 4.5, bunching is a typical signature of some heating mechanisms in laser irradiated solids. For resonance absorption, the electrons are bunched at the laser frequency, whereas they are bunched at twice the laser intensity for $\boldsymbol{j} \times \boldsymbol{B}$ heating. When the electrons are emitted from the target, they generate CTR with spectral characteristics which depend on the bunching frequency and thus on the predominant acceleration mechanism. This makes CTR an ideal tool to distinguish between different acceleration mechanisms in high intensity laser plasma interaction [177].

A model for the emission of transition radiation generated by laser driven electron beams in planar foil targets was developed in [251, 252]. The calculations are based on the ballistic transport model discussed in the previous chapter. Here, some important results which are used for data analysis in the experimental part of this work are summarized.

For the calculations, a cartesian coordinate system is chosen as indicated in Fig. 4.10. The rear surface of the planar foil is in the x-y plane at z=0 and the front surface is at z=-d. The center of the electron beam at the rear surface is at $\boldsymbol{r}$=(0,0,0). The directions of the electron velocity and the wave vector are given by the azimuthal and polar angles (Θ,Φ) and (θ,ϕ), respectively. The components of the wave vector are $\vec{k} = (\vec{q},\eta) = (k_x,k_y,k_z)$.

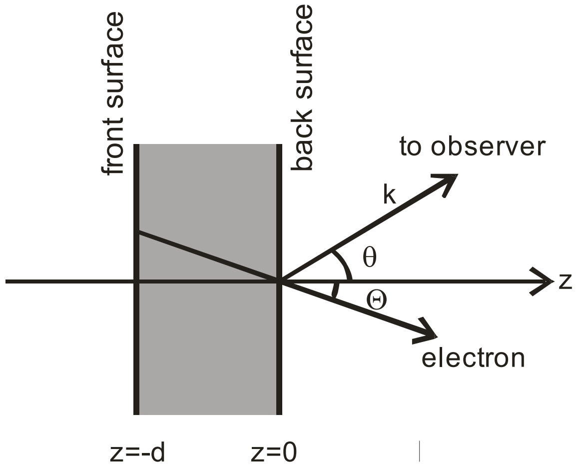

Fig. 4.10: Geometry for the calculation of the emission of coherent transition radiation from laser accelerated electron beams.

An important result in [252] for the CTR energy emitted per frequency and solid angle element by a total number of Λ identical electron bunches is

$$\begin{aligned}\frac{d^2E_{CTR}}{d\omega d\Omega} &= \frac{e^2N_b^2}{\pi^2 c}\exp\left(-q^2a^2\right)\\ &\times\left|\int d\tau dv \exp\left[i\left(\omega-\vec{q}\cdot\vec{w}\right)\tau\right]\sum_{\alpha=1}^{\Lambda}\delta\left(\tau-\tau_\alpha-d/u\right)f_v\left(\vec{v}\right)\exp\left(i\vec{q}\cdot\vec{w}\tau_\alpha\right)\right.\\ &\times\left.\frac{\beta\cos\Theta\left[\sin\theta-\beta\sin\Theta\cos\left(\phi-\Phi\right)\right]}{\left(1-\beta\sin\theta\sin\Theta\cos\left(\phi-\Phi\right)\right)^2-\beta^2\cos^2\theta\cos^2\Theta}\right|^2\end{aligned} \quad . \tag{4.43}$$

Here, the time for the emission of the α^{th} electron bunch is τ_α, $\beta=v/c$ is the velocity in units of the speed of light and N_b is the number of electrons in each bunch. According to Equation (4.43), the CTR energy depends on the emission angle Θ of the electron and the observation angle θ. In order to take into account this angular dependence, Equation (4.43) was used to analyze the experimental data in chapter 6.1.2 where two electron beams were emitted in different directions.

For the analysis of the experiments in the Chapters 6.1.1 and 6.2, the absolute value of the CTR fluence and the angular dependence are not crucial. In this case, the CTR emission can be calculated in 1D and Equation (4.43) can be written in the form [16]

$$I(\omega)=\eta(\omega)P^2\left|j(\omega)\right|^2\frac{\sin^2\left(M\omega\delta T/2\right)}{\sin^2\left(\omega\delta T/2\right)} \quad . \tag{4.44}$$

Here, M is the number of electron bunches, $\delta T=\tau_{\alpha+1}-\tau_\alpha$ is the delay between two adjacent electron bunches, $\eta(\omega)$ denotes the light intensity emitted by a single electron into the aperture of the detector optics and $j(\omega)$ is the Fourier transform of the current generated at the rear surface by a single electron bunch.

As an example, the CTR spectra calculated for the cases of resonance absorption and $\boldsymbol{j} \times \boldsymbol{B}$ heating are shown in Fig. 4.11. In the calculations, the laser wavelength is 1053 nm. The left hand side (a) shows the result for resonance absorption corresponding to δT=3.51 (one electron bunch per laser cycle). The CTR spectrum is peaked at multiples of the laser frequency ω_0. The right hand side (b) was calculated for $\boldsymbol{j} \times \boldsymbol{B}$ heating corresponding to δT=1.76 fs (two electron bunches per laser cycle). The CTR spectrum is peaked at multiples of the second harmonic of the laser. There is no peak at the fundamental. In both spectra the foil thickness is 10 μm, and a total of 100 identical electron bunches with a temperature of 1 MeV are emitted from the target.

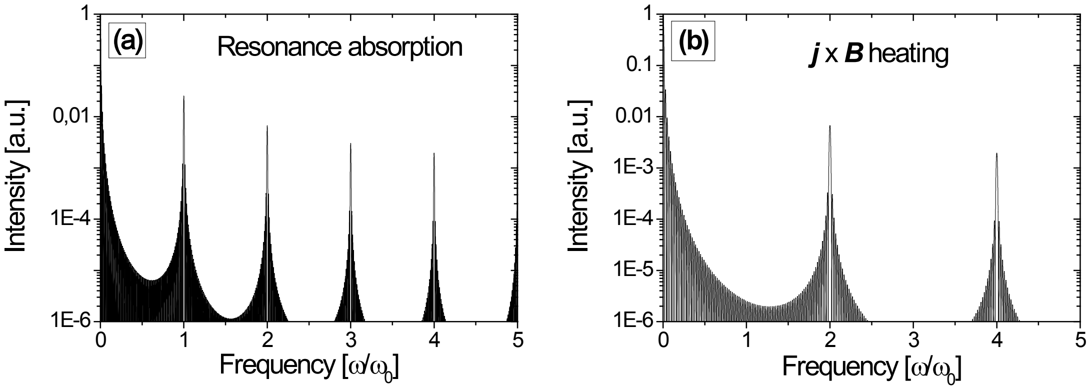

Fig. 4.11: *Spectra of CTR emission for the case of resonance absorption (a) and* $\boldsymbol{j} \times \boldsymbol{B}$ *heating (b) calculated with a 1D transport model. The frequency axis is in units of the laser frequency* ω_0*. For resonance absorption the CTR spectrum is peaked at multiples of the laser frequency, whereas it is peaked at multiples of* $2\omega_0$ *for* $\boldsymbol{j} \times \boldsymbol{B}$ *heating.*

A detailed view on the spectrum calculated for $\boldsymbol{j} \times \boldsymbol{B}$ heating around the second harmonic is shown in Fig. 4.12. The corresponding CTR fluences at 2ω are shown on the right hand side of Fig. 4.12 as a function of the target thickness for different temperatures. In the calculation, a dependence of the conversion efficiency into CTR from the electron energy is not taken into account. The decrease of the CTR fluence for long propagation lengths resulting from velocity dispersion can be seen clearly.

Moreover, the CTR fluence is stronger at high temperature. This observation can be explained regarding the relativistic velocity distributions shown in Fig. 4.7. At high temperature, a large fraction of the electrons propagate with a velocity close to the speed of light. Consequently, the width of the velocity distribution becomes smaller, and electron bunching is stronger at the target rear surface at high temperature.

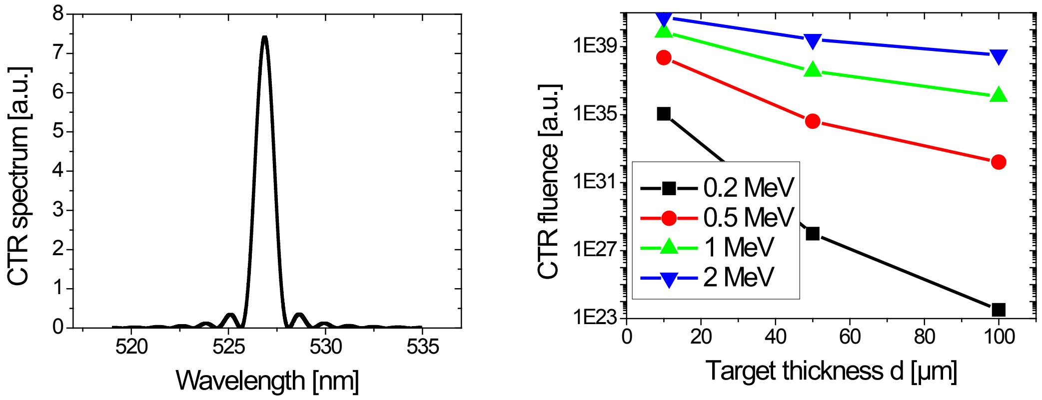

Fig. 4.12: *Calculation of the fluence of CTR generated by laser driven electron beams. Left hand side: CTR spectrum around the second harmonic of the laser. In the calculation, the electrons are accelerated by* $\mathbf{j}\times\mathbf{B}$ *heating (*δT*=1.76 fs at a laser wavelength of 1053 nm). Right hand side: corresponding of CTR fluences as a function of target thickness for different electron temperatures. Detailes are explained in the text.*

4.6.3 Effect of self-generated magnetic fields on the electron beam transport

Self-generated magnetic fields can dramatically affect the transport of electron beams in dense plasmas. A number of phenomena related to the self-generated magnetic fields, such as the Alfvén limit, collimation of the electron beam or filamentation due to instabilities are described in this chapter.

In Reference [3], Alfvén pointed out that the self-generated magnetic fields result in a maximum current which can be transported by charged particles. This result was obtained in a model where a uniform beam of identical charged particles with identical momenta is emitted from a circular area. The beam transports a current in a charge-neutralizing background plasma. When the current exceeds a certain threshold, the trajectories of the particles are strongly deflected and the beam cannot propagate, anymore. The following expression was obtained for the Alfvén limit:

$$I_A = \beta\gamma \frac{m_e c^3}{e} \approx 17.1 \beta\gamma \text{ kA} \quad . \tag{4.45}$$

More recently, the Alfvén limit was reinvestigated for laser driven, relativistic electron beams in dense plasmas. Here, the situation is more complex because factors such as the broad energy distribution and the interaction of the electron beam with the plasma become important [55]. Special attention has to be given to return currents transported by cold background electrons. Return currents can partially compensate the magnetic field generated by the high energetic electron beam. As a result, the hot electrons can transport currents exceeding the Alfvén limit. The maximum current depends on the plasma conditions and the electron beam characteristics [55].

The cold return currents j_{cold} are related to the plasma resistivity η by Ohm's law: $j_{cold} = E/\eta$. Assuming that the cold return currents compensate the current j_{fast} transported by the relativistic electron beam [19], the combination of Ohm's law with Faraday law yields the following expression for the growth of the magnetic field [20]

$$\frac{\partial \vec{B}}{\partial t} = \eta \nabla \times \vec{j}_f + \nabla(\eta) \times \vec{j}_f \quad . \tag{4.46}$$

As discussed in Reference [56], the first term on the right hand side of Equation (4.46) generates a magnetic field that pushes electrons towards regions of high current density, whereas the second term pushes electrons towards regions with high resistivity. Depending on the experimental conditions, the magnetic field can potentially increase or decrease the divergence of the relativistic electron beam propagating in the plasma.

The configuration of two counter propagating currents is susceptible to electromagnetic instabilities, such as the Weibel instability [241]. Instabilities can dramatically affect the transport and result in a filamentation of the electron beam. Neglecting collisions and the transversal beam temperature, the growth rate of the Weibel instability is [118]

$$\Gamma \approx \omega_b \frac{n_b}{n_e} \times \frac{\beta}{\gamma} \quad . \tag{4.47}$$

Here, ω_b is the electron beam plasma frequency, n_b and n_e are the electron densities of the beam and the surrounding plasma, respectively, β is the electron beam velocity in units of the speed of light and γ is the Lorentz factor of the beam. For conditions typically found for the interaction of intense laser pulses with dense plasmas, Equation (4.47) predicts a growth of the Weibel instability on a spatial scale of the order of 10-100 µm. This strong growth would significantly impair the transport of strong currents over long distances required for the FI scheme [107].

For a more detailed analysis of the effect of the Weibel instability on the transport of electron beams, a number of theoretical studies using PIC [39, 79, 107, 121] and hybrid [108] simulations were carried out. In was found that the dynamics of the Weibel instability strongly depends on the simulation parameters, as e.g. collision frequencies and the transversal beam temperature. From these data, there is still no unique picture, and further investigations are needed for a comprehensive understanding of the transport of strong currents in dense plasmas. The experimental observation of filamentation of an electron beam in a dense plasma due to the Weibel instability was reported in [118].

4.7 Target normal sheath acceleration

The interaction of intense laser pulses with solids leads to the formation of Debye sheaths at the target boundaries. In the associated electric fields, ions can be accelerated to high energies in the MeV range. Here, special attention is given to a process called target normal sheath acceleration (TNSA), where ions are accelerated from the rear side of thin foil targets [52, 100, 156, 211]. This process is schematically shown in Fig. 4.13.

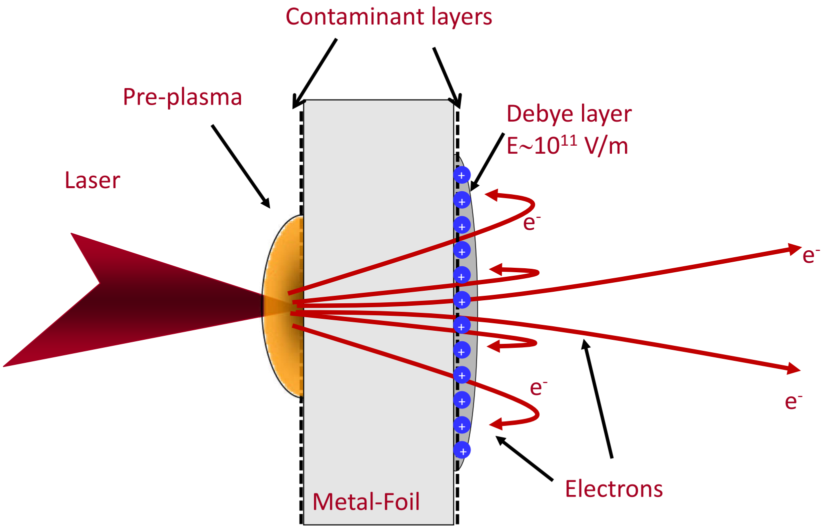

Fig. 4.13: *Target normal sheath acceleration. Protons and ions are accelerated in the strong electric field of the Debye sheath at the rear surface of a laser irradiated metal foil. The Debye sheath is generated by electrons which are accelerated at the front surface and propagate through the target.*

In the initial phase of the interaction, electrons are accelerated at the target front side and propagate through the target. At the rear side, they set up a dense electron plasma sheath with strong electric fields of the order of 10^{12} V/m [188]. Matter at the rear surface is ionized by field ionization, and the ions are rapidly accelerated normal to the target surface. The target surfaces contain layers of water vapour and hydrocarbon contaminants. Due to their high charge to mass ratio, the protons originating from these contaminants are accelerated most efficiently, and consequently mostly protons are observed unless the contaminants are removed from the target surface.

Many of the experimental observations can be quantitatively calculated by a fluid model where the emission of the ion beam is described as expansion of the plasma at the target rear side into vacuum [160]. The electron and ion densities at the rear side are schematically shown in Fig. 4.14 for two different times. At *t*=0, the ion density is given by a step function, whereas the electron density decays on a spatial scale given by the Debye length. At later times, an ion front is formed in the expanding plasma. The strong electric field in the Debye sheath at the front accelerates the ions until the electrons have lost their energy by cooling, and the ions keep on propagating with the velocity they have gained at that stage.

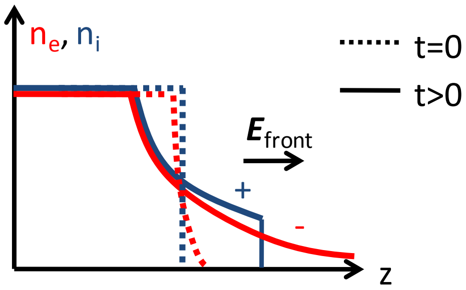

Fig. 4.14: *Expansion of the ion front according to the fluid model. The strong electric field in the Debye sheath at the ion front drives the ion acceleration, until the electrons have lost their energy by cooling.*

The initial electric field in the Debye sheath is

$$E_0 = \frac{n_{e0} k T_e}{\varepsilon_0} \quad , \tag{4.48}$$

where n_{e0} and T_e are the initial electron density and temperature, respectively. The electric field at the ion front at a later stage of the expansion is approximately given by

$$E_{front} \approx \frac{2E_0}{\sqrt{2\exp(1) + \omega_{pi}^2 t^2}} \quad . \tag{4.49}$$

Here,

$$\omega_{pi} = \sqrt{\frac{Z_i e^2 n_{e0}}{\varepsilon_0 m_i}} \tag{4.50}$$

is the initial ion plasma frequency, and Z_i and m_i are the ion charge and mass, respectively. The maximum energy E_{max} gained by the ions close to the ion front and is given by

$$E_{max} = 2T_e \left[\ln\left(t_p + \sqrt{t_p^2 + 1} \right) \right]^2 \quad , \tag{4.51}$$

where

$$t_p = \frac{\omega_{pi} t_{acc}}{\sqrt{2\exp(1)}} \tag{4.52}$$

is the normalized acceleration time. For the acceleration time t_{acc}, an empirical value of $t_{acc} \approx 1.3 \times \tau_{laser}$ is found in [81] where τ_{laser} is the laser pulse duration. According to the fluid model, the energy spectrum of the ions is

$$\frac{dN}{dE} = \frac{n_{e0} c_s t_{acc} A_D}{\sqrt{2ET_e}} \exp\left(-\sqrt{\frac{2E}{T_e}} \right) \quad . \tag{4.53}$$

Here, $c_s = \sqrt{Z_i T_e / m_i}$ is the ion sound speed and A_D is the area covered by the Debye sheath at the target rear surface. As an example, the energy spectrum calculated with Equation (4.53) for protons accelerated with 30 J, 1 ps laser pulses focused onto a 10 µm thick metal foil with a focal spot size of 10 µm is shown in Fig. 4.15. The spectrum is broadband with a maximum proton energy of about 45 MeV.

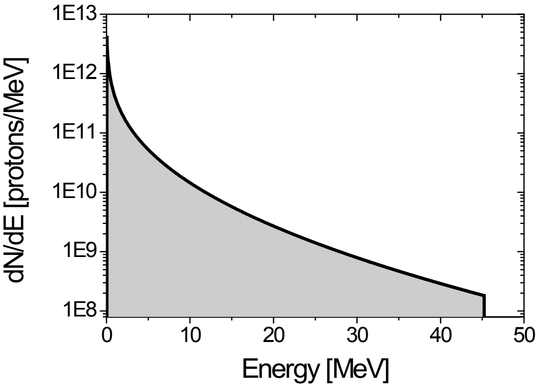

Fig. 4.15: *Energy spectrum of protons accelerated by TNSA calculated with the isothermal expansion model. The protons close to the ion front gain the maximum energy of 45 MeV. For details, see text.*

The penetration depth of MeV protons in dense matter vastly exceeds the penetration depth of visible and near infrared laser pulses. This is illustrated in Fig. 4.16 where the energy loss of protons with energies of up to 20 MeV in solid aluminium is plotted. The Bragg peak of the 20 MeV protons is close to 2 mm. The plots in Fig. 4.16 were calculated using the Monte Carlo code SRIM described in detail in [254]

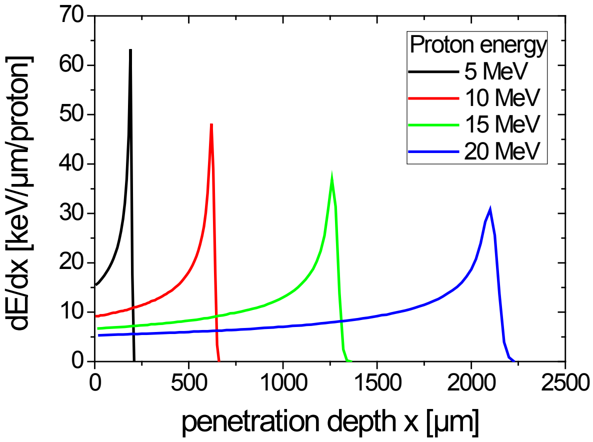

Fig. 4.16: *Energy loss of protons in solid aluminium. Due to their high penetration depth, MeV protons are ideal for radiaography in dense plasmas and isochoric heating of solids.*

Due to their small transversal emittance [32, 192], their short duration at the source and their high penetration depth in matter, laser produced proton beams are interesting for a number of applications. Laser driven proton beams have been used to generate dense plasmas by isochoric heating of solid density matter [5, 36, 61, 171]. Further details are discussed in Chapter 5.2. Radiography using laser driven proton beams turns out to be an ideal tool for probing electric fields in regions of dense plasmas not accessible for optical probing [29, 188]. Fig. 4.17 shows the formation of the ion front at the target rear side of a thin, laser irradiated foil observed with the proton projection imaging technique [187].

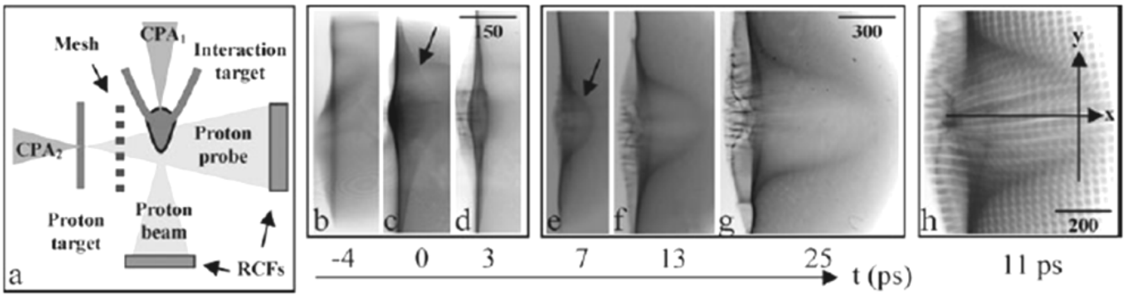

Fig. 4.17: *Formation of the ion front at the rear side of a thin, laser irradiated foil observed with the proton projection imaging technique. Images from Reference [187].*

4.8 Atomic kinetics in plasmas

The description of atomic kinetics in plasma is a complex task. The calculation of atomic population dynamics includes atomic structure calculations, scattering theory, plasma physics and statistical physics. Table 1 summarizes the relevant radiative and collisional processes which are important for the atomic kinetics in plasmas.

Process	Inverse Process
Photo excitation by absorption	Photo de-excitation by spontaneous or stimulated emission
Photo ionization	Photo recombination
Collisional excitation	Collisional de-excitation
Collisional ionization	Three body recombination
Auto ionization	Dielectric recombination

Table 1: *Collisional and radiative processes involved in the population dynamics of atoms and ions in a plasma.*

In principle, the atomic population dynamics can be derived by solving rate equations for each energy level and for each ion species present in the plasma. Due to the huge number of atomic energy levels involved, this would require an enormous computational effort. The complexity of the calculation is drastically reduced when the plasma in the state of thermodynamic equilibrium. In this case, the plasma can be fully characterized by a finite number of thermodynamic quantities. The principle of detailed balancing states that, in equilibrium, the rate for each process in Table 1 is equal to the rate of the corresponding inverse process.

At complete thermodynamic equilibrium, the velocity distribution is Maxwellian and the ionization-recombination dynamics is described by the Saha equation. The plasma emits blackbody radiation according to the Planck formula, and the population of the atomic energy levels is given by the Boltzmann distribution.

Although the investigation of systems in complete thermodynamic equilibrium is of immense importance in statistical physics, this condition is almost never fulfilled in laboratory plasmas. In praxis, the state of local thermodynamic equilibrium (LTE), where the equilibrium with the radiation field is not required, plays an important role.

4.9 Emission and absorption of radiation in plasmas

Radiative processes in dense plasmas have an important impact onto the atomic kinetics. On the other hand, measurements of the XUV and x-ray spectra provide a powerful tool to investigate atomic kinetics in dense plasmas. A detailed treatment of plasma spectroscopy is found in text books, e.g. in References [98, 151, 193, 197]. In the following section, some important results relevant for data analysis in the experimental part of this work are summarized.

The radiation emitted by a plasma is characterized by a set of radiometric quantities. The electromagnetic energy emitted from a plasma is related to the specific intensity or brightness I_ν defined by

$$dE = I_\nu dA dt d\Omega d\nu \quad . \tag{4.54}$$

Here, dE is the energy emitted by a surface element dA in the time interval dt into the solid angle $d\Omega$ within the frequency interval $d\nu$. The mean intensity is defined as the average of the specific intensity over the solid angle

$$J_\nu = \frac{1}{4\pi} \int_{4\pi} I_\nu d\Omega \quad . \tag{4.55}$$

The mean intensity is related to the spectral energy density u_ν by

$$J_\nu = \frac{c}{4\pi} u_\nu \quad . \tag{4.56}$$

In an isotropic radiation field one obtains

$$u_\nu = \frac{4\pi}{c} I_\nu \quad . \tag{4.57}$$

The interaction of the plasma with the radiation field is characterized by the emission and absorption coefficients. The spectral emission coefficient ε_ν is defined as the energy emitted by the plasma per volume, solid angle, frequency and time interval

$$\varepsilon_\nu = \frac{dE}{dV dt d\Omega d\nu} \quad . \tag{4.58}$$

The absorption coefficient κ is defined by the attenuation of a light beam crossing a plasma layer with thickness *ds* according to

$$\frac{dI_\nu}{ds} = -\kappa I_\nu \quad . \tag{4.59}$$

The transport of radiation in plasmas is determined by the radiative transport equation

$$\frac{dI_\nu}{d\tau} = -I_\nu + S_\nu \quad . \tag{4.60}$$

Here,

$$d\tau = \kappa ds \tag{4.61}$$

is the optical depth and

$$S_\nu = \frac{\varepsilon_\nu}{\kappa} \tag{4.62}$$

is the source function. Scattering of radiation is neglected in Equation (4.60). For an object in the state of complete thermodynamic equilibrium, the absorbed energy is equal to the emitted energy. Applying the principle of detailed balancing, it can be shown that the source function in equilibrium is given by the Planck formula

$$S_\nu = B_\nu \equiv \frac{2h\nu^3/c^2}{\exp(h\nu/kT) - 1} \quad . \tag{4.63}$$

The radiative transport equation plays an important role for the analysis of spectroscopic measurements. In general, the solution of the radiative transport equation for a given plasma geometry is complex. There are some cases when the radiative transport equation can be solved analytically. It turns out that the optical depth is an important parameter. Writing the radiometric quantities as a function of the optical depth τ instead of s, the formal solution is [193]

$$I_\nu(\tau) = I_\nu(0)\exp(-\tau) + \int_0^\tau \exp[-(\tau - \tau')] S_\nu(\tau') d\tau' \quad . \tag{4.64}$$

For a homogeneous plasma layer, i.e. when the source function S_ν is constant, the solution of Equation (4.64) is

$$I_\nu(\tau) = S_\nu + \left(I_\nu(0) - S_\nu\right)\exp(-\tau) \quad . \tag{4.65}$$

The emission and absorption of radiation in plasma is associated with radiative transitions of electrons. The initial and final states of the electron can be either bound-bound, bound-free or free-free.

Bound-bound transitions

The rate R_{ik} of photo excitation processes from a atomic level i to a higher energetic level k is related to the density n_i of particles in state i by [151]

$$R_{ik} = n_i u_\nu B_{ik} \quad . \tag{4.66}$$

Here, B_{ik} is the Einstein coefficient for absorption. The rate of photoemission due to spontaneous and stimulated emission is

$$R_{ki} = n_k A_{ki} + n_k u_\nu B_{ki} \quad , \tag{4.67}$$

where A_{ki} and B_{ki} are the Einstein coefficients for spontaneous and induced emission, respectively. Applying the principle of detailed balancing yields relations between the Einstein coefficients

$$A_{ki} = \frac{g_i}{g_k} B_{ik} \frac{8\pi h \nu_{ki}^3}{c^3} \tag{4.68}$$

and

$$g_k B_{ki} = g_i B_{ik} \quad . \tag{4.69}$$

Here, g_i and g_k are the statistical weights of the states i and k, and ν_{ki} is the frequency of the transition. Instead of the Einstein coefficients, the atomic transition rates are sometimes expressed in terms of the oscillator strength f_{ik}. The relation between the Einstein coefficient for spontaneous emission from state k to state i and the corresponding oscillator strength is

$$A_{ki} = \frac{8\pi^2 e^2 \nu_{ki}^2}{m_e c^3} \frac{g_i}{g_j} f_{ik} \quad , \tag{4.70}$$

where e is the electron charge, m_e is the electron mass and c is the speed of light. The contribution of a resonance line to the opacity is given by the Ladenburg relation

$$\int_{line} \kappa_L(\nu)d\nu = \frac{h\nu}{c} n_i B_{ik} \quad . \tag{4.71}$$

Using the normalized line profile $\phi(\nu)$, Equation (4.71) can be written in the form

$$\kappa_L(\nu) = \frac{h\nu}{c} n_i B_{ik} \phi(\nu) \quad . \tag{4.72}$$

The corresponding expression for the contribution of the resonance line to the emissivity is

$$\varepsilon_{\nu,L} = \frac{h\nu}{4\pi} A_{ki} n_k \phi(\nu) \quad . \tag{4.73}$$

At low density, the line profile $\phi(\nu)$ is determined by the lifetime of the transition and the Doppler effect. The limited lifetime of the states involved in the transition results in a Lorentz profile, whereas the Doppler shift yields a Gaussian profile. The convolution of the Lorentz and the Doppler profiles results in a Voigt profile. At high density, the line profiles are dominated by pressure broadening and Stark broadening (see Chapter 4.10).

Bound-free transitions

For the bound-free transitions, the opacity is related to the cross section for photo-ionization. The classical calculation for the photo-ionization cross section σ_n^{cl} of a hydrogenic ion with charge z-1 (z=1 for a neutral atom, z=2 for a singly charged ion, etc.) and principal quantum number n yields [151]

$$\sigma_n^{cl}(\nu) = \frac{64\pi^4 m_e e^{10}}{3\sqrt{3}ch^6} \times \frac{z^4}{\nu^3 n^5} \quad . \tag{4.74}$$

The quantum mechanical calculation results in a value $\sigma_{z\text{-}1,n}$ which is slightly different from Equation (4.74). The quantum mechanical corrections can be expressed in terms of the Gaunt factor G_n

$$\sigma_{z-1,n}(\nu) = \sigma_n^{cl}(\nu) G_n(\nu) \quad . \tag{4.75}$$

The cross section for photo-recombination with a hydrogenic ion in the ground state $\sigma_{z,1}$ can be calculated from the Milne relation

$$\sigma_{z,1}(\nu, \upsilon) = \frac{g_{z-1,i}}{g_{z,1}} \left(\frac{h\nu}{m_e c\upsilon}\right)^2 \sigma_{z-1,i}(\nu) \quad . \tag{4.76}$$

Here, υ is the free electron's velocity. The contribution from photo-ionization to the opacity is

$$\Delta\kappa(\nu) = n_{z-1,i}\sigma_{z-1,i}(\nu) \quad . \tag{4.77}$$

Here, $n_{z\text{-}1,i}$ is the density of ions with charge z-1 in quantum level i. The corresponding expression for the contribution to the emissivity is

$$\Delta\varepsilon_\nu = n_e n_{z,1} f(\upsilon) \frac{h^2\nu}{4\pi m_e} \sigma_{z,1}(\nu, \upsilon) \quad , \tag{4.78}$$

where $f(\upsilon)$ is the velocity distribution of the free electrons.

Free-free transitions

A semi-classical calculation of the free-free emissivities and opacities was carried out in Reference [135]. The results for a Maxwellian velocity distribution are [151]

$$\varepsilon_\nu^{ff} = C_4 z^2 \frac{n_e n_z}{\sqrt{T_e}} \exp\left(-\frac{h\nu}{kT_e}\right) \tag{4.79}$$

and

$$\kappa^{ff}(\nu) = C_6 n_e n_z \frac{z^2}{\nu^3 \sqrt{T_e}} \tag{4.80}$$

with

$$C_4 = \frac{16\pi e^6}{3c^3\sqrt{6\pi m_e^3 k}}$$

$$C_6 = \frac{8\pi e^6}{3m_e hc\sqrt{6\pi m_e k}} \quad .$$

Similar to the bound-free transitions, the quantum mechanical calculations yield deviations from the classic results which can be expressed in terms of Gaunt factors. Gaunt factors for the free-free transitions have been published in [122].

4.10 Collisional radiative effects at high density

At high density, the interaction of an ion with other particles in a plasma affects the energy levels of bound electrons. Numerous effects such as line broadening, line shift, satellite emission, pressure ionization, continuum lowering or the Inglis Teller effect result from the interaction. Many of these effects were identified in experiments investigating the XUV and x-ray emission from dense, laser produced plasmas [9, 14, 65, 87, 157, 162, 163, 183, 195, 214, 233, 244]. In this section some of the effects relevant in this work are discussed.

Line broadening and line shifts

At high density, the energy levels of radiating ions are disturbed by the electric field of surrounding electrons and ions. Elastic or inelastic collisions of electrons with the radiating ion result in pressure broadening of the resonance line. The duration of the collisions with electrons is typically much shorter than the lifetime of the radiating ion, and the effect of the electrons can be treated perturbatively. In contrast, the interaction with surrounding ions is on a timescale much longer than the lifetime of the excited state. The effect of the ions' microfield results in a shift of the frequency of the resonance line. The final line shape is obtained by averaging over all line shifts of an ensemble of ions. Line profiles in dense plasmas are often calculated using the standard quasistatic ion and impact electron approximations [143].

Besides line broadening, the microfield of the electrons and ions surrounding a radiating ion also results in a shift of resonance lines. This effect called plasma polarization shift has been observed for the first time in [21].

Satellites

At high density, dielectric recombination leads to a significant population of double excited states and to the emission of satellites at the low energy side of resonance lines [195, 157]. Satellites have been observed for the first time in [62] and were classified in [83]. An example of a configuration leading to the emission of a dielectric satellite is shown in Fig. 4.18. Fig. 4.18 (a) and (b) show the configuration for the emission of the Ly_α and He_α lines, respectively. In Fig. 4.18 (c) there are two electrons in an excited state, resulting in the emission of a helium-like satellite of the Ly_α line. The second electron is not involved in the transition and is therefore referred to as spectator electron. Because the spectator electron is in an excited state, its contribution to shielding of the Coulomb potential of the nucleus is smaller than in (b), and the satellite is at a wavelength between the Ly_α and the He_α. Due to the large number of electronic configurations, a large number of satellites exist. Besides dielectric recombination, double excited states are populated by three body recombination.

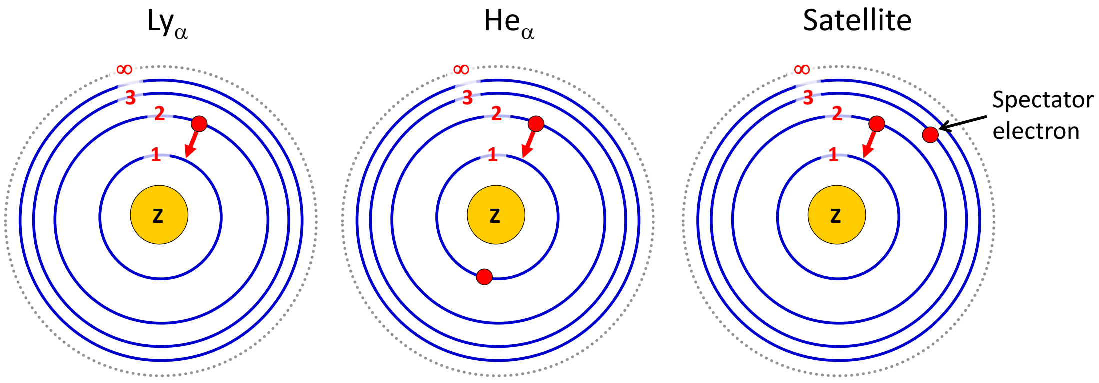

(a) (b) (c)

Fig. 4.18: *Emission of satellites from ions with more than one excited electron. The blue circles represent the atomic energy levels. The main quantum numbers 1-3 are shown. The series limit is indicated by the ∞ symbol. Fig. (a) and (b) show the configuration for the emission of the Ly_α and the He_α resonance lines, whereas (c) is the configuration for the emission of a He-like satellite of the Ly_α line. The spectator electron contributes to shielding of the Coulomb potential, and the energy of the emitted photon is below the Ly_α.*

Continuum lowering and pressure ionization

The interaction between charged particles results in a decrease of the ionization potential of bound electrons. Depending on the plasma density, there are different regimes of this effect called continuum lowering [59]. At low density, continuum lowering is a consequence of the shielding effect of free electrons in the plasma. In this regime, the ionization potential depression ΔE is approximately [144]

$$\Delta E \approx ze^2 / \lambda_D \quad , \tag{4.81}$$

where e is the electron charge, z is the ion charge +1 and λ_D is the Debye length.

At high density, the ion sphere radius r_i given by

$$r_i = (4\pi n_i/3)^{-1/3} \tag{4.82}$$

is smaller than the Debye length, and shielding appears in the vicinity of each ion individually. In this so called ion-sphere regime, the ionization potential depression is [144]

$$\Delta E \approx ze^2/r_i \quad . \tag{4.83}$$

At high density, the ionization potential depression can be higher than the vacuum ionization potential of bound electrons. Under these conditions, the bound states do not exist anymore and matter gets pressure ionized. Pressure ionization can be explained as a consequence of the overlap of higher orbitals of adjacent ions in dense plasmas as indicated in Fig. 4.19. Due to the overlap of the n>3 orbitals, the electrons in these states are effectively free.

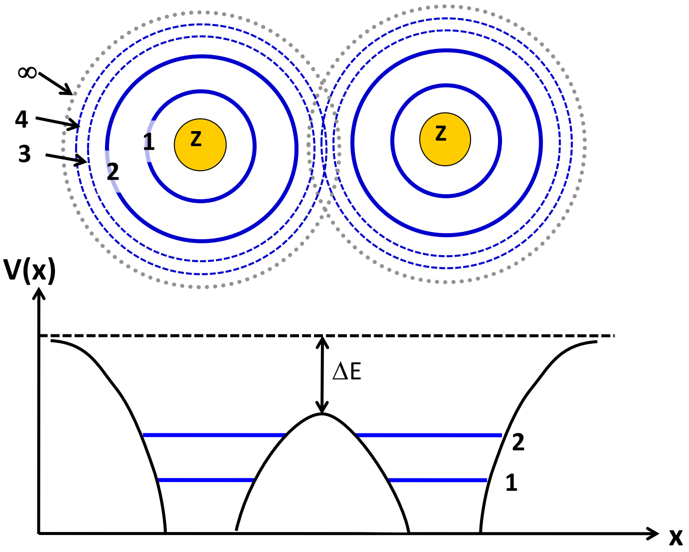

Fig. 4.19: *Pressure ionization in a dense plasma. At high density, the higher orbitals of neighbouring ions overlap, and consequently these levels do not exist, anymore. The plot at the bottom represents the potential V(x) of a bound electron as a function of its x-coordinate. The ionization potential depression ΔE exceeds the ionization potential of the levels with a principal quantum number of n>2.*

Another effect contributing to the ionic potential depression is the Inglis Teller effect [116] where Stark broadening leads to an overlap of the higher levels in an individual ion. A detailed analysis of ionization potential depression in different regimes was carried out by Stewart and Pyatt [218]. Continuum lowering can be calculated over a wide range of plasma parameters using the empirical formula [144]

$$\Delta E = 2.16 \times 10^{-7} \frac{Z}{r_i} \left\{ [1 + (\lambda_D/r_i)^3]^{2/3} - (\lambda_D/r_i)^2 \right\} \ . \tag{4.84}$$

Here, ΔE is in units of eV and r_i is in units of cm.

4.11 Numerical description of plasmas

The analytical description of the dynamics of dense plasmas and the interaction of dense plasmas with intense laser beams is only possible for simple model cases. In general, the complexity of laboratory experiments with all the processes involved requires numerical description. The collaboration between experimental, theoretical and computational physicists has been very successful for a deeper understanding of laser plasma physics. A large number of computer models have been developed and have become indispensable for the quantitative analysis of experimental data and for the prediction of new phenomena. In this chapter, the types of computer simulations relevant to this work are summarized.

4.11.1 Hydrocodes

The dynamics of LTE plasmas is often dominated by the collective behaviour of the particles. In this case, the plasma is well described by fluid models where the state of the plasma is characterized by a number of hydrodynamic observables such as density, pressure, temperature and velocity. The dynamics of the plasma is determined by the Euler equations, i.e. the equation of continuity, the equation of motion and the energy equation, given either in Eulerian or in Lagrangian coordinates [59]. A separate treatment of the electron and ion fluids is possible. The interaction with laser pulses can be simulated by calculating the energy transfer from the electromagnetic field to the electron fluid. The assumption of LTE restricts the maximum laser intensities to a value of about 10^{17} W/cm^2. At higher intensities, kinetic effects become important leading to the deviations from LTE.

In the early days of laser plasma interaction, hydrocodes have been extensively used to investigate the interaction of nanosecond laser pulses with plasmas. With some modifications, the simulations have been extended to the regime of sub-picosecond laser pulses. An important example is the 1D Lagrangian hydrocode MULTI-fs. MULTI-fs is based on the 1D version of the multigroup radiation hydrodynamics code MULTI. Three major changes are implemented in MULTI-fs to optimize the code for the ultrashort pulse regime:

First, the Maxwell equations are solved numerically using an algorithm described in [35] instead of the WKB approximation used in MULTI (see Chapters 4.4.1 to 4.4.3). Using this modification, the pulse propagation can be accurately described even in steep density gradients.

The second modification refers to the calculation of the collision frequencies. At low temperatures, an analytical expression for the electron-phonon collisions is used, whereas the electron-ion collision frequencies from Equation (4.19) are used at high temperatures. An interpolation for the intermediate temperature range is used.

Third, MULTI-fs allows for different EOS tables for the electron and ion fluids. This is important because the ion and electron fluids are typically not in equilibrium during the interaction with ultrashort laser pulses. The energy transfer between electrons and ions is implemented using a characteristic electron-ion relaxation time, typically in the range between 10 and 20 ps.

4.11.2 EOS tables

For a closed treatment of the hydrodynamics, the equation of state (EOS) of the plasma has to be known. In many hydrocodes, EOS tables containing the pressure and energy for a grid temperatures T and densities ρ are used. The SESAME tables are an important example for a tabulated EOS database [105].

Simulations of laser plasma interactions require the knowledge of the EOS over a wide range of temperatures and densities. Many established, rigorous EOS models are only valid for a limited range in ρ-T space. In order to cover a wide range of plasma parameters, different models are incorporated in the SESAME tables of some important materials such as aluminium [105] and copper [238]. For the construction of the table, the EOS has to be interpolated at the boundaries between different models.

The adequate description of the hydrodynamics requires the thermodynamic consistency of the EOS tables, i.e. the first law of thermodynamics has to be fulfilled. Thermodynamic consistency can be expressed by the condition [59]

$$\frac{d(\varrho\epsilon)}{dV}+p-T\frac{dp}{dT}=0\ . \tag{4.85}$$

The construction of EOS tables from different models often results in thermodynamic inconsistencies, as Equation (4.85) cannot be strictly fulfilled at the boundaries between different models.

These inconsistencies can be avoided in global EOS models such as the quotidian equation of state (QEOS). The QEOS can handle a wide range of temperatures and densities based on the Thomas-Fermi (TF) model. The TF model solves self-consistently the potential around an ion and takes into account ionization, excitation, Fermi-degeneracy of the electrons and ion-ion interactions. To some extent, quantum mechanical effects such as the shell structure can be incorporated in TF models.

4.11.3 PIC codes

At high laser intensities exceeding 10^{18} W/cm^2, laser plasma interaction becomes relativistic and the plasma is far from thermodynamic equilibrium. In this case, kinetic modelling is required. The motion of electrons and ions in plasmas is determined by the self-generated electromagnetic fields given by the Maxwell equations. The force of the electromagnetic field on a particle with charge q and mass m is

$$\vec{F}=\frac{d\vec{p}}{dt}=q\left(\vec{E}+\vec{v}\times\vec{B}\right) \tag{4.86}$$

and the equation of motion is

$$\frac{d\vec{r}}{dt}=\frac{\vec{p}}{\gamma m} \quad . \tag{4.87}$$

In principle, the evolution of the fields and the trajectories can be calculated when the initial phase space coordinates of each individual particle and the initial fields strengths are known. Due to the huge number of particles even in a small volume laboratory plasma, this approach is computational prohibitive. However, it turns out that the plasma behaviour can be represented by a reduced number of macroparticles [26]. This approach, used by particle-in-cell (PIC) simulations, drastically reduces computational effort to a feasible level. Macroparticles can be considered as a cloud of real particles or as finite volume fluid elements in phase space. Following the trajectories of the macroparticles by integrating the equation of motion allows for the detailed calculation of laser plasma interaction including kinetic effects.

In PIC simulations, the Maxwell equations are solved for each time step on a spatial grid. For the integration of the equation of motion, the electromagnetic field has to be extrapolated from the grid to the particle coordinates. In addition, the contribution of the particles to the charge and current densities on the grid points has to be calculated. These operations are called field and particle-weighting, respectively. The simplest approach is the nearest grid point approach, corresponding to a rectangular shape of the macroparticles. Due to the finite macroparticle size, the collision frequency is drastically reduced and PIC simulations reflect the collisionless behaviour of the plasma [26]. Binary particle collisions can be implemented using Monte Carlo approaches [225].

PIC simulations have become an indispensable tool for modelling laser plasma interaction. Fully relativistic codes calculating the interaction in 3D have contributed to a more detailed understanding of laser plasma interaction and to the prediction of new phenomena. In this work, a number of PIC codes were used to analyze experimental results. The absorption of sub-10-fs laser pulses in solid targets was investigated by 2D simulations with the PSC code. Simulations of the propagation of relativistic, laser generated electron beams in dense plasma were carried out in 3D using the virtual laser plasma laboratory (VLPL) code [180]. Finally, the electron transport in cone targets was investigated with the PICLS code [206].

4.11.4 Collisional radiative codes

Collisional radiative codes calculating the atomic kinetics and the emission and absorption of radiation in plasma are indispensable tools for plasma spectroscopy. In principle, the atomic population dynamics can be derived by solving rate equations for each energy level and for each ion species present in the plasma. However, the computational effort for the numerical solution of the rate equations for the complete set of detailed atomic energy levels is enormous. In practice, an established approach is to solve the rate equations using a reduced number of atomic energy levels representing the most important physical processes in the plasma. In this way, physical observables can be calculated accurately with a reasonable computational effort.

In this work, XUV spectra emitted from dense, laser generated plasmas were analyzed with two codes. *K* shell spectra were interpreted with the FLY code suite [144, 147] which is limited to ion species with a maximum number of three electrons and with a maximum atomic number of Z=26 (iron). For *L* shell spectra, the FLYCHK code was used [50, 51, 145]. The numerical models incorporated in FLYCHK can treat elements with a maximum atomic number of Z=93 (neptunium) without limitations of the electron number. In this chapter, a short overview of the capabilities of the codes is given.

FLY

In the FLY code, detailed atomic data including ionization potentials and energy levels of the hydrogen, helium and lithium-like ions are used for the calculation of the atomic kinetics. Because detailed information of the beryllium-like to the neutral stages is not provided, these states are represented by the ground state having zero energy and an ionization potential taken from [124]. In the FLY code, three kinetic models are implemented solving the rate equations for the steady state, LTE or time dependent case.

For the calculation of the synthetic spectra, bound-bound, bound-free and free-free transitions are taken into account. The emissivities and opacities of the bound-bound transitions are calculated according to Equations (4.72) and (4.73). Detailed line shape calculations including Doppler and Stark broadening based on the impact electron, quasistatic ion model are possible. Bound-free transitions are calculated using hydrogenic cross sections and Gaunt factors as discussed in Chapter 4.9. Free-free transitions are treated in the formalism of Kramers [135]. Opacity effects can be taken into account assuming a 1D, planar geometry.

FLYCHK

In the FLYCHK code, detailed population distribution calculations are implemented for the hydrogen to lithium like ion stages. For elements with $Z \leq 26$, the original FLY energy levels are used, whereas the atomic energy levels for higher Z elements are obtained from the HULLAC code [11, 12]. For species with more than three electrons, a set of superconfigurations is used to calculate the population dynamics.

The FLYSPEC spectral model includes detailed calculations of the line emission from the hydrogen to lithium like species, similar to the FLY code. For the species with more than three electrons, the superconfiguration transition array (STA) model is used to calculate the emissivities and opacities [13]. Therefore, detailed line frequencies and widths are calculated with the Dirac-Hartree-Slater (DHS) atomic physics code JJATOM [44]. For the calculation of the synthetic spectra, FLYCHK redistributes the populations of the superconfiguration levels statistically among the DHS configuration levels.

5 Production of dense plasmas by isochoric heating

In the recent years, there is an increasing interest in laboratory experiments investigating dense plasmas in the context of astrophysics, fusion research and high pressure science. Many of the experiments have become possible due to the development of high power laser systems. Various methods for the production of dense plasmas probing different regions of density-temperature space were developed.

Dense plasmas are produced by strong shocks driven with intense laser pulses [53, 112] or flyer plates [131]. Using the Hugoniot relations, the pressure and density of the shock wave are obtained by measurements of the shock speed and the particle velocity behind the shock [250]. Alternatively, the impedance matching technique allows for the derivation of the post shock density and pressure by comparing the shock velocity in the sample with the velocity in another material with well known EOS [59]. Shock experiments render possible the measurement of the equation of state along the Hugoniot at high pressures exceeding 100 Gbar [53, 131].

Shock waves are typically associated with a strong increase of temperature. For the production of dense plasmas with lower temperatures, shockless quasi-isentropic compression experiments (ICE) were developed. In ICE, quasi-isentropic compression is achieved by applying a smooth, increasing pressure to the sample. ICE driven with laser pulses is described, e.g., in References [63, 152, 210]. Dense plasmas were also produced by static compression in diamond anvil cells in combination with laser heating [69]. Pressures of up to 200 Gbar at a temperature of 4000 K are reported in [27].

Here, we focus on the production of dense plasmas by isochoric heating of solid density matter. Dense plasmas are generated by rapidly heating a sample on a time scale smaller than the time scale of the plasma expansion. For a sample with thickness d, this translates into a heating pulse duration τ of

$$\tau < d/c_s \tag{5.1}$$

where c_s is the ion sound velocity of the expanding plasma. Different types of heating pulses, such as optical photons, x-rays, electrons or ions, can be used for isochoric heating. The penetration depth of these pulses in solid matter varies from the nanometer range for visible laser pulses up to the centimetre range for high energetic electrons and protons. This is illustrated in Fig. 5.1 showing the penetration depth of optical photons, x-rays, electrons and protons in solid aluminium. The attenuation lengths of electrons and protons represent the CSDA (continuous slow down approximation) range obtained from the estar and pstar databases, respectively [22]. The x-ray attenuation length was calculated using the database of the Center for X-Ray Optics [102]. The attenuation length for laser irradiation was calculated using Equation (4.25).

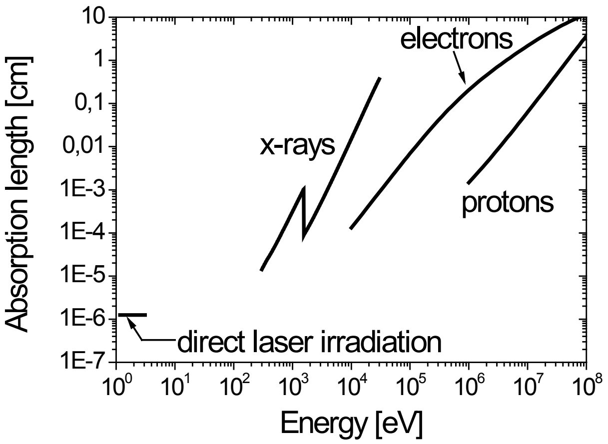

Fig. 5.1: *Absorption length of visible and infrared laser radiation, x-rays, electrons and protons in solid aluminium. Plot adapted from [166].*

Ultrashort laser are among the highest developed sources producing intense radiation pulses with sub-picosecond durations. However, isochoric heating with laser pulses requires laser systems with an optimized pulse duration and contrast. Without optimization, a preplasma with a scale length exceeding the electron skin depth is present during the interaction. This situation is schematically shown in Fig. 5.2 (a). The laser cannot penetrate into the solid region of the target. The laser energy is absorbed in the preplasma close to the critical surface where the density is much smaller than solid. The generation of dense plasmas relies on energy transport by heat conduction to the solid region.

For a direct energy transfer from the laser to the dense region of the target, preplasma scale lengths shorter than the electron skin depth are required. This situation is shown schematically in Fig. 5.2 (b). The laser penetrates into the dense region of the target and a thin layer of dense plasma with a thickness of the order of the electron skin depth is generated. In the past, these conditions could only be achieved with moderate laser intensities, typically smaller than 10^{14} W/cm^2. Direct laser heating has successfully been used to investigate the dielectric properties [6, 247] and the EOS [242] of dense plasmas with temperatures of the order of 10 eV.

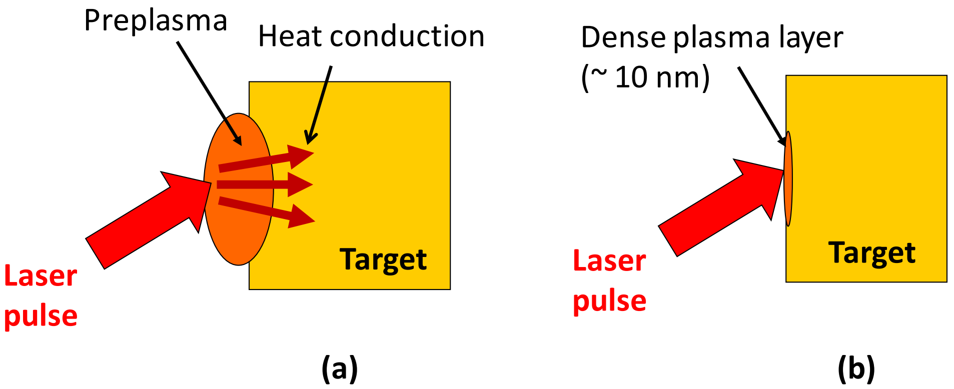

Fig. 5.2: *Two different regimes of the interaction of intense, ultrashort laser pulses with solids. (a) When the preplasma scale length exceeds the electron skin depth, the laser cannot penetrate into the solid region of the target. The laser energy is absorbed in the preplasma close to the critical surface where the density is much smaller than solid. (b) Isochoric heating is possible when the preplasma scale length is smaller than the electron skin depth. The laser directly interacts with the dense region of the target, and a thin, dense plasma layer is produced.*

Due to the short penetration depth of the laser into solids, the sample thickness is limited to a dimension of the order of 10 nm. The ion sound velocity of plasmas with a temperature of 100 eV is typically of the order of several 10 nm/ps, and the thin plasma layer expands on a picosecond timescale. This short lifetime of the plasma is a limitation for some experiments where conditions close to thermodynamic equilibrium are needed. Therefore, other types of heating radiation with higher attenuation lengths in dense matter were proposed.

Ultra-fast, volumetric heating with x-rays requires high brilliant sources of keV photons. Experimental studies investigating isochoric heating with laser generated K_α radiation are reported in [60]. Although calculations predict a significant contribution from the laser generated K_α photons, it was found that other heating sources such as electrons and protons were more efficient. A substantial improvement will be possible with the new generation of x-ray free electron lasers (XFELs) which are currently under construction at some facilities.

Isochoric heating with laser driven electron beams is one of the key issues in the FI scheme in fusion research. Recently, a number of studies have investigated isochoric heating of solid density matter with laser driven, relativistic electron beams. Depending on the experimental conditions, different processes contribute to heating. In thin foils, electron refluxing plays an important role [2, 158]. In thicker foils, heating is basically an effect of the resistive transport of return currents [200]. Heating with relativistic electron beams has also been demonstrated in wires attached to the tip of re-entrant cone targets [126]. The heating processes involve a number of complex phenomena. Self generated magnetic fields and instabilities may be associated with the transport of the electron beams. The effects on the electron transport and the energy transfer to the surrounding material are subject of topical research.

Another approach envisages isochoric heating with intense proton beams generated with intense laser pulses by target normal sheath acceleration. Protons with an energy of 10 MeV exhibit a penetration depth of more than 500 µm into solid aluminium. At to the source, the duration of the proton beam is close to the laser pulse duration, typically shorter than 1 ps. The total number of protons is of the order of 10^{12}. These properties make laser driven proton beams well suited for volumetric, isochoric heating of solids. Recently, the generation of dense plasmas with laser accelerated proton beams has been successfully demonstrated. WDM states with temperatures of about 20 eV were produced [5, 171]. Design studies using laser driven proton beams in the FI scheme in fusion research are reported in [126].

In this work, two methods for the generation of dense plasmas in different parameter regimes for spectroscopic studies and for equation of state measurements are presented. The first method is based on isochoric heating of solids with ultrashort laser pulses. For the experiments, an optimized laser system with a pulse duration of less than 10 fs and a high contrast is used. Unique experimental conditions with a nanometer preplasma scale length, significantly smaller than the electron skin depth, are achieved. Under these conditions, the laser energy is directly absorbed in a small layer with an initial thickness in the order of 10 nm as indicated in Fig. 5.2. The high density and the temperature of 200 eV make this kind of laser produced plasmas interesting for spectroscopic studies and opacity measurements in the context of astrophysics.

The second method pursued in this work is based on isochoric heating by laser driven proton beams. In this way, solid density aluminium plasmas with temperatures of 20 eV are produced [61]. The temperature and the expansion velocity of the plasma are measured with high temporal resolution. From these data, the EOS along the release isentrope is determined [80].

5.1 Production of dense plasmas with sub-10-fs laser pulses

Here, experiments generating dense plasmas with sub-10-fs laser pulses with a high contrast are presented. In the experiments, the Düsseldorf sub-10-fs laser system described in detail in Chapter 3.2.1 was used. Due to the high contrast and the short pulse duration, there is virtually no preplasma and the energy is transferred directly to the solid region of the target. This is confirmed in spectroscopic studies and absorption measurements. The series limit observed in *K* shell spectra from elements with a low atomic number clearly show that dense plasmas with peak temperatures in the order of 200 eV are produced [169, 170]. The strong absorption of p-polarized pulses close to grazing incidence confirms that unique conditions with extremely small values of the plasma scale-length are achieved. [42]. These properties make the plasmas produced with the few-cycle laser pulses interesting for opacity measurements and for basic studies of the interaction of intense electromagnetic fields with matter at high density.

5.1.1 XUV emission from dense plasmas generated with sub-10-fs laser pulses

For the characterization of the plasma conditions in the experiment, *K* shell spectroscopy was used. For the plasma temperature of about 200 eV, elements with a small atomic number are needed to obtain the hydrogen- and helium like species producing the *K* shell emission. Therefore, first experiments were carried out with carbon and boron nitride targets. Because the *K* shell emission from these elements is in the XUV wavelength range, an imaging XUV spectrometer with high detection efficiency was constructed [194]. A schematic drawing of the experimental setup is shown in Fig. 5.3.

The laser was focussed with an f/3 off-axis parabola. The focal spot with a diameter of 10 μm contained 50% of the laser energy resulting in a peak intensity of 3×10^{16} W/cm^2. The p-polarized laser is incident onto the target at an angle of 45°.

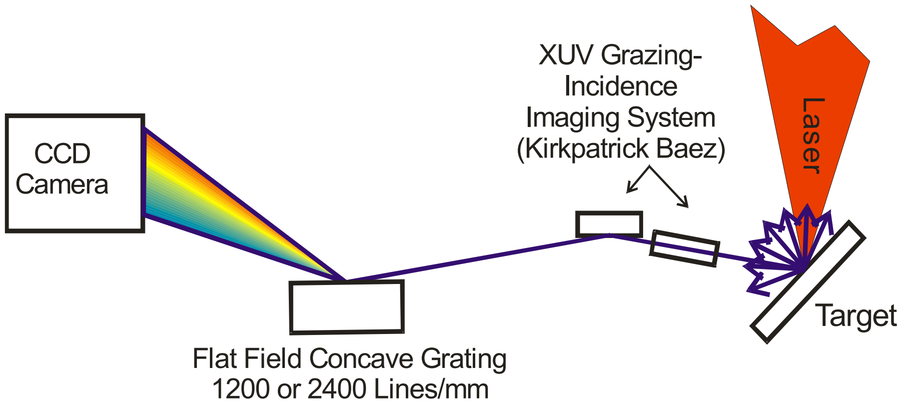

Fig. 5.3: *Schematic of the XUV spectrometer used for plasma diagnostics.*

The XUV emission from the plasma was imaged with a Kirkpatrick-Baez system [129] consisting of two gold-coated, spherical mirrors with a diameter of 2 inch. The first mirror (radius of curvature 7 m, grazing angle 2.2°) generated a line focus at the position of the spectrometer entrance slit, whereas the second mirror (radius of curvature 10 m, grazing angle 2.6°) imaged the plasma onto the detector plane in one dimension. Two different kinds of mechanically ruled, gold coated reflective flat-field gratings with a nominal number of 1200 [130] and 2400 lines/mm were used. The reciprocal linear dispersions were 0.6 nm/mm and 0.3 nm/mm, respectively. The spectra were recorded with an intensified CCD camera. In the image intensifier, the XUV light was converted into visible light using phosphor with a 100 nm Al coating. The CCD pixel size was 14 µm × 14 µm with a total number of 2048 × 2048 pixels. Depending on the signal strength, the XUV spectra were integrated over a time interval of up to 800 s, corresponding to a maximum of 8×10^5 laser shots. During the exposure, the target was moved laterally in order to keep the target surface in focus position. The resolution of the spectrometer was $\lambda/\Delta\lambda \approx 100$ at the wavelength of 5 nm.

XUV spectra obtained from a carbon target are shown in Fig. 5.4. The spectrum represented by the black line was obtained with the sub-10-fs laser pulses. The spectrum only consists of the C VI $1s$-$2p$ (C Ly$_\alpha$, 3.37 nm) and the C V $1s^2$-$1s2p$ (C He$_\alpha$, 4.03 nm) lines. There is a small contribution of the C V $1s^2$-$1s3p$ (C He$_\beta$, 3.50 nm) line in the spectrum which is only slightly above the noise level. This spectrum is compared to a second carbon spectrum obtained with a frequency doubled Nd:YAG laser with a pulse duration of 8 ns and an energy of 120 mJ in the same experimental setup in Fig. 5.4. In that spectrum, the whole series including the recombination continuum are observed.

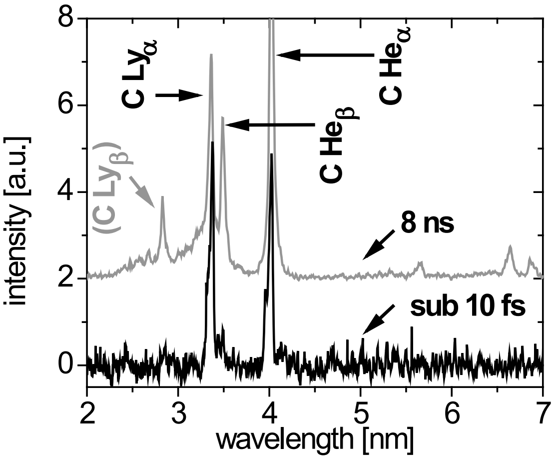

Fig. 5.4: *XUV emission from a carbon plasma. Black line: sub-10-fs laser pulses, grey line: 8 ns laser pulses (shown with an offset). For the sub-10-fs laser pulses the plasma is at high density, and a series limit is observed. In contrast, the whole series including a recombination continuum are emitted for the case of the 8 ns laser pulses.*

Similar results were obtained from BN targets. A typical XUV spectrum obtained with the sub-10-fs laser pulses is shown in Fig. 5.5.

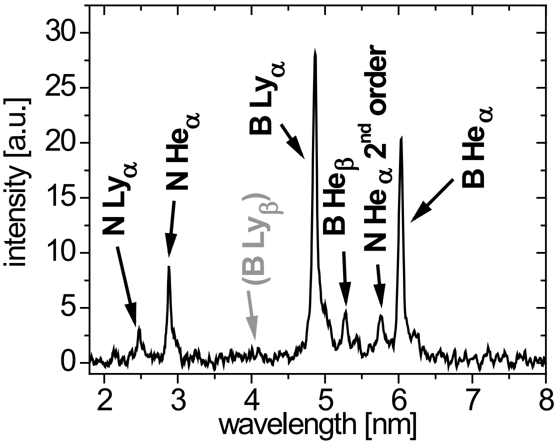

Fig. 5.5: *XUV spectrum from a dense boron nitride plasma generated with sub-10-fs laser pulses. Due to the high density, the higher series lines including the B* Ly_β *are suppressed.*

In the spectrum, the N VII $1s$-$2p$ (N Ly_α, 2.48 nm), N VI $1s^2$-$1s2p$ (N He_α, 2.88 nm), B V $1s$-$2p$ (B Ly_α, 4.86 nm), B IV $1s^2$-$1s2p$ (He_α, 6.03 nm) and the B IV $1s^2$-$1s3p$ (B He_β, 5.27 nm) are labelled. The higher series lines, for instance the B Ly_β, are not observed.

The series limit observed in the spectra obtained from the sub-10-fs laser pulses indicate that the plasma is at high density and the higher lines are suppressed by pressure ionization. The plasma conditions during the emission of the XUV spectra can be estimated using Equation (4.84). To this end, the ionization potentials of the hydrogen and helium-like levels in boron are plotted versus density for three different temperatures in Fig. 5.6. According to the observed spectral lines, the calculation was carried out for an average ion charge of $\overline{Z} = 4.5$. For a temperature of 100 eV, a density of ρ>0.36 g/cm^3 is required for the suppression of the B Ly$_\alpha$. On the other hand, the observation of the B He$_\alpha$ requires a density of ρ<1.37 g/cm^3. In the same way, it is estimated that the density is higher than 0.55 g/cm^3 for the carbon plasma.

Slightly different values of the density were estimated using the IMP code described in [189]. In these calculations the Schrödinger equation is solved for different orbitals. The potential around the ions in the plasma is calculated using the high-temperature Thomas-Fermi model. For a temperature of 100 eV the range of densities which allow for the emission of the Ly$_\alpha$ and suppress the Ly$_\beta$ lines is between ρ_{min} = 0.3 g/cm^3 and ρ_{max} = 0.8 g/cm^3 for BN and between ρ_{min} = 0.2 g/cm^3 and ρ_{max} = 1.3 g/cm^3 for C.

It is noted that some of the resonance lines in Fig. 5.5 exhibit a shoulder towards the long wavelength range. These features are attributed to the emission of dielectric satellites.

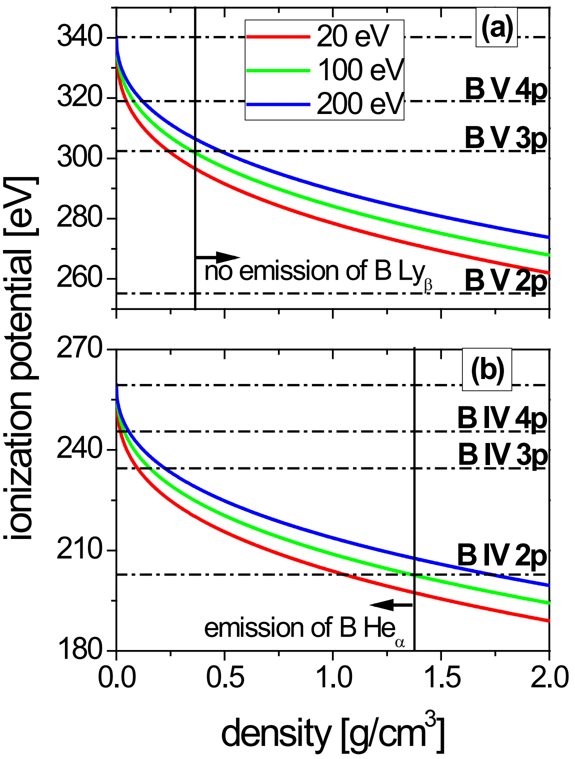

Fig. 5.6: *Ionization potential depression as a function of density in hydrogen and helium-like boron for three different temperatures. The unperturbed energy levels are indicated by the dash-dotted lines. At high density, the higher levels are removed by pressure ionization.*

Although these calculations are very useful for a rough estimation of the plasma conditions, more sophisticated calculations are required for a detailed understanding of the XUV emission. Therefore, computer simulations including the energy transfer from the laser to the plasma, the hydrodynamic expansion of the plasma during the emission, the highly transient nature of the plasma, line broadening and opacity effects were carried out [169].

In the first step, the expansion of the plasma was calculated with the 1D Lagrangian hydrocode MULTI-fs [66]. For the simulations, a prepulse was implemented in the hydorcode to investigate potential effects of a preplasma. The temporal grid t_j for the simulations was chosen with intervals of $\Delta t_j = t_{j+1} - t_j$ ranging from 0.1 fs close to the laser peak to larger values before and after the peak. The target was subdivided into a total of N=160 Lagrangian cells as shown in Fig. 5.7. A small layer size close to the target surface of 0.05 nm was chosen to resolve the high temperature and density gradients. The laser pulse was Gaussian in time with a FWHM duration of 8 fs. The equation of state was taken from the SESAME database.

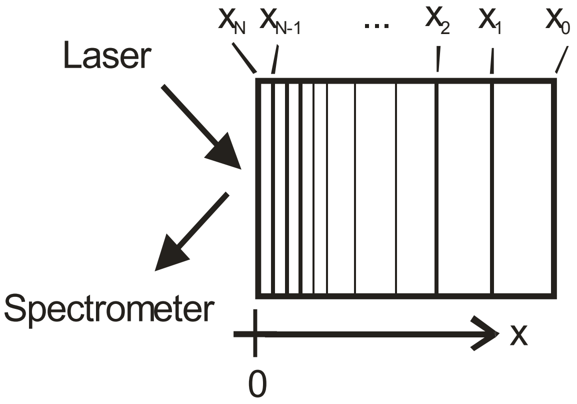

***Fig. 5.7:** Arrangement of the Lagrangian layers for the hydrodynamic simulation of the plasma expansion.*

As discussed in detail in Chapter 4.9, the radiative transport equation (4.64) has to be solved to calculate the XUV emission from the plasma. For this purpose, the emissivities ε_ν and opacities κ were calculated for each individual layer using the FLY code [147]. In the FLY simulation, the time dependent atomic kinetics, detailed line shapes and opacity effects were taken into account. The radiative transport equation was solved numerically using a standard finite difference scheme:

$$I_\nu(t_j, x_{k+1,j}) = S_\nu(t_j, x_{k+1,j}) + \exp(-\tau_{k+1,j}) \cdot (I_\nu(t_j, x_{k,j}) - S_\nu(t_j, x_{k+1,j})) \tag{5.2}$$

Here, $x_{k,j}$ denotes the position of the Langrangian layer with index k at the point of time with index j, $S_\nu = \varepsilon_\nu / \kappa$ is the source function and $\tau_{k+1,j} = \kappa(t_j, x_{k+1,j})(x_{k+1,j} - x_{k,j})$ is the optical thickness of layer number k+1. In this way, the intensity at the target front side $I_\nu(t_j,x_N)$ was obtained for each time t_j. Finally, the time integrated spectrum $D(\nu)$ was calculated by adding up the contributions of all times:

$$D(\nu) = \sum_j I_\nu(t_j, x_{N,j}) \Delta t_j \tag{5.3}$$

The simulations were carried out for different values of the preplasma scale length and the flux limiter. The best fit was obtained for a preplasma scale length of a few nm in agreement with the observations in [42] and for a flux limiter of f=0.001. The small value of f might be attributed to the small focal spot size resulting in 2D effects.

The electron temperature, mass density and electron density obtained for the carbon plasma for different times are shown in Fig. 5.8. The time t=0 corresponds to the laser peak. The corresponding time integrated XUV spectrum is shown in Fig. 5.9.

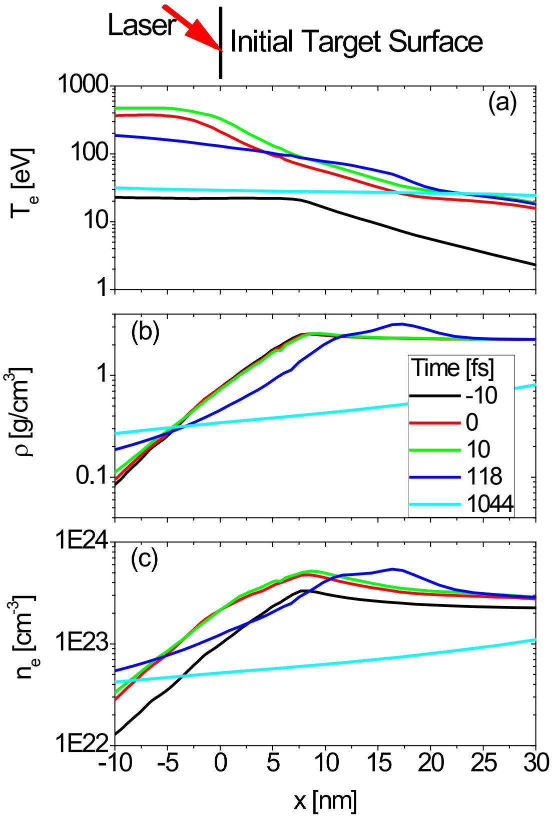

Fig. 5.8: *Hydrodynamic simulation of the temperature (a), mass density (b) and electron density (c) of a carbon plasma generated with sub-10-fs laser pulses. For details, see text.*

In the simulated spectrum only small contributions of the higher series lines are observed. The ratios of the Ly_β / Ly_α and He_β / He_α are smaller than 0.09 and 0.06, respectively. This is close to the noise level of the experiment, and consequently the lines are not observed in the measured spectra.

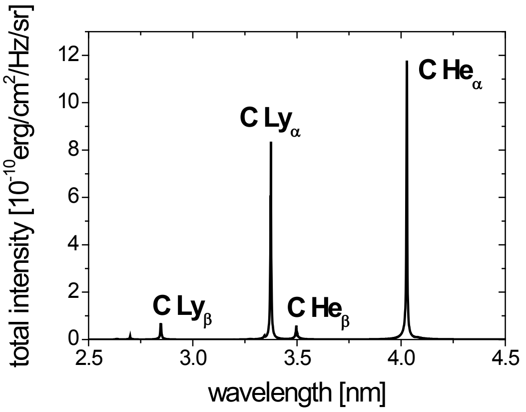

Fig. 5.9: *Time integrated XUV spectrum from a carbon target calculated with MULTI-fs and FLY simulations. The contribution of the higher lines is small due to pressure ionization during the XUV emission.*

In the hydrodynamic simulations, there is only a small preplasma scale length of a few nm at t=-10fs right before the laser pulse. Due to the small preplasma scale length, there is only a weak contribution of the low density part of the plasma to the overall XUV emission. The emission is dominated by the region of the plasma where the density is high and the higher series lines are suppressed by pressure ionization. At later times, the plasma scale length increases, but the plasma cools down quickly. This is demonstrated in Fig. 5.10, where the temperature and density histories of the Lagrangian layer number 92 with an initial position of x=2.7nm are plotted. Close to the laser peak, the temperature rapidly increases to about 200 eV. When the temperature is at its maximum, the density is still larger than 1 g/cm^3.

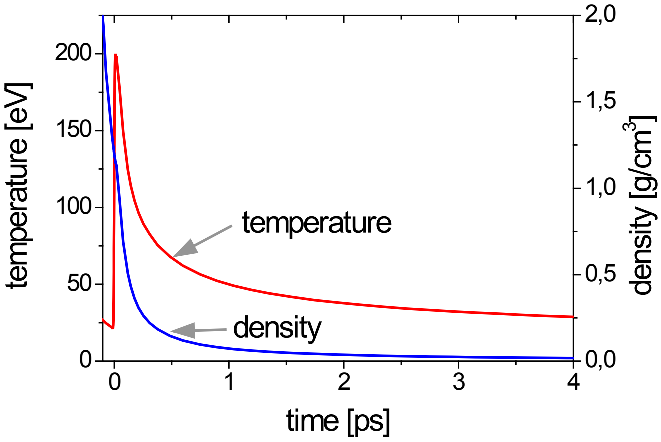

Fig. 5.10: *Temporal evolution of the temperature and density in the expanding carbon plasma. The plot shows the plasma conditions in the Lagrangian layer number 92 with an initial position of* x_0*=2.7 nm.*

The temporal evolution of the intensities of the C Ly$_\alpha$ and C He$_\alpha$ lines for layer number 92 are plotted in Fig. 5.11. The line intensities drop off with a time constant on a ps scale. Consequently, the emission of the hydrogen and helium-like resonance lines is predominantly from the period where the plasma is at high density.

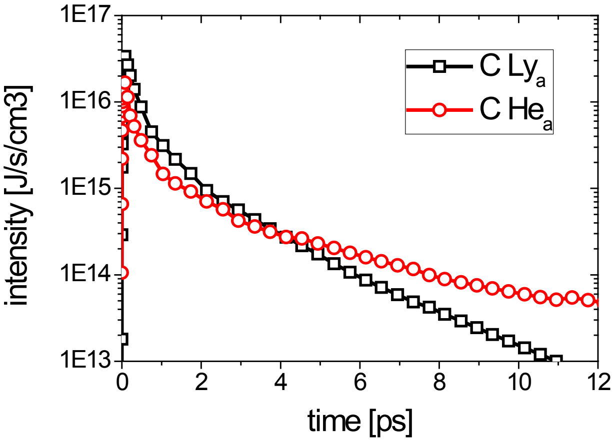

Fig. 5.11: *Intensities of the C Ly*$_\alpha$ *and C He*$_\alpha$ *lines in the expanding carbon plasma as a function of time. The intensities were calculated for the Lagrangian layer number 92 with an initial position of* x_0*=2.7 nm.*

In the simulations it was found that the thickness of the emitting plasma region is very small. For example, at the point of time 10 fs after the laser peak, the C Ly$_\alpha$ line is emitted from a region with a thickness of about 10 nm (FWHM). This value is in agreement with the expansion model in [170] where the initial thickness of the emitting plasma layer is equal to the electron skin depth.

Similar results were obtained for the BN plasma. In Fig. 5.12, the calculated ratios of the Ly_α / He_α lines are shown for B, C and N. The calculated values agree within the experimental error of 20% with the measured intensity ratios, indicating that the computer models used in this work are well suited for the calculation of XUV spectra generated with sub-10-fs laser pulses. Due to the small plasma thickness, all lines are optically thin at the point of time of the maximum emission, except for the N He_β with an optical depth of 1.2 [170].

It is noted that additional PIC simulations were carried out to analyze the absorption of the sub-10-fs laser pulses in the target (see Chapter 5.1.2). Although the PIC simulations are an ideal tool for analyzing the energy transfer to the plasma, the calculation of the XUV emission requires the calculation of the expansion over an extended period of time and target volume. Because this task would require a huge computational effort for PIC simulations, MULTI-fs was used for the analysis of the XUV spectra, instead. In the PIC simulations, it is shown that kinetic effects are important for a detailed understanding of the absorption mechanism. Although kinetic effects are not included in the hydrocode, a good agreement between experiment and calculations was obtained by fitting the values for the preplasma scale length and the flux limiter in the calculations. This is consistent with the results in [67], where a good agreement between the absorption measured in experiments and MULTI-fs and PIC simulations is reported.

It is interesting to mention that the ratio of the He_β/He_α lines measured in the experiment is larger for boron than for carbon, although under similar plasma conditions pressure ionization eliminates the B He_β at lower density. This observation is an effect of the smaller atomic number of boron. The He_β lines are emitted at a late stage of the plasma expansion when the temperature is low. Under these conditions, the $1s3p$ states are stronger populated for ions with a small atomic number, and consequently the intensity of the He_β is higher for B than for C.

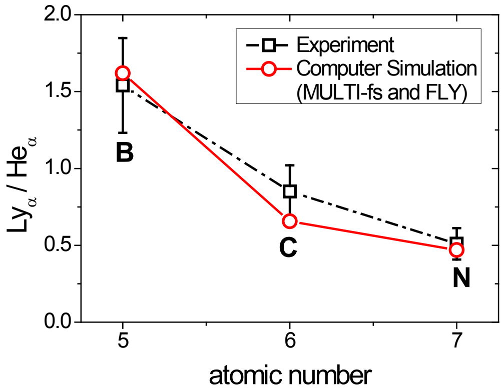

Fig. 5.12: *Ratios of the Ly_α/He_α lines for boron, carbon and nitrogen measured in the experiment (black boxes) and calculated with computer simulations (red circles). There is a good agreement within the experimental error of 20%.*

In order to investigate the effect of the laser intensity on the XUV emission, another experiment measuring the ratio of the B Ly_α/B He_α lines was carried out. The ratio of the Ly_α/He_α is sensitive to the plasma temperature and is therefore often used for plasma diagnostic. The laser intensity on the surface was varied by moving the target out of focus. Prior to the experiment, the Rayleigh length z_R was determined by imaging laser profile at different z-positions. A Rayleigh length of z_R=30µm was derived and was used to calculate the intensity at different z-positions. The measured intensity ratios are shown in Fig. 5.13 as a function of the laser intensity. In the range between 0.5 and $3 \cdot 10^{16}$ W/cm^2, the ratio increases almost linearly from 0.8 to 1.5. At smaller values of the intensity, the ratio drops quickly.

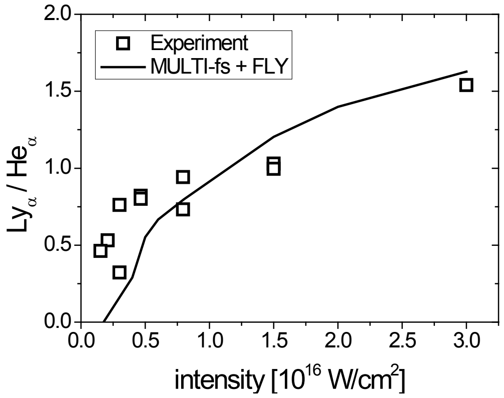

Fig. 5.13: *Ratios of the B Ly_α/B He_α lines for different laser intensities. Boxes: experiment, solid line: calculation. The decrease of the ratio at low laser intensity is due to the smaller plasma temperature.*

The ratios of the line intensities calculated with MULTI-fs and FLY are also shown in Fig. 5.13. There is a good qualitative agreement with the experimental data. Deviations are attributed to errors of the intensity scaling in the low intensity range.

The absence of the higher series lines is one of the most remarkable results of the *K* shell spectra from the low *Z* elements. Because the individual lines can be easily resolved, *K* shell spectroscopy is an ideal tool for plasma diagnostics. Besides the *K* shell spectra, it is interesting to investigate *L* shell spectra from higher *Z* elements in the same spectral range. Because *L* shell spectra contain a larger number of lines, they are more complicated and less suited for plasma diagnostics. However, they play an important role for the opacities in dense plasmas and for the radiative energy transport in the interior of stars. Due to the higher nuclear charge, the dimension of the orbitals is smaller, and it is expected that higher series lines are emitted. For Ti XIII, for example, Equation (4.84) predicts an ionization potential depression of about ΔE=72 eV at 0.25 times solid density and a temperature of 200eV. This value is much smaller than the ionization potential of 788 eV and does not lead to pressure ionization of the *M* shell electrons.

An XUV spectrum from titanium plasma generated with the sub-10-fs laser pulses at an intensity of 3×10^{16} W/cm^2 is shown in Fig. 5.14. For the interpretation of the spectrum, computer simulations were carried out. Because the FLY code is limited to a maximum number of three electrons, the superconfiguration code FLYCHK [50, 51] was used, instead.

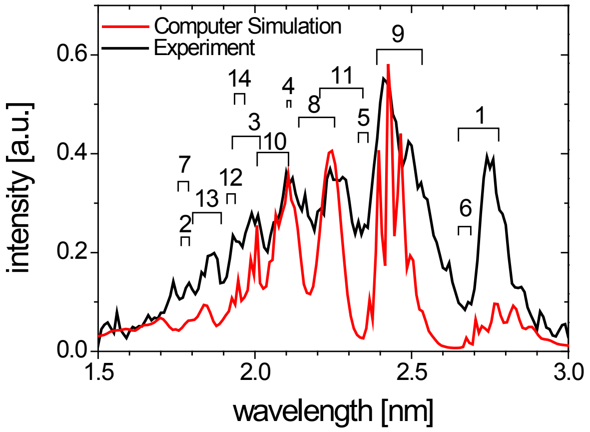

Fig. 5.14: *XUV emission from a titanium plasma generated with sub-10-fs laser pulses. Black line: experiment, red line: computer simulation. Some L shell lines are labeled. The labels are explained in Table 2.*

The temporal evolution of the plasma parameters was calculated with an expansion model described in [170]. In the model, a fraction f_{th} of the laser energy is converted to thermal energy within a layer with an initial thickness in the order of the of the electron skin depth δ_0. The plasma layer is initially at solid density (ρ_0=4.5 g/cm^3) and expands with the ion sound speed c_s. Assuming an adiabatic equation of state, a set of two coupled differential equations is obtained describing the laser absorption and the expansion of the plasma layer:

$$\frac{d}{dt}kT(t)=\frac{2}{3}\frac{f_{th}P_L(t)}{N}-(\gamma-1)\frac{c_s(t)}{\delta(t)}kT(t) \tag{5.4}$$

$$\frac{d}{dt}\delta(t)=c_S(t)=\sqrt{(Z+\gamma)kT(t)/M} \tag{5.5}$$

Here, k is the Boltzmann constant, N is the total number of particles (free electrons and ions) in the interaction volume, P_L is the incident laser power, γ =5/3 is the adiabatic exponent, M is the ion mass and $\delta(t)$ is the layer thickness. The first term on the right side of Eq. (5.4) represents heating of the plasma by the laser, whereas the second term is due to adiabatic cooling during the expansion. The temporal evolution of the laser power was calculated from the Fourier transform of the laser spectrum shown in Fig. 3.4. Equations (5.4) and (5.5) were solved numerically using an explicit Euler scheme. The density is obtained from $\rho(t)=\rho_0\cdot\delta_0/\delta(t)$, taking into account that the expansion can be considered as 1-dimensional as long as the plasma layer thickness is smaller than the focus diameter. The ion sound speed in Eq. (5.5) was calculated assuming an average ion charge of Z=8, which is consistent with atomic kinetics calculations. A value of f_{th}=25% was chosen for the calculations [170]. The temporal evolution of the plasma temperature and density are shown in Fig. 5.15. Similar to the results for the carbon plasma in Fig. 5.10, the temperature increases quickly to a value of about 200 eV and decreases on a picosecond time scale during the expansion. At the peak of the temperature, the density is about 3g/cm^3, which is still close to solid.

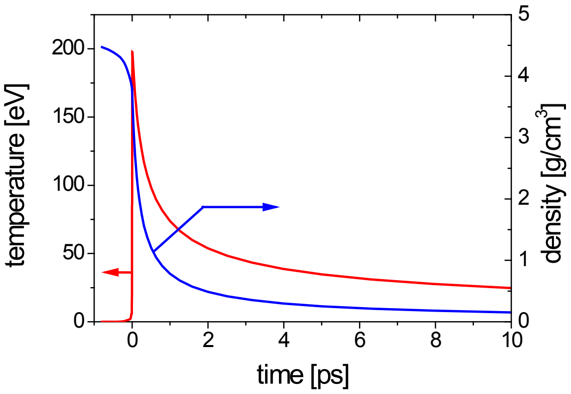

Fig. 5.15: *Temporal evolution of plasma temperature and density in the titanium plasma generated with sub-10-fs laser pulses, as calculated with an adiabatic expansion model.*

The plasma parameters calculated with the expansion model were then used as input for the FLYCHK calculations. The calculated, time integrated spectrum is also shown in Fig. 5.14. In the simulations, the XUV emission in the observed spectral range is basically from transitions from *L* shell excited stated to the ground state. The labels of the lines in Fig. 5.14 are explained in Table 2. There are contributions from the Ti XII to Ti XVII species to the measured spectrum. Basic features of the measured spectrum are reproduced by the calculations. The main difference from the measured spectrum is the smaller intensity in the wavelength range close to 2.74 nm. This might be attributed to the expansion model which considers only a single plasma layer. More precise results might be obtained from hydrodynamic simulations of the plasma expansion in combination with calculations of the *L* shell emission.

Although laser generated plasmas are highly transient, conditions close to LTE can be approached quickly at high density [9]. This has been confirmed in FLY simulations where LTE conditions were reached a few 100 fs after the laser peak. It is also interesting to calculate the ion-ion coupling parameter Γ_{ii} for the plasma conditions of our experiment. In the simulations Γ_{ii} is close to 1 for the BN and C plasmas, and significantly larger than 1 for the Ti plasma within a period of more than 10 picoseconds after the laser peak.

Label	Transition	Wavelength range [nm]
1	Ti XII $1s^22s^22p^63l$-$1s^22s^22p^53l'$	2.66-2.80
2	Ti XIII $1s^22s^22p^6$-$1s^22s^22p^55d$	1.77-1.79
3	Ti XIII $1s^22s^22p^6$-$1s^22s^22p^54l$	1.92-2.01
4	Ti XIII $1s^22s^22p^6$-$1s^22s^22p^53p$	2.10-2.11
5	Ti XIII $1s^22s^22p^6$-$1s^22s^22p^53d$	2.34-2.40
6	Ti XIII $1s^22s^22p^6$-$1s^22s^22p^53s$	2.66-2.70
7	Ti XIV $1s^22s^22p^5$-$1s^22s^22p^44d$	1.76-1.79
8	Ti XIV $1s^22s^22p^5$-$1s^22s^22p^43d$	2.13-2.25
9	Ti XIV $1s^22s^22p^5$-$1s^22s^22p^43s$	2.37-2.53
10	Ti XV $1s^22s^22p^4$-$1s^22s^22p^33d$	2.01-2.11
11	Ti XV $1s^22s^22p^4$-$1s^22s^22p^33s$	2.21-2.34
12	Ti XVI $1s^22s^22p^3$-$1s^22s^22p^23d$	1.90-2.01
13	Ti XVII $1s^22s^22p^2$-$1s^22s^22p3d$	1.80-1.88
14	Ti XVII $1s^22s^22p^2$-$1s^22s^22p3s$	1.94-1.97

Table 2: *List of transitions from L shell excited levels contributing to the XUV emission of the titanium plasma.*

5.1.2 Absorption of sub-10-fs laser pulses in solid targets

The energy transfer from the laser to the plasma is a fundamental question. Experiments highlight the role of the preplasma and the hydrodynamic expansion during the interaction [75, 179, 201]. The absence of the higher series lines in the XUV spectra discussed in the previous section indicates that there is virtually no preplasma during the interaction of the sub-10-fs laser pulses with the target. It is interesting to investigate the energy transfer to the target under these conditions. Therefore, additional experiments investigating the absorption of the sub-10-fs laser pulses over a wide range of intensities and angles of incidence have been carried out [42].

A schematic drawing of the setup is shown in Fig. 5.16. The target is mounted in the center of an integrating sphere. The integrating sphere collects the light that is specular and diffuse reflected from the target. The intensity is measured with a fast photo diode connected to the sphere via an optical fiber. Prior to the experiment, the linearity of the detector was confirmed. The signal on the detector is proportional to the amount R of reflected laser energy. The fraction of absorbed energy is $A=1-R$. Because a smooth surface is essential for a well defined angle of incidence, optical quality glass substrates with an aluminium coating were used.

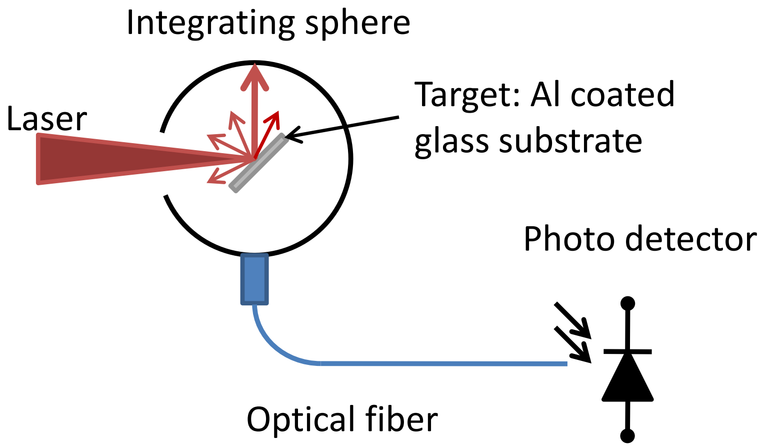

Fig. 5.16: *Experimental setup for the absorption measurement. The target is mounted inside an integrating sphere. The diffuse and specular reflected light is measured with a photo detector which is coupled to the integrating sphere via an optical fiber.*

The absorption for different angles of incidence at a laser intensity of 5×10^{16} W/cm^2 are shown in Fig. 5.17. Each point in Fig. 5.17 is averaged over 10-20 shots. The error bars represent the standard deviation. For all investigated angles, the absorption in p-polarization is higher than for s-polarization. The p-absorption increases from a value of 34% at an angle of 10° to 77% at an angle of 80°.

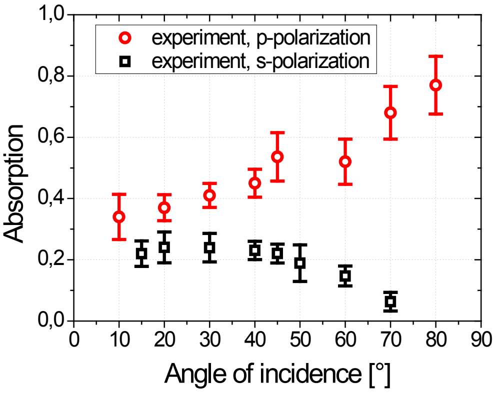

Fig. 5.17: *Absorption of sub-10-fs laser pulses incident on flat aluminium targets as a function of the angle of incidence measured with an integrating sphere setup. The increase of the p-polarized absorption towards higher angles indicates that the preplasma scale length is small.*

Besides the angular dependence, we also investigated the intensity scaling of the absorption. The intensity was varied by moving the target out of focus. The result is shown in Fig. 5.18 for an angle of incidence of 45°. For s-polarization, the absorption is nearly constant (10%) in the low intensity range up to a value of 10^{15} W/cm^2. It then increases to a value of approximately 20% at an intensity of 5×10^{16} W/cm^2. For p-polarization, the absorption is in the range of 10-20% for intensities smaller than 10^{14} W/cm^2. At higher intensities, the absorption increases and reaches a value of more than 50% at the highest intensity of 5×10^{16} W/cm^2.

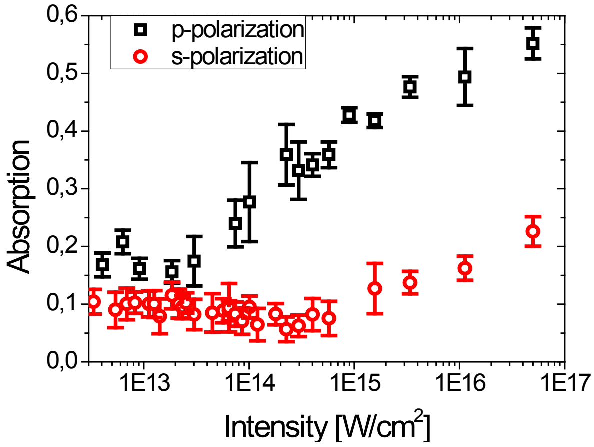

Fig. 5.18: *Absorption of the sub-10-fs laser pulses as a function of laser intensity measured in the experiment. The angle of incidence was 45° for p- and s-polarization.*

For the interpretation of the experimental data, 2D PIC simulations using the plasma simulation code PSC [28] were carried out. In the simulations, the aluminum target with the dimensions of 15 µm × 1 µm was placed in a 20 µm × 20 µm simulation box. The FWHM duration of the laser pulse with a Gaussian shape was 10 fs. Simulations were carried out for different values of the preplasma scale length L. The electron density profile at the target front side was chosen according to

$n_e(x)/n_{e0} = (1+\exp(-2x/L))^{-1}$. In order to account for the high contrast of the laser, the initial electron density in the cold target was set to zero, and optical field ionization using the ADK model [4] (see Chapter 4.1) was implemented in the calculations.

In order to compare the simulation results with the experiment, the collisionless absorption defined by the difference between p- and s-polarization is plotted versus the angle of incidence in Fig. 5.19. In the PSC code, an optional module calculating binary collisions using a Monte Carlo approach [225] is implemented. Here, simulations were carried out with and without binary collisions. The values obtained in the collisional simulations were only slightly larger than for the collisionless case, and similar results for the difference between p- and s-polarization were obtained. This indicates that the major absorption mechanism is of collisionless nature.

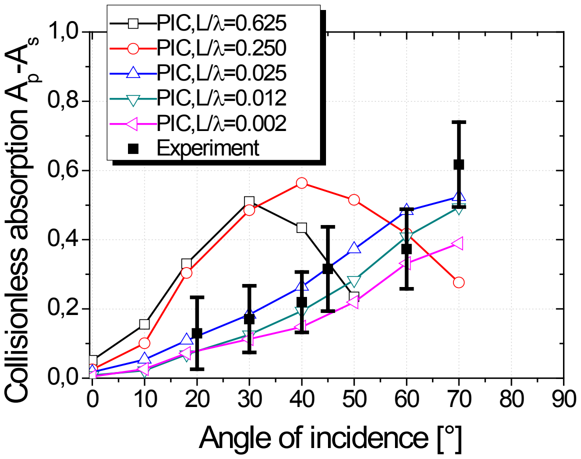

Fig. 5.19: *Collisionless absorption of the sub-10-fs laser pulses as a function of the angle of incidence. The open symbols represent PIC simulations for different preplasma scale-lengths L. The filled black squares represent the experimental data. A good agreement is obtained for a preplasma scale-length of the order of L/λ=0.01.*

The values of the collisionless absorption for large scale lengths (L/λ=0.625 and 0.250) follow the well known form expected for the case of linear resonance absorption with a maximum of the absorption at an angle of 30° and 40°, respectively. For smaller values of the preplasma scale length, the angle of the maximum absorption shifts towards larger values as discussed in Chapter 4.4.3. The best agreement between the simulations and the experimental data is obtained for a preplasma scale length of the order of L/λ=1%. This result confirms the interpretation of the XUV spectra in the previous chapter.

There are a number of collisionless processes which can potentially contribute to the absorption under our experimental conditions, such as sheath inverse bremsstrahlung [40], anomalous skin effect [246], vacuum heating [43, 89] or Brunel heating [38] (see Chapter 4.4.5). Although these processes are consistent with the small plasma scale length, their contribution to the absorption would be smaller than in the experiment [42]. Special attention was given to vacuum heating which has been investigated in detail by Gibbon [89]. In his calculations, a significantly smaller absorption is predicted under our experimental conditions. In addition, the predicted scaling of the absorption with the laser intensity is different from the experiment [42].

A new model of anharmonic resonance absorption was recently developed in Reference [161] (see Chapter 4.4.7). Anharmonic resonance absorption is a collisionless process which is efficient at high density gradients. Similar to the experiment, high values of the anharmonic resonance absorption are predicted close to grazing incidence. In addition, the threshold behaviour observed in the experiment (see Fig. 5.18) is consistent with the model. Therefore, the authors in Reference [161] come to the conclusion that anharmonic resonance absorption is the most promising candidate to explain our experimental results.

5.2 Production of dense plasmas with laser-driven proton beams

In the previous chapter, the production of dense plasmas with sub-10-fs laser pulses for spectroscopic studies was presented. The thickness of the sample which can be heated is limited by the electron skin depth and is of the order of 10 nm. The preparation of thicker layers of dense plasmas requires radiation with a higher penetration depth, such as protons. Here, the production of dense plasmas with laser driven proton beams for equation of state measurements in presented.

A schematic drawing of the experimental setup is shown in Fig. 5.20. The experiment was carried out at the at Titan laser at the Lawrence Livermore National Laboratory [236]. The 100 J, 500 fs laser pulse with a wavelength of 1 µm was focussed to a spot size with a diameter smaller than 10 µm onto a aluminium foil with a thickness of 17µm. A proton beam with a cut-off energy of about 50 MeV was generated by TNSA. The proton beam was incident onto a 2 µm aluminium sample target supported on a 25 nm SiN_3 and a 500 nm gold layer. A 400 µm gap separated the proton source from the sample.

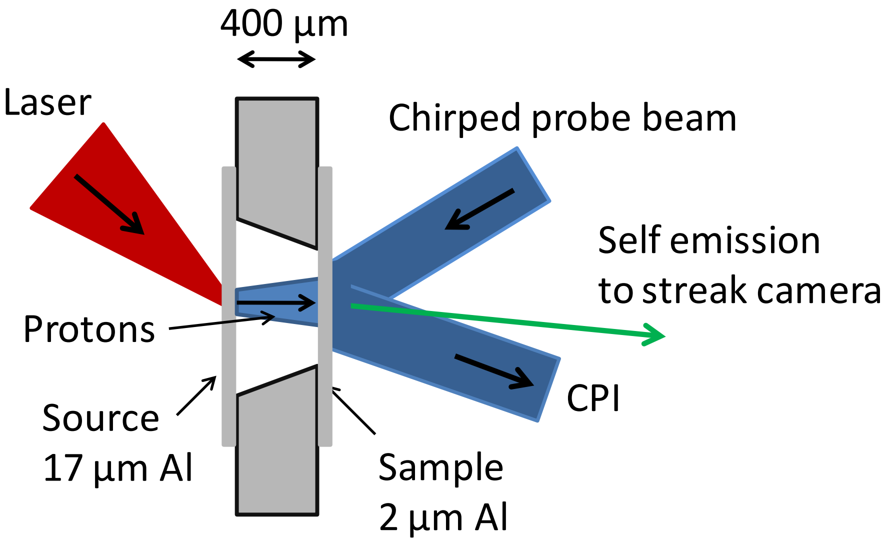

Fig. 5.20: *Experimental setup for the measurement of the equation of state of dense aluminium plasmas heated with laser driven MeV proton beams. The plasma temperature and density were measured simultaneously using a streaked optical pyrometer and a chirped pulse interferometer.*

The temperature of the expanding aluminium plasmas was measured using a streaked optical pyrometer (SOP) [5, 41, 171]. To this end, the visible light emitted from the rear side of the sample foil was imaged onto the entrance slit of a fast Hamamatsu C7700 streak camera with a resolution of 3 ps. A filter was used to select light at a central wavelength of 470 nm with a bandwidth of 10 nm. The imaging optics and the streak camera were absolutely calibrated at this wavelength, allowing for a direct measurement of the brightness temperature.

The expansion of the sample was investigated with a chirped pulse interferometer (CPI) [88]. A 5 mJ probe beam was extracted from the amplifier chain and stretched to a duration of 130 ps. As shown in Fig. 5.20, the CPI probe beam is incident onto the rear side of the sample foil at an angle of 15° with respect to the normal. The reflected probe beam was then relay imaged into a Mach-Zehner interferometer and onto the entrance slit of a high resolution imaging spectrometer.

A typical result from the SOP diagnostic is shown in Fig. 5.21.

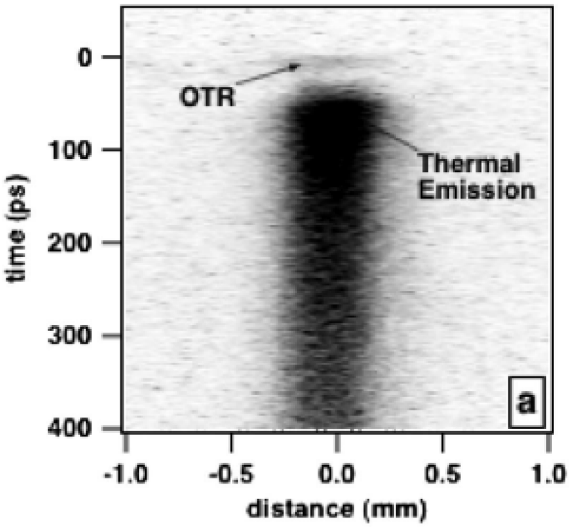

Fig. 5.21: *Time resolved measurement of the optical emission from dense aluminium plasma using streaked optical pyrometry. The optical transition radiation (OTR) at t=0 is emitted when fast electrons cross the rear side of the sample foil. The brightness temperature is derived from the thermal emission of the plasma.*

In the SOP data, the time zero is identified by the short duration emission of optical transition radiation (OTR) which is emitted when the fastest electrons cross the rear side of the sample foil. The thermal emission of the sample, related to proton heating, starts after a delay in the order of a few 10 ps, corresponding to the transient time of the protons across the vacuum gap.

An example image from the CPI diagnostic is shown in Fig. 5.22. The horizontal axis corresponds to the spatial dimension and the vertical axis to the spectral dimension.

The frequency of the linear chirped probe pulse translates into the linear time scale shown on the left side of the interferogram. In the undisturbed region of the interferogram, the fringes are equally spaced in the spatial dimension, whereas they are bent in the regions where the target expands. The expansion of the sample was derived from a Fourier reconstruction method applied to the interferometric data [88].

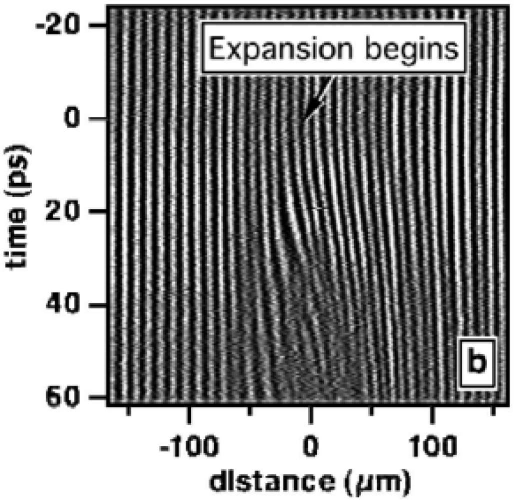

Fig. 5.22: *Expansion of the aluminium plasma measured with the chirped pulse interferometer. Bending of the interference fringes indicates the beginning of the expansion.*

For the further data analysis, the data in Fig. 5.21 and Fig. 5.22 was evaluated at different times in the spatial region of maximum temperature and expansion velocity. The result is shown in Fig. 5.23. The analysis reveals an expansion velocity approaching 5×10^4 m/s and a peak temperature of about 20 eV. This temperature corresponds to an ion-ion coupling parameter of Γ_{ii}=100 at the maximum density and Γ_{ii}=10 at the critical surface.

To compare the experimental data with different EOS models, computer simulations with the 1D Lagrangian hydrocode HYADES [142] were carried out. Proton heating was implemented using a time dependent source of energy into thermal electrons according to the measured proton energy spectrum and the NIST proton stopping power tables [22]. Because the total number of protons was not measured in the experiment, this parameter was used to fit the calculated brightness temperature to the experiment.

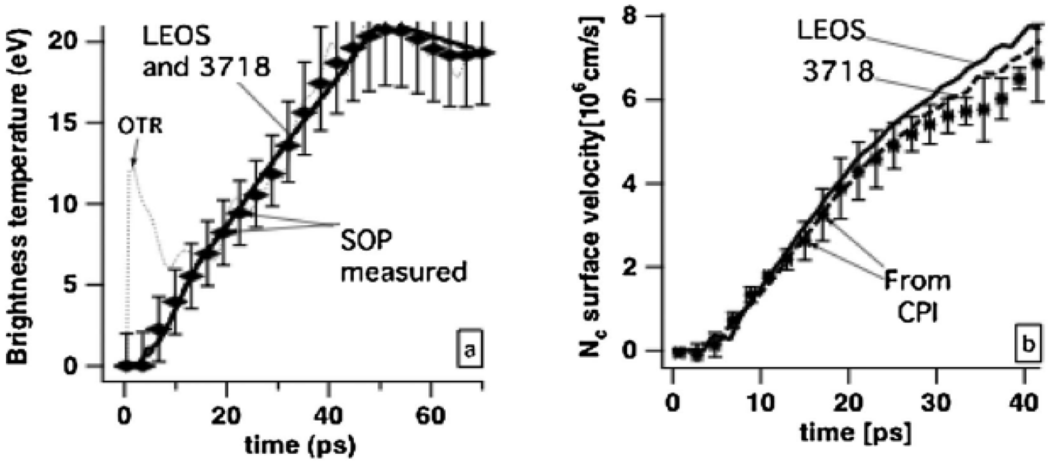

Fig. 5.23: *Brightness temperature (a) and expansion velocity (b) of the aluminium plasma. The experimental data (symbols) are compared the hydrodynamic simulations. Simulations were carried out using two different equation of state tables (LEOS: solid line, SESAME 3718: dashed line).*

In the simulations, the brightness temperature is given by the temperature at the critical density layer corresponding to the SOP wavelength and viewing angle. The temperature derived from the simulations for two different EOS tables (LEOS and SESAME 3718) is shown on the left side of Fig. 5.23. For both EOS tables, there is a good agreement with the measured temperature within the whole period of time covered by the SOP diagnostics. The expansion velocities of the critical density layer at the wavelength of the probe beam calculated with the hydrocode are shown as solid (LEOS) and dashed (SESAME 3718) line in Fig. 5.23 b. The expansion velocity derived from the SESAME 3718 tables fits the measured values over the whole time range, whereas deviations at late times are observed for the LEOS tables. This suggests that the SESAME tables calculate the EOS more accurately. However, it was possible to fit both the measured expansion velocity and brightness temperature calculated with LEOS to the experimental data by using a slightly different value for the total proton number. For both the SESAME and LEOS tables, the calculated temperatures and expansion velocities are accurate within an error of 18%.

These results demonstrate the potential of laser accelerated proton beams for EOS measurements in the WDM regime. It is expected that an improvement of the precision is possible, e.g. by using spectrally resolved SOP measurements in the visible or XUV wavelength range.

6 Generation of strong currents in dense plasmas

Due to its relevance to inertial confinement fusion, the development of strong x-ray sources and ion acceleration by target normal sheath acceleration, a large number of experiments have been carried out to study the generation and the transport of strong currents in dense plasmas. The scaling of the temperature with the laser intensity was derived using the bremsstrahlung and characteristic x-rays generated by the electrons in the target [18, 178, 198, 220] or the energy spectra of ions emitted from the target [18, 226]. The angular distribution of electrons emitted from laser irradiated foils was studied using nuclear activation techniques [198]. The transport of electron beams has been investigated by optical probing, [31, 96, 227] x-ray imaging [47, 96, 217] and by proton imaging [34]. More recently, laser driven electron beams were investigated using Cherenkov radiation [37, 216, 232] or optical transition radiation [16, 48, 85, 118, 199, 253].

From these experiments, important scaling laws, e.g. for the electron temperature as a function of laser intensity, have been obtained. However, so far no unique picture of the interaction has emerged from the experimental data. The acceleration and the transport of the electron beam depend on a large number of experimental parameters such as the laser pulse duration, intensity, polarization, plasma temperature, conductivity and the preplasma scale length. The investigation of the effect of the experimental conditions is subject of topical research.

An important issue is the optimization of the experimental conditions for the generation and the transport of strong currents. This is in particular true for the generation of strong currents driven by petawatt laser pulses in the context of fusion research. Recently, a number of studies were carried out to optimize the target design for the transport of strong currents. An enhancement of the electron flux was observed at the tip of laser irradiated, re-entrant cone targets. The transport of electrons along a wire attached to the tip of the cone was demonstrated [133]. In fusion experiments, a strong enhancement of the neutron yield was achieved by transporting electrons to the center of a pre-compressed fusion pellet via cone guiding [132]. In [78] the generation of protons by target normal sheath acceleration at the tip of cones with a flat top was investigated. An enhancement of the proton energy was observed and was explained by cone guiding, resulting in stronger electric fields in the Debye sheath.

Here, investigations of the generation and transport of electron beams in dense plasmas over a wide range of experimental parameters are presented. This includes ultrashort laser pulses with durations of only 40 fs and laser pulses with petawatt intensities. So far, only few experimental data is available in these regimes. The temperature, divergence and angular distribution of the electron beams are investigated in detail. The efficiency of different acceleration mechanisms and the effects of magnetic fields and instabilities on the transport are discussed.

Special attention was given to the optimization of the target design in terms of high electron fluxes. Advanced target concepts including cone and wedge shaped targets were investigated in experiments and computer simulations.

6.1 Generation of strong currents with ultrashort, multi-terawatt laser pulses

Many of the experiments investigating laser driven electron beams were carried out with pulse durations longer than 100 fs. At the present time, only few experimental data on the transport of electron beams produced with shorter laser pulses exist. In this chapter, experiments investigating the transport of strong currents driven with 40 fs laser pulses in planar metal targets are presented [48, 49]. The experiments were carried out with the THOR laser at the Texas Center for High Intensity Laser Science (see Chapter 3.2.2). A schematic of the experimental setup is shown in Fig. 6.1.

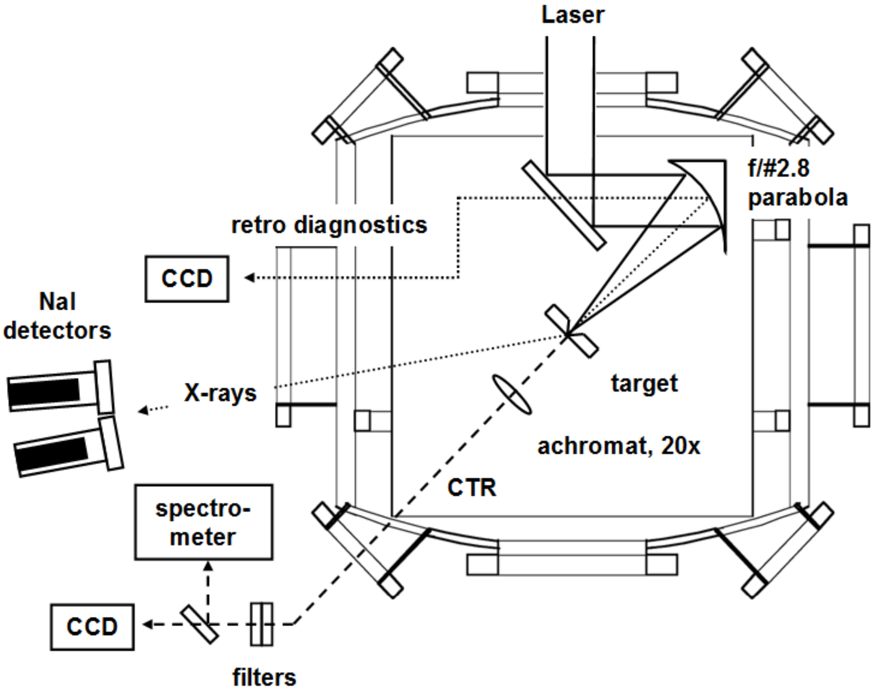

Fig. 6.1: Schematic of the experiment investigating the transport of electron beams in dense plasmas generated with ultrashort laser pulses.

The laser was focussed with an f/2.8 off-axis parabola. The focus diameter was 7 µm corresponding to a peak intensity of 2×10^{19} W/cm^2. The CTR emission from the target rear surface was imaged with 20x magnification onto a CCD camera using an achromatic lens. Neutral density filters were used to avoid overexposure of the camera. A part of the CTR emission was extracted with a beam-splitter after the lens and imaged onto the entrance slit of an imaging spectrograph. In this way, the spatial characteristics and the spectrum of the CTR were be observed simultaneously for each shot.

In addition, a multi-channel hard x-ray spectrometer was used to measure the bremsstrahlung emitted from the target. The spectrometer consisted of five NaI scintillating detectors located outside the target chamber at a distance of 3 m from the target. Lead filters with different thicknesses (0.0, 0.31, 0.95 and 4.8 cm) in combination with the 0.5 cm stainless steel target chamber wall resulted in x-ray cut-off energies of 85, 269, 413 and 916 keV, respectively. In this way, bremsstrahlung spectra were obtained in the energy range between 100 keV and 1 MeV for each shot.

In the experiments, planar metal targets with thicknesses between 10 μm and 40 μm were used. The interaction and the electron beam transport were characterized for two different angles of incidence of Θ=10° and Θ=45°.

6.1.1 Planar targets at 10° incidence angle

A typical image of the optical emission observed at the rear side from a planar aluminium foil with 10 μm thickness at an angle of incidence of 10° is shown in Fig. 6.2. In the image there is a single bright spot with a diameter of 6 μm FWHM. The spectrum of the optical emission is shown on the right side of Fig. 6.2. The spectrum with a bandwidth of 20 nm is peaked around 800 nm. This bandwidth is significantly smaller than the laser bandwidth also shown in Fig. 6.2, indicating that the observed signal is not laser light scattered into the imaging optics. This is reasonable because the laser pulse cannot penetrate the overdense aluminium plasma. For a foil thickness of 10 μm, it is estimated that the expanding plasma becomes underdense after a time of 10 ns, and thus direct laser light can be excluded as a source of the observed signal. It is noted that similar images were obtained in a configuration (not shown in Fig. 6.1) where the collection angle of the imaging optics did not overlap with the opening angle of the laser beam. It is also noted that experiments with different filter combinations and spectrometer settings were carried out to check for contributions in the spectral range at 2ω to the CTR fluence. However, the emission at the second harmonic could barely be distinguished from thermal plasma emission for an angle of incidence of Θ=10°.

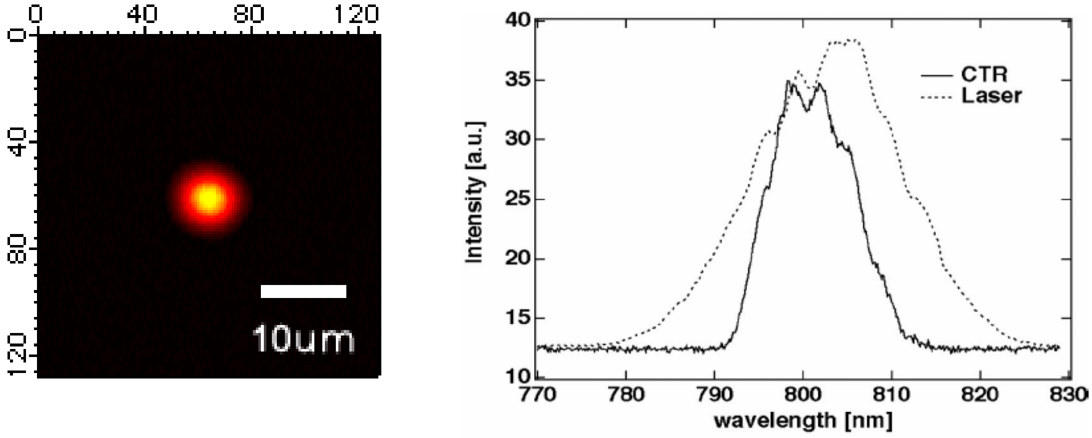

Fig. 6.2: CTR emission generated by a laser driven electron beam at an angle of incidence of 10°. Left side: Typical image of the CTR emission from the rear side of a 10 µm Al foil. The units at the image axes are pixel numbers. Right side, solid line: Spectrum of the CTR. The spectrum is peaked at 800 nm indicating that the electrons are bunched at the laser frequency. Dotted line: Laser spectrum.

These observations allow for the conclusion that the observed signal is CTR generated by hot electrons emitted from the target rear side [199]. The peak of the CTR spectrum clearly indicates that the electrons emitted from the foil are bunched at the laser frequency. This phenomenon is expected for some acceleration mechanisms such as resonance absorption and vacuum heating. Vacuum heating can only contribute to the energy transfer in steep plasma profiles when the electron quiver amplitude exceeds the plasma scale length as discussed in Chapter 4.4.6. For the intensity of 2×10^{19} W/cm^2, the quiver amplitude $eE/m_e\omega^2$ is smaller than 1 µm. Because this value is below the preplasma scale length of 3.5 µm (see Chapter 3.2.2), vacuum heating is not significant in this experiment. Therefore, it is concluded that resonance absorption is dominant at an angle of incidence of 10°.

The small spot size of the CTR emission indicates that the electron beam is well collimated over the propagation distance of 10 µm inside the foil. To analyze this aspect more in detail, the spot size was measured for different foil thickness. The result is shown in Fig. 6.3 for three different foil thicknesses of 10, 25 and 40 μm. The spot size increases only slightly with a divergence of approximately 4° from 10 to 25 μm and 8° from 25 to 40 μm.

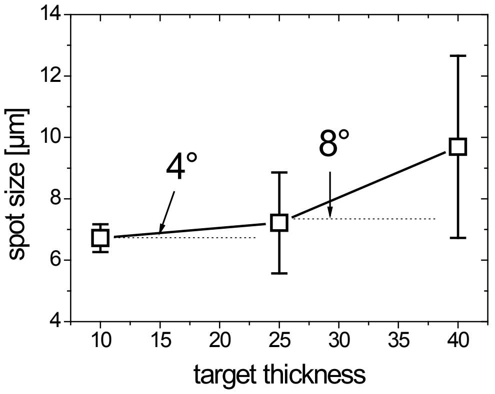

Fig. 6.3: *Spot size of the CTR emission versus foil thickness. The spot size increases only slightly with the foil thickness, corresponding to an opening angle of 4° at 10 μm and 8° at 25 μm.*

The x-ray yield measured with the NaI detectors from a 10 μm aluminium foil is shown in Fig. 6.4. Each data point represents the x-ray energy above the cut-off energy of the corresponding filter. To derive the electron temperature from the experimental data, the bremsstrahlung emitted from an ensemble of electrons with a single Maxwellian velocity distribution with temperature T_e was calculated. After convolution with the x-ray transmission of the filters, the calculated data was compared to the experiment. The best fit was obtained for an electron temperature of T=340 keV.

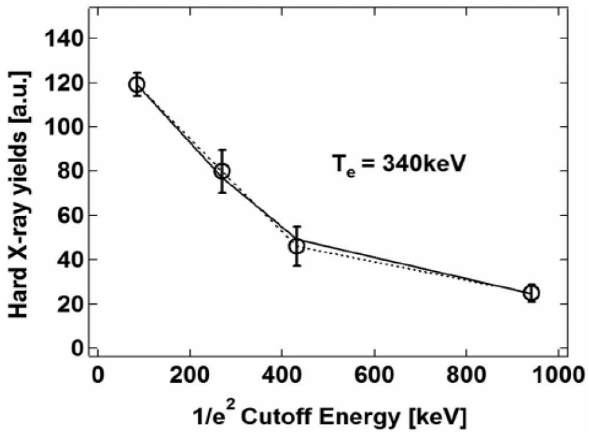

Fig. 6.4: *Bremsstrahlung x-ray spectrum from a 10 μm Al foil. Symbols and dashed line: experiment, solid line: calculation with an electron temperature of* T_e*=340 keV.*

As discussed in Chapter 4.6.2, it is expected that the CTR fluence decreases with increasing target thickness. This is confirmed in Fig. 6.5, where the CTR fluence obtained from several experimental runs with 10 and 25 μm aluminium foils is plotted. The error bars represent the standard deviation from a series of shots under identical experimental conditions. The measured CTR fluencies are reproducible from day to day. In Fig. 6.5 the fluence from the 25 μm foils is smaller than from the 10 μm foils by a factor of 4.7×10^{-3}.

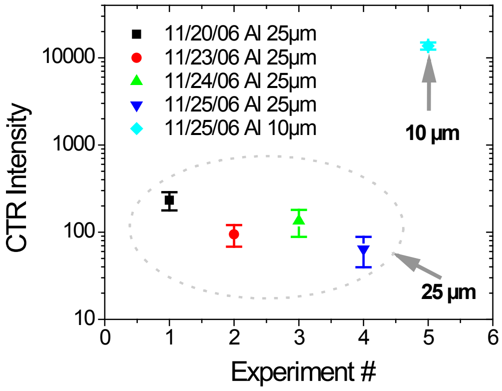

Fig. 6.5: *Measured CTR fluences from aluminium foils with thicknesses of 10 and 25 μm from different experimental runs. The measured CTR fluences are reproducible on a shot to shot base.*

From the measured CTR fluences, the electron temperature was derived using the 1D transport model introduced in Chapter 4.6.2. Therefore, the CTR fluences for the 10 and 25 μm foils were calculated for different electron temperatures T using Equation (4.44). The data from the 40 μm foils were not used in this analysis because they were obtained with a slightly different imaging setup. Because this has an effect on the detection efficiency, a direct comparison with the data from the thinner foils is not possible.

In the calculation, the temporal delay between two electron bunches is δT=2.67 fs corresponding to one electron bunch per laser cycle at the laser wavelength of 800 nm. The total number of bunches was M=15 corresponding to the pulse duration of 40 fs. The result is shown in the left side of Fig. 6.6. To derive the electron temperature in the experiment, the ratio of the 25 μm to the 10 μm foils calculated for different temperatures is shown on the right side of Fig. 6.6. The measured value, represented by the horizontal, solid red line, corresponds to an electron temperature of 290 ± 20 eV. The experimental error of 20% is indicated by the dashed, red lines. This value is close to the electron temperature of 340 keV derived from the bremsstrahlung spectrum. The scaling law in Equation (4.36) predicts a significantly higher electron temperature of 500 keV for an intensity of 2×19^{19} W/cm^2. It is noted that an electron temperature exceeding 500 eV was measured at a different angle of incidence of 45° (see Chapter 6.1.2). This result indicates that the angle of incidence is an important parameter for the energy transfer by resonance absorption.

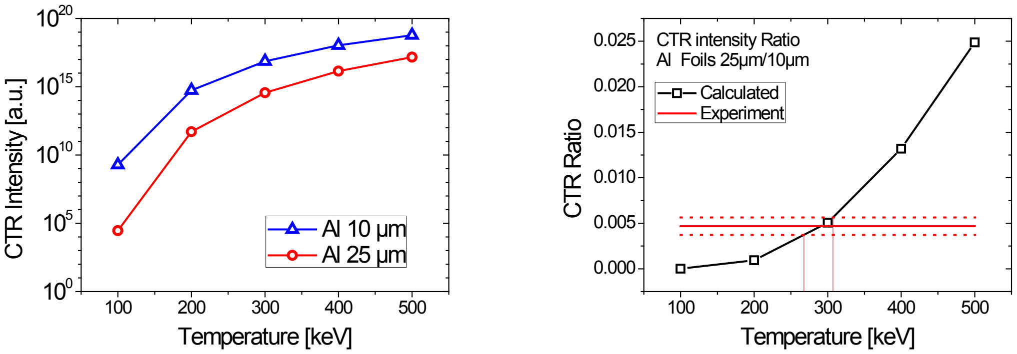

Fig. 6.6: *Left side: CTR fluences calculated for different electron temperatures with a 1D transport model for foil thicknesses of 10 and 25 µm. Right side: Ratio of the CTR fluences of the 25 to the 10 µm foil. Black line: calculation. Red line: experiment. The dotted line represents the experimental error. The measured signal ratio corresponds to an electron temperature of 290 ± 20 eV.*

It is noted that the divergence of the electron beam obtained from the CTR emission is smaller by almost a factor of 10 compared to experiments investigating the x-ray emission from the target [47]. This deviation can be explained by the different conversion efficiencies into CTR and K_α x-rays. The conversion efficiency for the K_α production has a maximum at electron energies of about 30 keV in [47], whereas the CTR is produced most efficiently by higher energetic electrons. This result indicates a stronger collimation of the higher energetic electrons. The small divergence of the electron beam is attributed to the self-generated magnetic fields [56, 227] as discussed in Chapter 4.6.3).

6.1.2 Planar targets at 45° incidence angle

In laser irradiated foils, the predominant electron heating mechanism crucially depends on the angle of incidence (see Chapter 4.4). Here, it is confirmed experimentally that different acceleration mechanisms contribute to the production of hot electrons at an angle of incidence of 45°. Fig. 6.7 shows the CTR image obtained from a 10 μm aluminium foil at 45°. The image is filtered with a 3 mm thick BG39 glass blocking the 800 nm light from the diagnostic. There are two distinct spots labelled A and B in the CTR image. The right side of Fig. 6.7 shows the spectrum of the CTR which is peaked at the second harmonic of the laser beam.

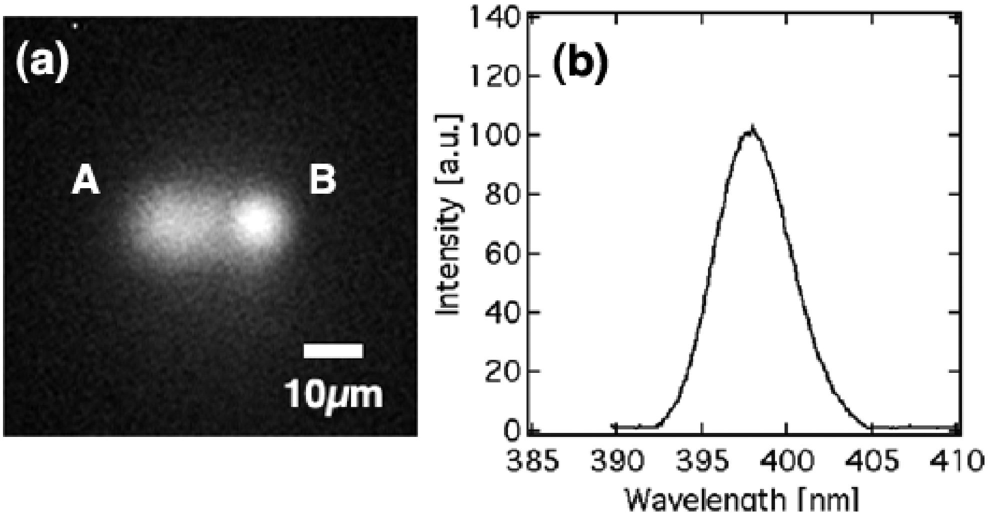

Fig. 6.7: *CTR emission generated by laser driven electron beams at an angle of incidence of 45°.Left side: Image of CTR obtained from a 10 μm Al foil at the second harmonic of the laser. There are two distinct spots labelled A and B resulting from different acceleration mechanisms. Right side: The CTR spectrum is peaked at 400 nm.*

The peak in the CTR spectrum clearly shows that the electrons are bunched at either the laser frequency (also resulting in CTR emission at 2ω) or at twice the laser frequency. The observation of two distinct spots at the target rear side can be explained assuming the two beams of electrons with different propagation directions are generated in the interaction zone at the target front side as indicated in Fig. 6.8. In the experiment, the position of spot B corresponds to the laser direction, whereas spot A corresponds to the target normal. This observation suggests that the electrons generating spot A were accelerated by resonance absorption, whereas the electrons in spot B were produced by $\boldsymbol{j} \times \boldsymbol{B}$ heating.

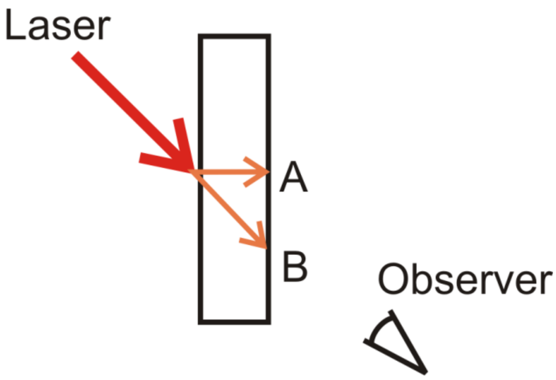

Fig. 6.8: *Schematic of the electron transport in the foil at an angle of incidence of 45°. Two electron populations propagating in different directions are generated in the interaction zone at the front surface. The beams generate two distinct spots of CTR at the target rear surface.*

In order to further characterize the two electron beams, the CTR fluence was measured as a function of laser intensity. The laser intensity was varied by changing the timing of the flash lamps of the pump lasers in the final amplifier.

The CTR fluences of each spot A and B were obtained from a horizontal lineout through the central region of the spots as shown in Fig. 6.9. The lineout was fitted with a double peak Gaussian function. The peak height of the Gaussian represents the CTR fluence of each spot.

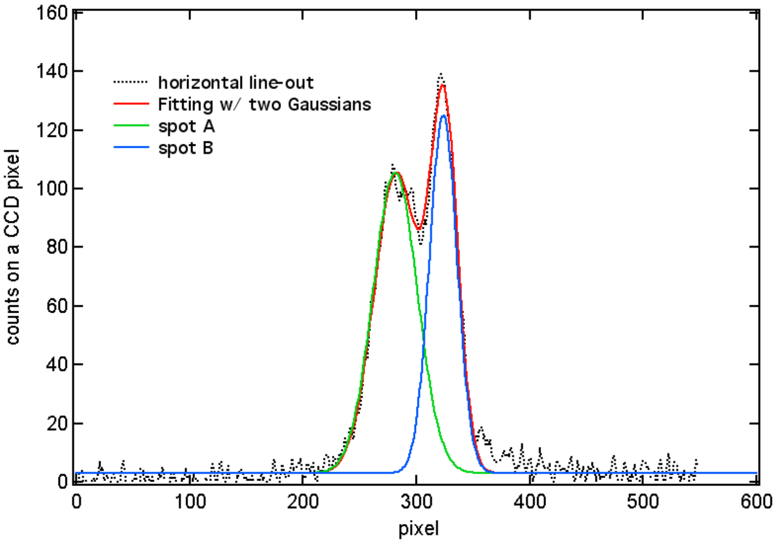

Fig. 6.9: *Lineout through the central regions of the spots A and B. The lineout was fitted with a two peak Gaussian curve. The peak heights represent the CTR fluences of the two spots and are used for further data analysis.*

The measured CTR fluences F_A and F_B are shown in Fig. 6.10 as a function of the laser intensity. To analyze the scaling of the CTR signal with the laser intensity, the fluences were fitted with power laws according to $F \propto I^{\alpha}$, resulting in α_A=4.6±0.3 for spot A and α_B=5.4±0.2 for spot B. In the following calculations, the indices A and B are used to distinguish between quantities related to spot A and B, respectively.

The measured CTR fluences were further analyzed with the ballistic transport model discussed in Chapter 4.6.2. Because the different emission angles of the two electron beams have to be taken into account, Equation (4.43) was used to calculate the CTR spectra around the second harmonic of the laser. The calculations require the input of the electron temperature T, the bunching frequency ω_b and the propagation length l of the electron beams. According to Fig. 6.8, it was assumed that spot A is produced by electrons accelerated by resonance absorption, corresponding to a bunching frequency $\omega_{b,A}=\omega_L$ equal to the laser frequency. The effective propagation length was set to l_A=13 µm, corresponding to the 10 µm target thickness plus the 3 µm preplasma at the target front side. The number of electron bunches is Λ_A=15 for the 40 fs laser pulses. The electron temperature was calculated using the scaling law given in Equation (4.36) [18].

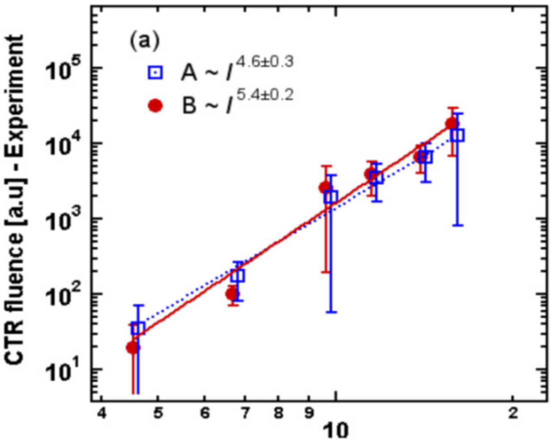

Fig. 6.10: *CTR fluences in spot A and B as a function of the laser intensity. Blue boxes and red circles: measured values, lines: fit with power law.*

Assuming that spot B corresponds to electrons accelerated by $\boldsymbol{j} \times \boldsymbol{B}$ heating, the bunching frequency was set to $\omega_{b,B}=2\omega_L$ corresponding to a total number of Λ_B=30 bunches. The propagation length is l_B=18.4 µm. The electron temperature was calculated from the scaling law for $\boldsymbol{j} \times \boldsymbol{B}$ heating given in Equation (4.37) [243]. Fitting the calculated fluences with a power law results in exponents of α_A=4.9 and α_B=5.9 which are close to the exponents derived from the experiment.

For an absolute comparison of the calculated CTR fluences, the number of electrons N_b in each bunch has to be known. Using the same number for both spots yields a CTR fluence which is about two orders of magnitude smaller for resonance absorption than for $\boldsymbol{j} \times \boldsymbol{B}$ heating. In the experimental data, however, the same fluences in spot A and B are observed at a laser intensity of about 8×10^{18} W/cm^2. The ratio of the numbers of electrons in each bunch for spot A and B can be derived by fitting the calculated CTR fluences to the experimental data. The best agreement was obtained for $N_{b,A}=10.6 \times N_{b,B}$. Taking into account that the ratio of the number of bunches is $\Lambda_A/\Lambda_B=0.5$, the ratio of the total number of electrons in each beam A and B was $N_A/N_B=5.3$, i.e. approximately 5 times more electrons are accelerated by resonance absorption. This result is in qualitative agreement with [198] where resonance absorption dominated when the plasma sale length was less then 10 µm. The CTR fluences calculated for this ratio of $N_{b,A}/N_{b,B}$ are shown in Fig. 6.11.

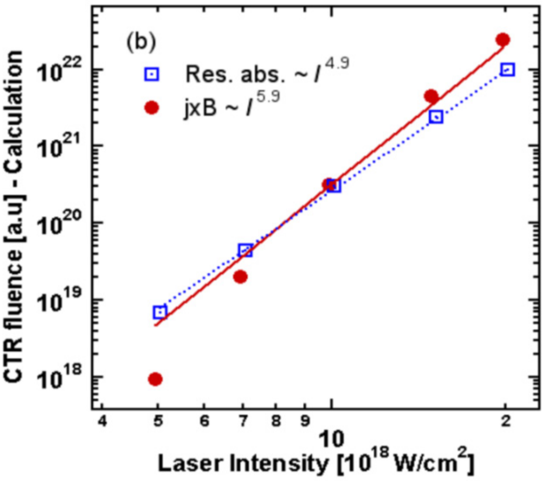

Fig. 6.11: *CTR fluences calculated with a ballistic transport model. The ratio of the numbers of electrons in each beam was fitted to the experimental data.*

For an experimental estimation of the electron temperatures in each electron beam, the CTR fluences were measured for two different foil thicknesses (10 and 20 µm). At a laser intensity of 2×10^{19} W/cm^2, the fluences from the 20 µm foil were smaller by a factor of 0.120 and 0.186 compared to the 10 µm foil for spot A and B, respectively. This result is compared to the ratio of the CTR fluences calculated for different temperatures using the ballistic transport model in Fig. 6.12. The measured ratio of the CTR fluences corresponds to a temperature of $T_A=0.78 \pm 0.02$ MeV for resonance absorption and $T_B=1.5 \pm 0.2$ MeV for $\boldsymbol{j} \times \boldsymbol{B}$ heating. At an intensity of

2×10^{19} W/cm^2, the scaling laws in Equations (4.36) and (4.37) yield temperatures of 0.5 MeV for resonance absorption and 1 MeV for $\boldsymbol{j}\times\boldsymbol{B}$ heating, which are roughly consistent with the experiment. The slightly higher temperatures derived from the CTR fluences might be a consequence of an intensity increase due to relativistic self-focusing in the underdense plasma (see Chapter 4.3).

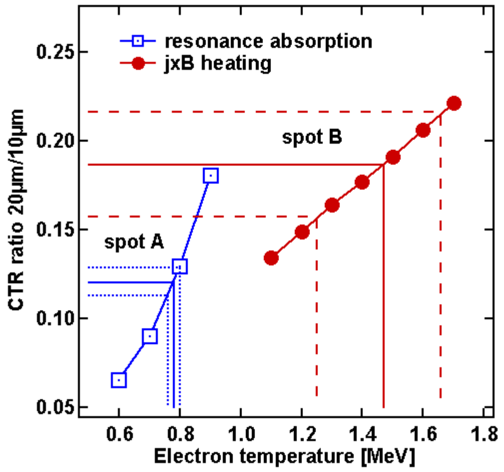

Fig. 6.12: *Ratio of the CTR fluences of the 20 µm to the 10 µm foils for spot A and B. Blue boxes: calculated for resonance absorption (spot A), red circles: calculated for* $\boldsymbol{j}\times\boldsymbol{B}$ *heating. The measured values including the experimental errors are represented by the horizontal lines.*

The interpretation of different acceleration mechanisms was confirmed in 3D PIC simulations using the fully relativistic Virtual Laser Plasma Laboratory (VLPL) code [180]. In the simulations, a Gaussian laser pulse $a = a_0\exp(-r^2/R^2)\exp(-t^2/T^2)\cos(\omega_0 t)$ was incident at p-polarization onto an overdense plasmas layer at an angle of 45°. The pulse duration, focus radius and wavelength were T=30 fs, R=6.7 µm and λ=800 nm, respectively. The amplitude of the normalized vector potential was a_0=5 corresponding to a peak intensity of 5.4×10^{19} W/cm^2. The electron density of the 9 µm thick plasma layer was 20 times overcritical. A linear density profile increasing from 0 to 20 times critical density over a distance of 3.5 µm at the target front side was implemented to simulate the preplasma. The simulation box was sampled with a grid of 250 × 237 × 20 cells with 8 particles per cell.

In the PIC simulations, two distinct electron populations were emitted from the target in different directions and in different time intervals. The temporal evolution of the energy spectrum of the hot electrons is plotted in Fig. 6.13. The first population is emitted in the time interval from 20 to 40 laser cycles. The second population with a smaller number of electrons, but with a higher temperature is emitted in the interval between 40 and 80 laser cycles.

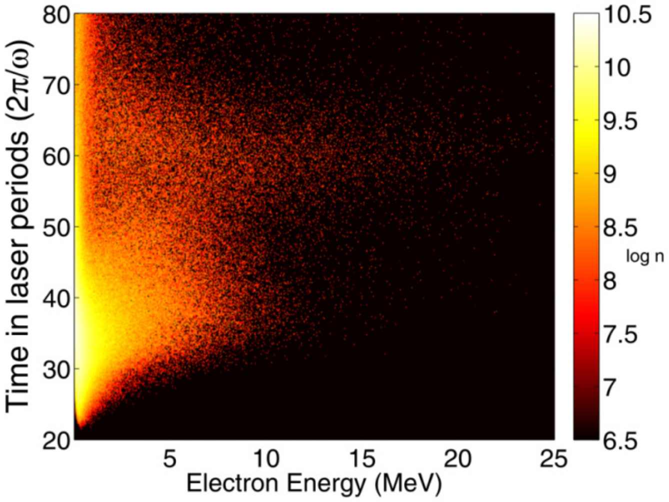

Fig. 6.13: *Time resolved energy spectrum of laser driven electron beams calculated with a PIC simulation. The angle of incidence is 45°. The colour bar represents the electron density on a logarithmic scale.*

The angular distribution of the two populations is shown in Fig. 6.14. In the period corresponding cycle 20-38, the angular distribution of the emitted electrons is peaked at 165°, close to the target normal. In contrast, the second population is emitted in the time interval from cycle 40-80 close to the direction of the incident laser beam.

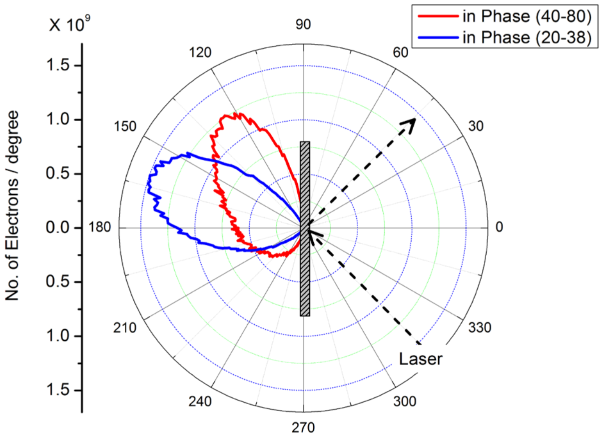

Fig. 6.14: *PIC simulation of the electron emission from a laser irradiated metal foil. Two electron populations are emitted at different angles in different time intervals.*

The energy spectra of the electrons in the angular intervals of 90-150° and 150-210° are plotted in Fig. 6.15. The electrons following the laser direction have a temperature of 3.3 MeV, whereas the electrons emitted close to the target normal have a temperature of 1.4 MeV.

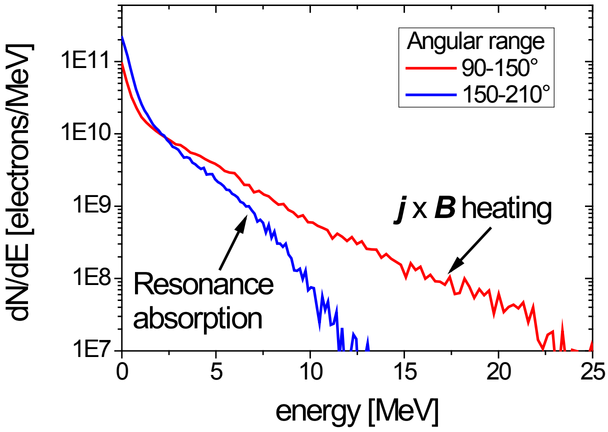

Fig. 6.15: *Energy spectra of the electrons emitted in normal direction (blue line) and in laser direction (red line) as calculated with the PIC simulation.*

These trends observed in the PIC simulations are in agreement with the experimental results. The observation of two distinct electron beams with different temperatures confirms the interpretation of different acceleration mechanisms. It is noted that similar observations are reported in Reference [232] where the emission of Cerenkov radiation and protons was investigated.

It is interesting to estimate the currents transported by the electron beams as discussed in Chapter 4.5. Using the temperatures obtained in the experiment (T_A=0.78 MeV, T_B=1.5 MeV) and the ratio of the total electron numbers of N_A / N_B = 5.3, the conversion efficiency for resonance absorption is higher than the efficiency for $\boldsymbol{j} \times \boldsymbol{B}$ heating by a factor of 2.8. Assuming a total conversion efficiency of η=20%, the number of electrons accelerated by resonance absorption is N_A=8.2×10^{11} electrons corresponding to a peak current of I_A=3.3 MA. The number of electrons accelerated by by $\boldsymbol{j} \times \boldsymbol{B}$ heating is N_B=1.5×10^{11}, corresponding to a peak current of I_B=0.62 MA. Both values are larger than the Alfvén currents of $I_{A,A}$=42.7 kA and $I_{A,B}$=66.7 kA, respectively.

6.2 Generation of strong currents with petawatt laser pulses

In the FI scheme of inertial confinement fusion, the generation of strong currents of the order of Gigaamperes with petawatt laser pulses is proposed. The transport of such huge currents far above the Alfvén limit in dense plasmas is widely unexplored. In numerical simulations, self-generated magnetic fields and the interaction with the plasma play an important role for the beam transport [55]. Computer simulations have predicted effects such as the filamentation due to the Weibel instability [108, 121] or anomalous stopping [107].

Here, experiments on the transport of electron beams generated with petawatt laser pulses incident onto dense foam plasmas are reported [118]. The transport was investigated using the CTR emitted from the target rear side. Electron temperatures in the MeV range were measured with an electron spectrometer. The CTR spectra clearly showed bunching of the electron beam. In the CTR images, the filamentation of the electron beam due to the Weibel instability was observed.

The experiment was carried out at the Vulcan petawatt laser at the Rutherford Appleton Laboratory. A drawing of the experimental setup is shown in Fig. 6.16. The laser pulses with an energy of 350 J, a duration of 750 fs and a wavelength of 1053 nm were focused with an *f*/3.2 off-axis parabolic mirror. The focal spot with a diameter of 6 µm contained 75% of the energy, resulting in an intensity of up to $5 \cdot 10^{20}$ W/cm^2. The transition radiation emitted from the target rear side was collected with a mirror and imaged with an *f*/2 lens system with 40 times magnification. Beam splitters in the imaging path were used to distribute the light to two cameras and two spectrometers. In this way spectra and images with different filter settings were obtained simultaneously with a single shot. In addition, a permanent magnet electron spectrometer covering the energy range of up to 40 MeV was set up in the laser forward direction at a distance of 3.7 m from the target.

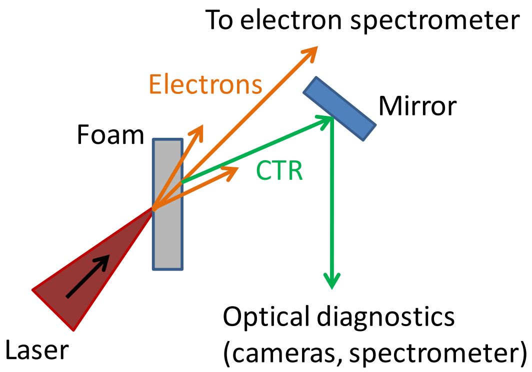

Fig. 6.16: *Experimental setup for the investigation of electron acceleration and transport with petawatt laser pulses. An electron spectrometer and the CTR emission were used for diagnostics.*

For the experiment, foam targets with different thicknesses (250, 500 and 750 μm) and different densities (100 and 200 mg/cm^3) were used. The target front surface was coated with a 75 nm gold layer. The high Z material efficiently converts laser light into x-rays and preheats the foam to a temperature of about 150 eV. The target rear side was coated with 200 nm of aluminium to maintain a sharp plasma-vacuum boundary required for CTR generation. The p-polarized laser pulses were incident onto the target at an angle of 45°.

A typical image of the optical emission from the target rear side is shown in Fig. 6.17 [118]. The image consists of a number of bright spots arranged on a ring, indicated by the dashed line. These spots are surrounded by a cloud of smaller spots.

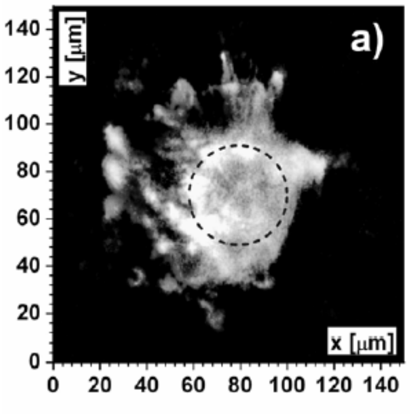

Fig. 6.17: *Image of the coherent transition radiation emitted from a foam plasma irradiated with a petawatt laser pulse. A number of spots are observed, indicating that the electron beam undergoes filamentation in the foam plasma.*

The spectra of the light emitted from targets with different thicknesses are plotted in Fig. 6.18 in the wavelength range between 490 and 580 nm. For the target with a thickness of 250 μm, a strong peak around 527 nm is observed. The peak in the spectrum indicates that the electrons are bunched either at the fundamental or at the second harmonic of the laser frequency. For the 500 μm target only a weak peak at

527 nm is observed, whereas the spectrum obtained from the 750 µm target only consists of the broadband OTR signal without any significant contribution from CTR. The ratio of the CTR peak height for the 500 µm to the 250 µm target is $CTR_{500}/CTR_{250}=0.01$.

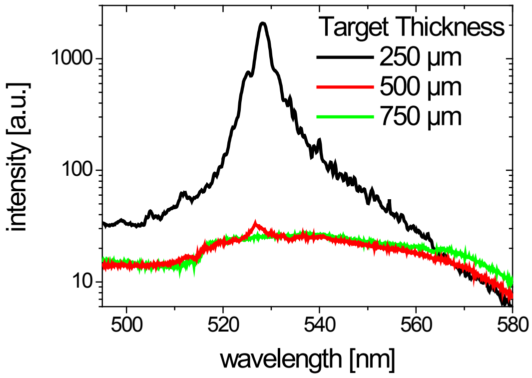

Fig. 6.18: *Spectra of the optical transition radiation emitted from targets with different thicknesses. The peak close to a wavelength of 527 nm for the 250 µm target indicates that the electrons are bunched either at the laser frequency ω_0 or at $2\omega_0$.*

Electron spectra obtained from two targets with different thicknesses and densities are shown in Fig. 6.19. The spectra are similar and can be well described by a two temperature Boltzmann distribution with T_1=2.6 MeV and T_2=8.8 MeV.

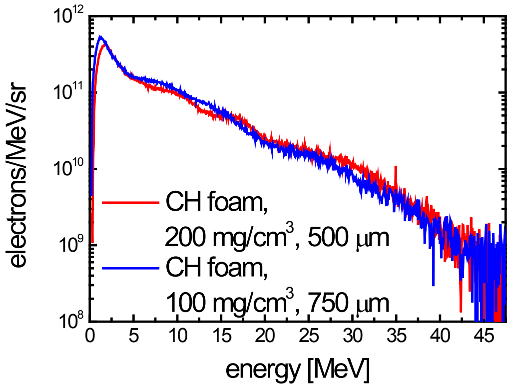

Fig. 6.19: *Electron spectra obtained from two targets with different thicknesses and densities.*

The CTR image shown in Fig. 6.17 clearly shows that the electron beam was split into a number of filaments during the transport in the foam plasma. As discussed in Chapter 4.6.3, this might be a consequence of the Weibel instability. For a confirmation of this assumption, 3D PIC simulations using the VLPL code were carried out. The first simulation investigated the generation of the relativistic electron beam at the target front surface. A Gaussian laser pulse with a normalized vector potential $a = a_0 \exp(-r^2/R^2)\exp(-t^2/T^2)\cos(\omega_0 t)$ was normally incident onto a 20 times overdense plasma. The focal spot radius, laser pulse duration, wavelength and amplitude were $R=63c/\omega_0$, $T=314\omega_0^{-1}$, $\lambda_0=2\pi c/\omega_0=1054$ nm and $a_0=15$, respectively. The preplasma was simulated using a linear density profile increasing from 0 to $20n_c$ over a distance of $300c/\lambda_0$. The calculated electron spectrum was fitted with a two temperature Boltzmann distribution, resulting in $T_1=8$ MeV and $T_2=3.5$ MeV. These values are reasonably close to the electron temperatures measured with the electron spectrometer in the experiment.

In the second part of the simulation, the transport of the electrons through the target was investigated. To this end, the electron beam with $\gamma=15$, a Gaussian density profile with a beam radius of $R_b=10\mu$m and a density of $n_b=0.1n_c$ in the center was injected in x-direction into a 30 times overdense plasma. The transversal beam profile and the magnetic fields were analyzed in detail. Fig. 6.20 (a) shows the transversal density profile of the electron beam in units of the critical density after a propagation distance of 100 µm. It is evident that the electron beam splits into a number of filaments. The spatial structure of the filaments is similar to the structure observed in the CTR images. The filaments are surrounded by a strong magnetic field shown in Fig. 6.20 (b).

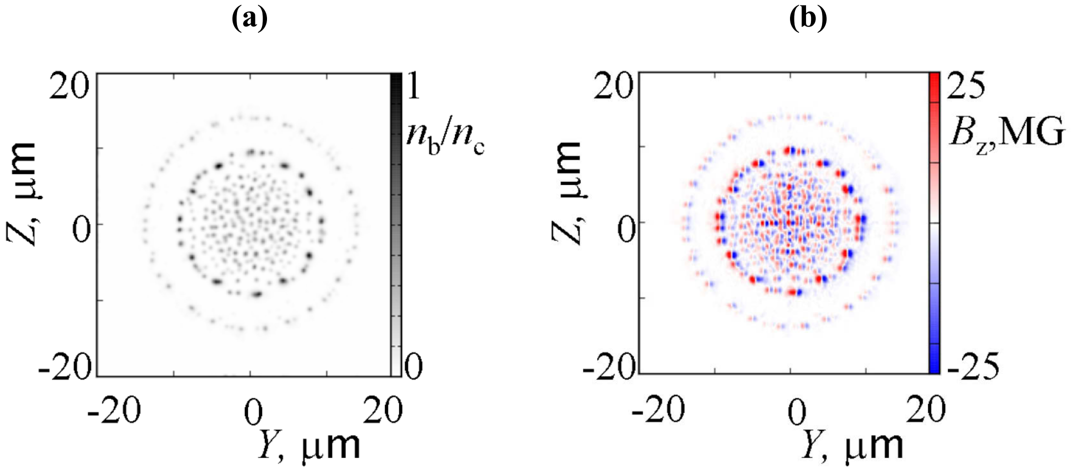

Fig. 6.20: *PIC simulation of the electron beam transport through a dense foam plasma. a) transversal electron density profile after a propagation length of 100 µm in the foam plasma. b) z-component of the magnetic field strength. The electron beam splits into a number of filaments due to the Weibel instability. The filaments are surrounded by strong magnetic fields.*

In the simulations the electron beam transports a power of $P_b = \gamma n_b mc^3 \pi R_b^2 \approx 14\,\mathrm{TW}$, corresponding to a current of $I = n_b ec\pi R_b^2 \approx 1.8\,\mathrm{MA}$. This value exceeds the Alfvén current by a factor of 7. The current in each filament in Fig. 6.20 is below than the Alfvén current.

For the interpretation of the CTR spectra, the 1D ballistic transport model introduced in Chapter 4.6.2 was used. Because the observed spectra are consistent with electron bunching frequencies of $1\omega_0$ and $2\omega_0$, both cases were considered in the calculations. Similar to the analysis in Chapter 6.1.2, it is assumed that bunching at $1\omega_0$ corresponds to a population of electrons heated by resonance absorption, whereas bunching at $2\omega_0$ corresponds to a population of electrons generated by $\boldsymbol{j} \times \boldsymbol{B}$ heating. For resonance absorption, a total number of Λ_{res}=213 identical electron bunches, corresponding to the 750 fs pulse duration and one electron bunch per laser cycle, was used. Because the electrons accelerated by resonance absorption propagate predominantly along the target normal, the propagation lengths are 250, 500 and 750 µm corresponding to the thicknesses of the foam targets. For $\boldsymbol{j}$ x $\boldsymbol{B}$ heating, a total number of Λ_{jxB}=426 electron bunches was used, corresponding to two electron bunches per laser cycle. The electrons in this population are expected to be accelerated in a direction close to the laser axis, and the corresponding propagation lengths are larger than the target thicknesses by a factor of $\sqrt{2}$. The calculated CTR fluences at the wavelength of $2\omega_0$ are shown as a function of the electron temperature in Fig. 6.21 for the three target thicknesses used in the experiment. In the calculation, the same number of electrons in each bunch was assumed. As expected, the CTR fluences increase with temperature (see Chapter 4.6.2).

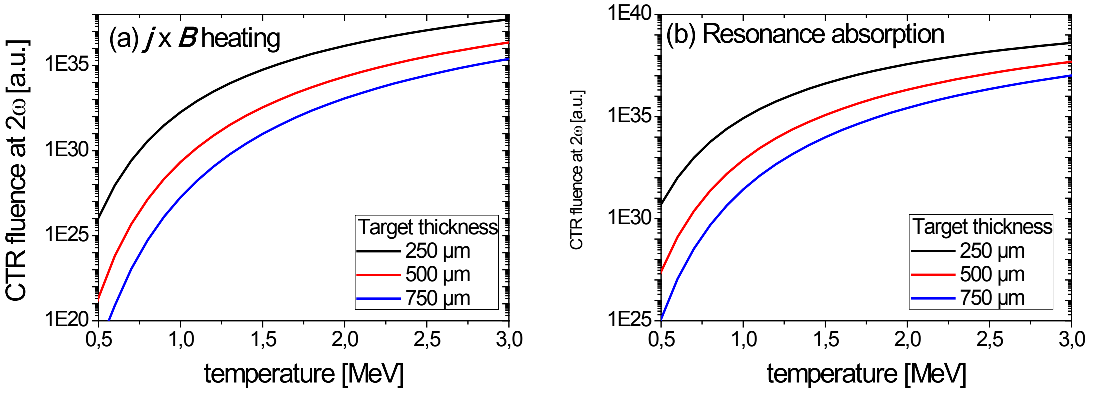

Fig. 6.21: *Calculation of the CTR fluences at the second harmonic of the laser with a 1D ballistic transport model for **j** × **B** heating (a) and resonance absorption (b).*

The ratios of calculated CTR fluences at $2\omega_0$ of the 500 µm to 250 µm targets are plotted in Fig. 6.22. The measured ratio of the CTR fluences of CTR$_{500}$/CTR$_{250}$=0.01 and an experimental error of 20% are indicated by the solid and dotted lines, respectively. This value corresponds to a temperature of T_{res}=1±0.2 MeV for the case of resonance absorption and T_{jxB}=1.7±0.2 MeV for the case of $\boldsymbol{j} \times \boldsymbol{B}$ heating.

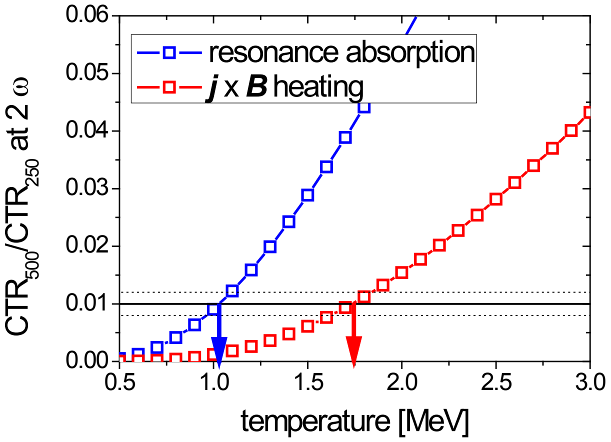

Fig. 6.22: *Ratios of the CTR fluences from the 500 µm to the 250 µm targets for resonance absorption and **j** × **B** heating as a function of electron temperature. The measured value of 0.01 is represented by the solid black line. The dotted black lines indicate the experimental error of 20%.*

These temperatures are compared to the scaling laws of hot electron temperatures given by Equations (4.36) and (4.37) in Chapter 4.5. At a laser intensity of 5×10^{20} W/cm^2, the scaling law by Beg predicts a temperature of 1.8 MeV for resonance absorption, whereas the scaling law by Wilks results in a temperature of 9.8 MeV for $\boldsymbol{j} \times \boldsymbol{B}$ heating.

For both cases, the temperature obtained from the CTR spectra is significantly smaller than the temperatures calculated with the scaling laws and measured with the electron spectrometer. There are a number of factors which can explain these observations. Due to the filamentation of the electron beam, the assumption of ballistic transport might not be valid in this experiment. It is expected that the formation of the filaments and the interaction of the electrons with the strong magnetic fields leads to more complex electron trajectories. In addition, it has to be taken into account that the Alfvén limit and target charge up effects will inhibit the propagation of a fraction of the electrons from the target to the electron spectrometer. Analytical models predict that basically the low energetic electrons will be confined to the target [76, 77]. As a consequence, the energy distribution of the electrons generating the CTR at the target surface will differ from the energy distribution of the electrons measured with the electron spectrometer at large distances from the target.

6.3 Electron transport in cone targets

For some applications, such as the fast ignitor scheme in ICF, enhanced backlighters and isochoric heating with fast electrons, a high flux of electrons is important for the performance. The high value of the divergence of the electron beams generated in laser irradiated, planar targets of up to 50° measured in some experiments [96] is a limiting factor. Cone guiding has been demonstrated to be a promising approach to achieve high electron fluxes. Besides guiding of electrons to the tip of the cone, their transport along a thin wire attached to the tip has been demonstrated [133]. The high energy density at the tip of the cone also results in a higher conversion efficiency to protons by target normal sheath acceleration [78].

There are two effects contributing to the strong electron fluxes at the tip of the conical targets. On the one hand, the laser is reflected by the overdense plasma at the inner cone surfaces, resulting in an increased intensity at the tip of the cone. On the other hand, electric and magnetic fields in the cone guide the electrons to the tip as shown in Fig. 6.23. The electric field normal to the surface is generated by the Debye sheath at the inner surface of the cone. The magnetic fields parallel to the surface are generated by currents in the cone. In these fields, electrons are inhibited from being injected into the bulk target material and are transported to the tip of the cone.

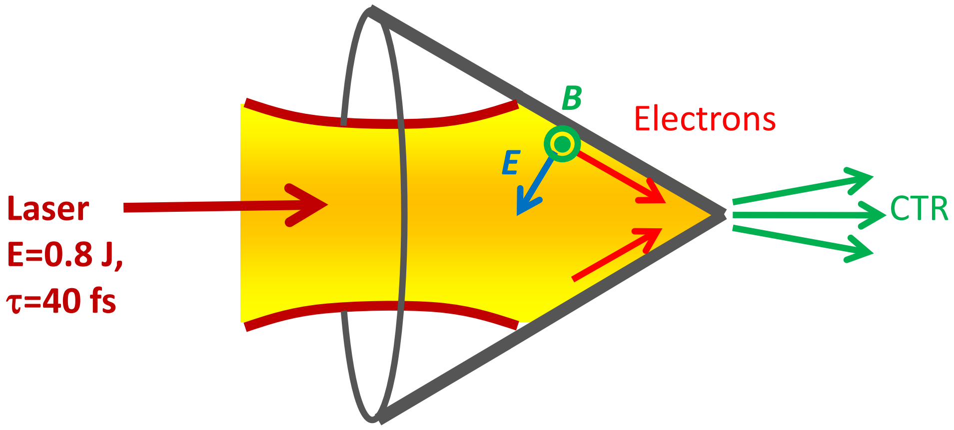

Fig. 6.23: *Guiding of electrons to the tip of a cone target. The electric field in the Debye sheath and the self-generated magnetic field result in a potential minimum close to the inner cone surface. In this potential, electrons are transported to the tip of the cone. When the electrons are emitted from the tip of the cone, CTR is produced.*

In this chapter, the generation and transport of electron beams in cone targets is studied in detail. To this end, the CTR emitted by the fast electrons at the tip of the cones was investigated. A reproducible method for a precise alignment of the cones was developed [85]. The focussing geometry was optimized for an efficient production of hot electrons. The transport of fast electrons in the extended tip of the cones was observed. These results are confirmed by PIC simulations [84].

For the experiments, different types of cone targets were investigated. Scanning electron microscope images of copper cones are shown in Fig. 6.24. The base of the cones was 250 µm in diameter, the height was 250 µm. The cones in Fig. 6.24 have a rough surface with bumps in the order of 15-20 µm. In addition, cones with a smooth surface with a flatness of less than 4 µm and cone targets with an extended tip as shown in Fig. 6.30 were used.

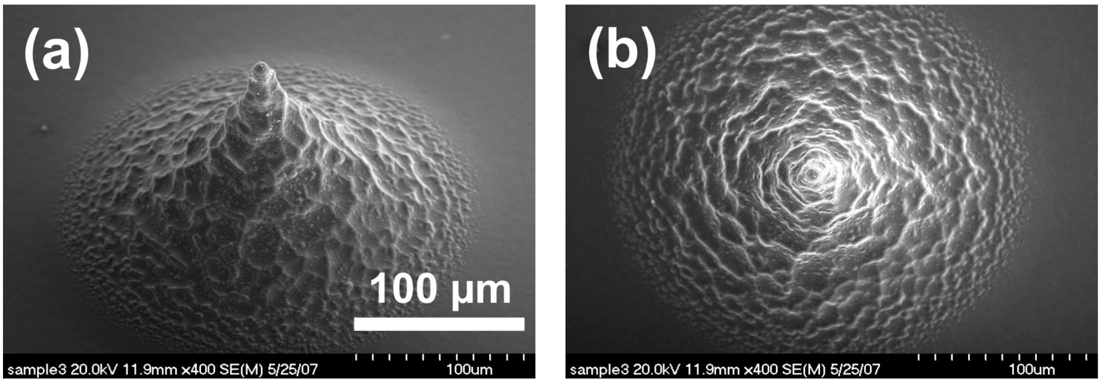

Fig. 6.24: *Scanning electron microscope images of the copper cone targets for cone guiding experiments with ultrashort laser pulses. (a): slanted view, (b): top view.*

The experiments were carried out at THOR laser using the same setup as shown in Fig. 6.1. For the precise alignment of the cone targets, a retro diagnostics and several telescopes viewing at the target at different angles (not shown in Fig. 6.1) were used. The cones were attached together with 10 µm copper foils to a motorized xyz target mount. The coordinate axes are chosen as indicated in Fig. 6.25. In a first series of shots, the CTR signal and the x-ray yield from the copper foils were maximized by scanning the z-position of the targets. The position of the best interaction was defined as z=0 (Fig. 6.25 a). The cone targets were then aligned in two steps. In the first step, the z-position of the base of the cones was aligned to z=0 using the retro diagnostics and a telescope viewing obliquely at the target front side. In the second step, the tip of the cone was aligned to the laser axis. Therefore, the ASE from the laser which was backscattered by the target was observed with the retro diagnostics. When the tip of the cone was on the laser axis, a strong signal was observed which was extremely sensitive to the exact x-y position of the cone. This observation is explained in Fig. 6.25. When the cone is off axis as shown in Fig. 6.25 (b), the light gets reflected sideways and is not collected by the imaging optics. In Fig. 6.25 (c), the cone is on axis, the light is reflected symmetrically and fills a wide area of the image plane. Indeed, at a well defined x-y-position, a bright signal filling the whole image plane of the retro diagnostic could be identified for each cone. The accuracy of the lateral alignment was about 1-2 µm.

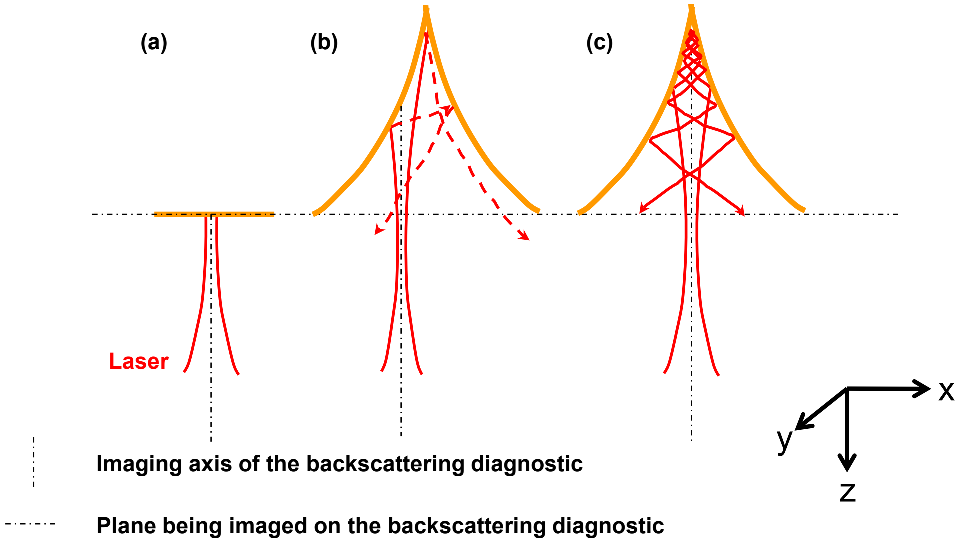

Fig. 6.25: *Alignment of the cone targets. When the cone is on axis with the laser beam, there is a strong back reflection allowing for a precise lateral alignment of the cones targets.*

A typical image of the optical emission from the tip of the cone is shown in Fig. 6.26. A bright spot with a FWHM diameter of about 5 µm is observed. Similar to the experiments with the foil targets at an angle of incidence of 10° (see Chapter 6.1.1), the spectra of the optical emission from the cone targets were peaked at 800 nm. Following the interpretation in the previous chapters, this indicates that the observed signal is CTR generated by electrons bunched at the laser frequency at the tip of the cone.

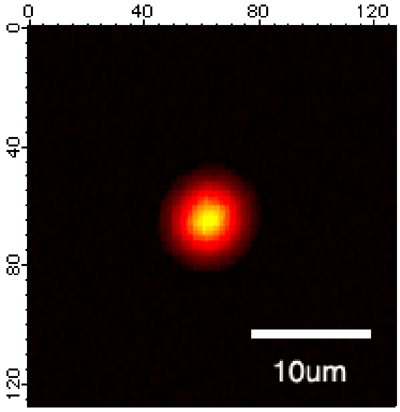

Fig. 6.26: *Image of the optical emission from the tip of the cone. The units at the axes are pixel numbers.*

In order to optimize the electron flux at the tip of the cone, a series of shots measuring the CTR fluencies at different z-positions was carried out. The result is shown in Fig. 6.27. The highest CTR fluences were obtained at z=0, corresponding to the configuration where the laser focus is at the base of the cone. Weaker CTR fluences were observed when the cone tip was moved 50 µm towards the laser focus. The CTR disappeared for z-positions larger than 150 µm, corresponding to a distance between the focus and the tip of less than 100 µm.

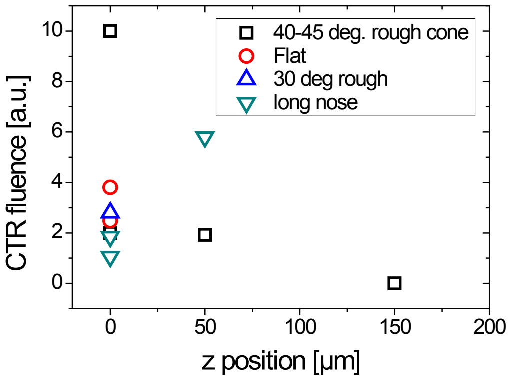

Fig. 6.27: *CTR fluences emitted from the cone targets for different z-positions. The highest signal is obtained when the focus is at the base of the cone. This observation is attributed to optical guiding of the laser pulse in conjunction with the mitigation of the preplasma inside the cone.*

For the interpretation of this observation, it is important to mention that, for z=0, the divergence of the laser beam leads to a decrease of the laser intensity when it impinges onto the inner cone surface as shown in Fig. 6.28. In the interaction zone, the beam diameter is 21 µm, corresponding to an intensity of 2×10^{18} W/cm^2. It is assumed that the strong electron fluence observed in this configuration is related to the mitigation of preplasma formation at the tip of the cone [85]. The smaller laser intensity at the inner cone surface leads to a smaller preplasma scale length, resulting in a more efficient optical guiding of the laser pulse and guiding of the electrons along the cone surface. This interpretation is consistent with [15] where electron guiding by the cone was inhibited in the presence of a preplasma.

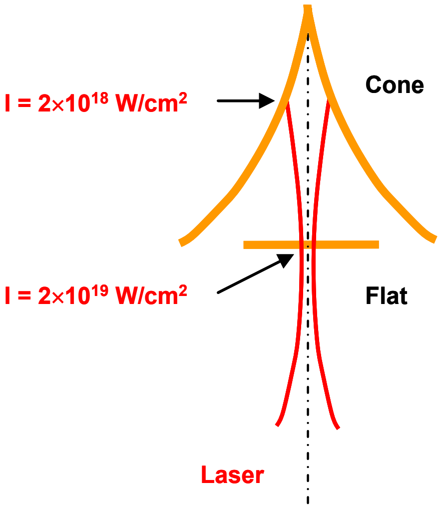

Fig. 6.28: *Alignment of the cone targets. The highest CTR fluence was observed at z=0 when the laser Divergence of the laser beam at z=0µm when the focus close to the base of the cone. In this configuration, the beam diameter is approximately 21 µm when the laser pulse is incident onto the cone surface and the intensity in the interaction zone is about one order of magnitude smaller compared to a flat target at best focus.*

In order to further characterize the electron transport inside the target, the size of the CTR spot was measured using lineouts in x and y direction through the central region of the images. The result is shown in Fig. 6.29. The diameter of the CTR images obtained from the flat foils with a thickness of 10 µm is between 6 and 9 µm. Similar values were found for the cone with 45° opening angle. A remarkable result is that significantly smaller values for the CTR spot diameters were found for the cones with the extended tips.

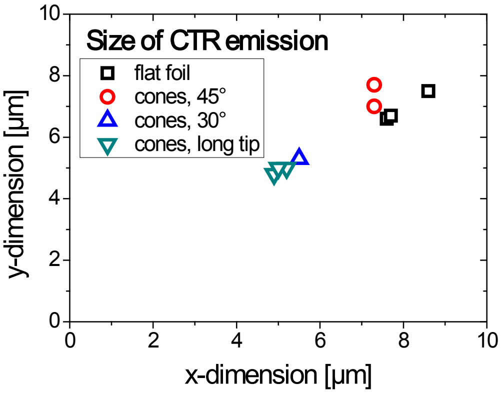

Fig. 6.29: *Size of the CTR emission from flat foils and different types of cone targets. The smallest diameter is observed for the cones with an extended tip.*

To explain the small diameter of the CTR signal obtained from the long tip cones, the exact shape of the inner cone surface close to the tip was analyzed. Scanning electron microscope images of the region close to the tip are shown in Fig. 6.30. In the top view (a) and the side view (b), the white arrows indicate the outer diameter of the extended tip of 15-20 µm. Fig. (c) shows the inner surface of the cone close to the tip, whereas (d) is a magnification showing a small channel with a diameter of 5 µm extending into the tip. The dotted lines in Fig. 6.30 (a) and (c) indicate the size of the laser beam in the cone where it impinges onto the inner surface when the focus is at *z*=0. In the side view (b), the inner surface of the cone is indicated by the dotted line.

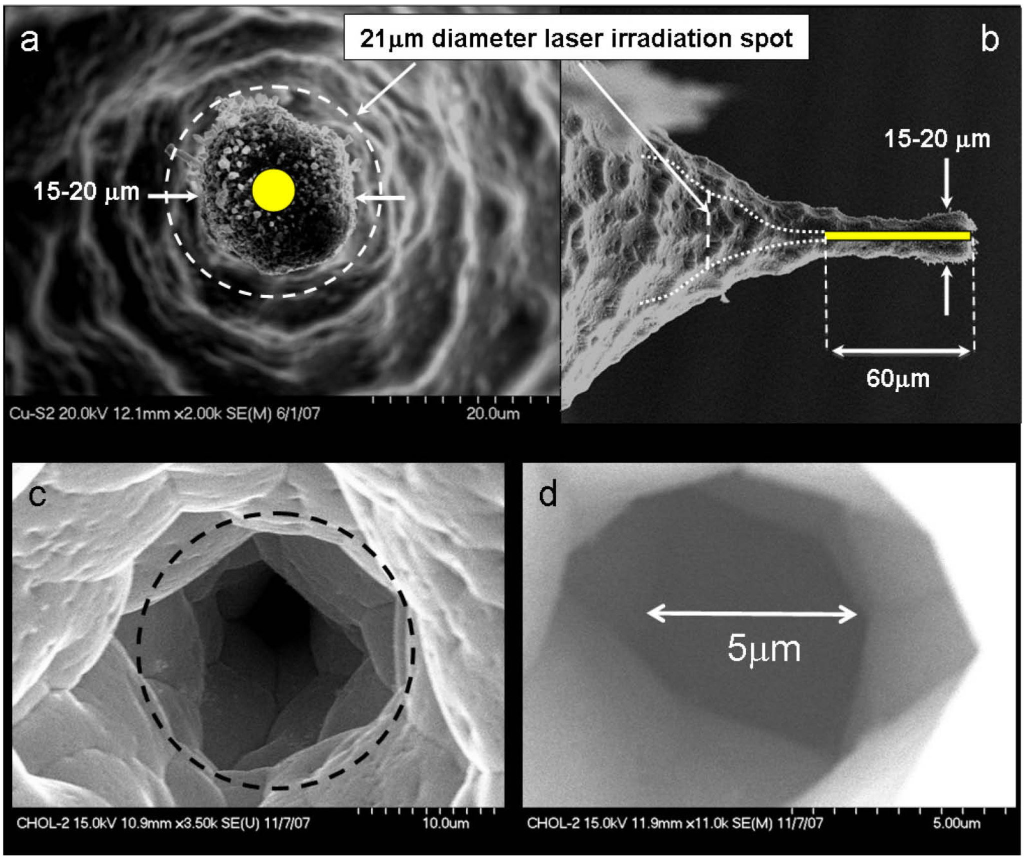

Fig. 6.30: *Scanning electron microscope images of the copper cones with an extended tip. (a) top view, (b) side view, (c) and (d) view inside the cone. The yellow spot in (a) and the bar in (b) indicate the electron beam transported through the extended tip. The dashes lines in (a) and (c) indicate the diameter of the laser beam when it impinges onto the cone surface.*

In order to further analyze the experimental results, two dimensional PIC simulations using the PICLS code [206] were carried out. In the simulations, a Gaussian laser pulse with 1 µm wavelength and 40 fs duration is used. Similar to the experimental setup in Fig. 6.28, the pulse is incident onto the cone at an intensity of 3×10^{18} W/cm^2

with a spot size of 21 µm. The laser is polarized in the simulation plane, corresponding to p-polarization with respect to the inner cone surface. The shape of the target in the simulations is close to the shape of the cone in Fig. 6.30. The walls of the cone consist of 10 µm of fully ionized aluminium at 10 times critical density. A channel with 5 µm diameter extends into the tip of the cone. The dimension of the simulation box is 150 µm × 150 µm with a mesh size of 80 nm × 80 nm. The laser enters the simulation box from the left side and the peak of the pulse crosses the simulation box boundary at t=40fs.

The electron temperatures calculated with the PIC simulations at three different times (132 fs, 264 fs and 396 fs after the beginning of the simulation) are shown in Fig. 6.31. In the simulations, the laser pulse is guided to the tip of the cone where the intensity increases from 3×10^{18} W/cm^2 almost by one order of magnitude to 2.2×10^{19} W/cm^2. At the tip, a high density plasma is produced filling the funnel. In Fig. 6.31 (b), a population of hot electrons is generated at the tip of the cone in a region with a diameter of 5 µm corresponding to the inner diameter of the channel. This size is much smaller than the initial laser focus diameter of 21 µm. In Fig. 6.31 (c), the hot electron population extends over a distance of several 10 microns inside the tip. The electron beam diameter remains well collimated over this distance.

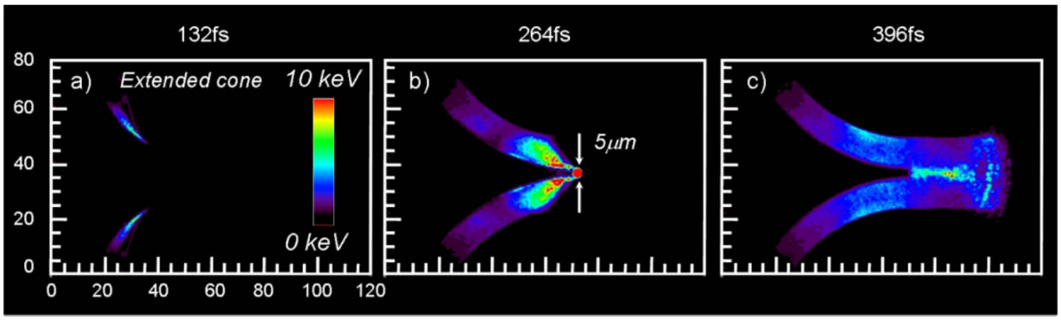

Fig. 6.31: *PIC simulation of electron acceleration and transport in a cone target at three different points of time. At t=132 fs, the laser is incident onto the inner cone surface. At t=264 fs, population of fast electrons is generated at the tip of the cone. At t=396 fs, The electron beam with a diameter of 5 µm extends into the tip of the cone.*

The relation between the electron beam diameter and the dimension of the channel in the cone tip was further investigated in a second set of PIC simulations. Fig. 6.32 shows the energy density for inside tip diameters of a) 2 µm, b) 5 µm and c) 10 µm at *t*=264 fs. In each simulation, a population of hot electrons is observed at the tip of the cones. The transversal dimensions of the high energy density regions are close to the channel diameters of 2, 5 and 10 µm, respectively.

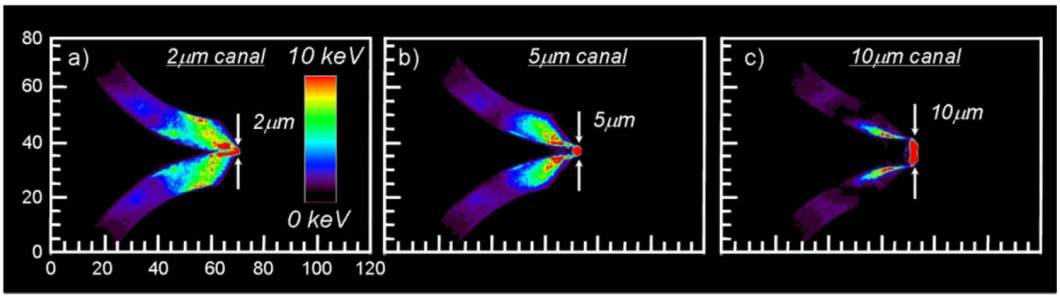

Fig. 6.32: *PIC simulations of the electron acceleration and transport in cone targets with different inside tip diameters at t=264 fs. In each simulation, the dimension of the electron beam diameter is close to the diameter of the channel at the tip.*

The experimental data in combination with the PIC simulations allow for the following conclusions: A beam of hot electrons with a diameter in the order of channel diameter is emitted from the tip of the cone. In the cones with the extended tip, the electron beam is transported over distances in the order of several 10 µm. These results demonstrate the potential of the new cone targets for applications in ICF, advanced x-ray sources, measurement of radiative properties and EOS measurements of dense plasmas.

6.4 Electron transport in wedge and pyramid targets

In the previous chapter, cone guiding is explained by optical guiding of the laser pulse in conjunction with guiding of electrons by the Debye sheath and the self-generated magnetic fields at the inner cone surface. Computer simulations have shown that the magnetic fields are predominantly generated in the polarization plane of the laser [207]. In order to investigate the effect of the laser polarization in more detail, additional experiments using re-entrant wedge and pyramid targets were carried out. As shown in Fig. 6.33, the polarization with respect to the inner surface is well defined for the wedge and pyramid shaped targets.

The targets were produced from (100) single crystal silicon wavers using standard lithographic KOH etching techniques. Owing to the dependence of the etching rate from the crystallographic orientation, pyramid and wedge shaped structures can be produced. A schematic drawing (side view) of the target is shown in Fig. 6.33 (a). Fig. 6.33 (b) and (c) show scanning electron microscope images (top view) of a pyramid and wedge target, respectively. The opening angle of 71° of these structures is determined by the angle of 54.5° between the (100) and (111) orientation in silicon. The rear side of the targets was coated with a 1 µm aluminium layer to inhibit the transmission of laser light.

The experiments were carried out at THOR laser using the experimental setup in Fig. 6.1. The targets were mounted on a motorized xyz translation stage. The laser was incident onto the targets as indicated in Fig. 6.33 (a).

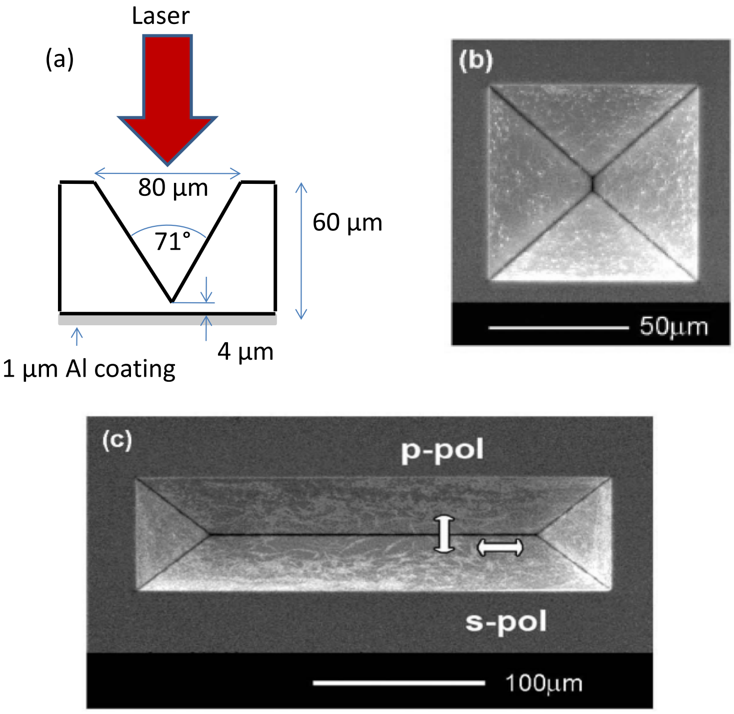

Fig. 6.33: *Pyramid and wedge shaped targets of the investigation of polarization effects. The targets were produced by anisotropic etching of silicon. a) Schematic drawing (side view) of the pyramid target. The opening angle of 71° is determined by the crystallographic structure. b) and c) Scanning electron microscope images (top view) of pyramid and wedge shaped targets. The two different laser polarizations (s and p) in the experiment are indicated by the arrows in (c)*

The CTR images obtained from the wedge targets in p- and s-polarization, and from the pyramid targets are shown in Fig. 6.34. The images are significantly different from those obtained from planar targets shown in Fig. 6.2.

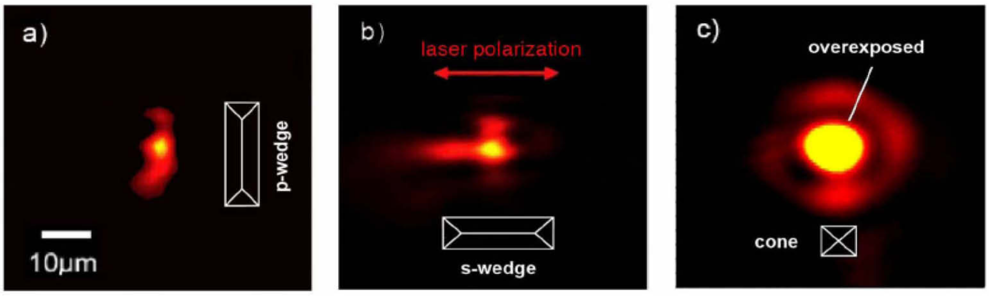

Fig. 6.34: *Images of the CTR from (a) p-wedges, (b) s-wedges and (c) pyramid targets. The polarization of the laser is indicated by the red arrows. The central region in (c) is overexposed in order to emphasize the side-lobes.*

The spectra of the CTR obtained from the structured targets were peaked at 800 nm, similar to the CTR emission observed for planar foils at an angle of incidence of 10° in Chapter 6.1.1. The emission at 400 nm was very low and could hardly be separated from the broadband thermal plasma emission. This observation indicates that the electrons generating the CTR emission were bunched at the laser frequency. The CTR images consist of a bright region close to the tip and a weaker contribution in the direction normal to the target walls. In addition, the emission close to the tip is elongated along the crease of the wedge targets. The shape of the CTR emission suggests that two populations of electrons were generated. One population is emitted from the region close to the tip whereas the other one propagates normal to the pyramid and wedge walls. It is noted that the stronger CTR fluence close to the tip is, at least partially, a result of the shorter propagation length of the electrons from the tip to the target rear side.

For the p-polarized wedge, the signal emitted normal to the wedge surfaces is very weak compared to the case of s-polarization. This observation can be explained assuming that there is indeed an effect of the polarization on the generation of magnetic fields at the inner cone surface. A strong magnetic field in the p-wedge will inhibit electrons from penetrating into the bulk target and force them back to the surface and to the tip of the cone. The weaker field in the case of the s-wedges cannot confine the electrons to the wedge surface, and they can penetrate into the target material. This qualitative interpretation of the CTR data is in agreement with the simulations in [207].

7 Summary and conclusions

The physics of dense plasmas is an important field of research with relevance to applied and fundamental science. In the recent years, new laboratory experiments have strongly contributed to our understanding of dense plasmas. Many of these experiments have become possible due to the rapid development of laser technology. In this work, important novel aspects of the physics of dense plasmas with relevance to astrophysics, fusion research, x-ray science and atomic physics are presented. Two major topics are investigated. In the first part of this work, dense plasmas are produced by isochoric heating of solid density matter for spectroscopic studies and equation of state measurements. In the second part, the generation and transport of strong currents in dense plasmas are investigated.

7.1 Generation of dense plasmas

In high density plasmas, the interaction between particles becomes increasingly important and significantly affects the properties of the plasma. This is in particular the case for the radiative properties and for the equation of state of dense plasmas. The theoretical treatment of high density phenomena is complex, and reliable predictions are only possible when numerical calculations can be compared to experimental data. Consequently, there is an enormous interest in laboratory experiments investigating opacities and equations of state in laboratory experiments. However, the experience from the recent years has shown that the preparation of well defined samples of dense plasmas is complex.

In the first major part of this work, the production of dense plasmas by isochoric heating of solid density matter is investigated. Two approaches allowing for the generation of dense plasmas in different parameter regimes for spectroscopic studies and for equation of state measurements are presented. The first approach is based on direct irradiation of solids with high contrast, few-cycle laser pulses. Due to the high contrast in combination with the short pulse duration, extremely small values of the preplasma scale length below the electron skin depth were achieved. Dense plasma layers with an initial thickness of about 10 nm and peak temperatures of about 200 eV were produced.

In the XUV spectra obtained from elements with a small atomic number (boron, carbon and nitrogen), a series limit is observed which is explained by pressure ionization in the dense plasma. In addition, spectroscopic studies of the *L* shell emission of higher *Z* elements such as titanium under conditions found in the interior of stars are demonstrated. Detailed computer simulations including the atomic kinetics, the expansion of the plasma and radiative transport are in good agreement with the measurements. In the simulations, the plasma is in a highly transient state immediately after the interaction, but the plasma approaches the LTE conditions quickly on a time scale in the order of 100 fs. Due to the small plasma layer thickness, the plasma cools down quickly. The calculations predict extremely small durations of the Ly_α and He_α emission of the order of a picosecond. In the computer simulations, the ion-ion coupling parameter is close to 1 for boron nitride and carbon plasmas, and significantly larger than 1 for titanium plasmas in the time interval of 10 ps after the laser peak.

The small preplasma scale length makes the few-cycle laser pulse extremely interesting for fundamental studies of the interaction of dense matter with strong electromagnetic fields. The absorption of laser energy in solid targets under these conditions is not yet fully understood and is subject of topical research. In this work, absorption measurements are presented over a wide range of laser intensities and incidence angles for different polarizations. In all measurements, the absorption at p-polarization is stronger than at s-polarization. A threshold behaviour for p-polarization with a strong increase of the absorption at intensities exceeding 10^{14} W/cm^2 is found. The highest values of the absorption close to 80% are observed for p-polarization close to grazing incidence. These experimental results are in agreement with PIC simulations, indicating that the absorption mechanism is of collisionless nature.

Due to the short penetration depth of the laser into the solid target, the thickness of the dense plasma layer produced with the sub-10-fs pulses is limited to 10 nm. The preparation of thicker samples by isochoric heating requires radiation with a higher penetration depth [166]. Therefore, a second method for the generation of dense plasmas was pursued. Short pulses of protons with MeV energies were generated in laser irradiated metal foils by target normal sheath acceleration. Solid aluminium targets with a thickness of 2 µm were isochorically heated to a temperature of 20 eV by the laser-driven proton beam. The expansion and the temperature of the plasma are measured with high time resolution. The EOS along the release isentrope was investigated by comparing the experimental data with computer simulations. A good agreement with an error of less than 20% was obtained for the SESAME table 3718. The calculations predict an ion-ion coupling parameter of $\Gamma_{ii}\approx100$ at the center of the foil.

7.2 Electron transport in dense plasmas

In the second major part of this work, the generation and the transport of strong currents in dense plasmas is investigated. Strong currents are driven when solids are irradiated with ultrashort laser pulses at relativistic intensities. The transport of these currents in dense plasmas plays an important role, e.g., for ultrafast x-ray sources, for the fast ignitor scheme and for proton and ion acceleration by target normal sheath acceleration. The optimization of the conversion efficiency into hot electrons and a controlled transport of the electrons are important issues for the performance of these applications.

Although many experiments have investigated the generation and the transport of electron beams in laser irradiated, solid targets and important scaling laws were found, there is still no comprehensive picture. The acceleration processes and the transport depend on a large number of experimental parameters such as preplasma scale length, plasma temperature, conductivity, laser intensity, pulse duration and polarization. Magnetic fields and instabilities affect the transport of currents in a complex way.

Here, the generation and the transport of strong currents were investigated over a wide range of laser parameters. Special attention was given to the extreme cases of very short laser pulses with durations of only 40 fs and very intense laser pulses with a power in the petawatt regime.

The production of strong currents with 40 fs laser pulses incident onto planar, solid targets was investigated for laser intensities up to 2×10^{19} W/cm^2. Electron beams with temperatures in the MeV range were generated. The transport of the electron beams through the target was investigated with high spatial resolution by observing the coherent transition radiation (CTR) emitted from the target. Depending on the angle of incidence θ, different acceleration mechanisms were identified.

At θ=10°, resonance absorption was the dominant heating mechanism. Measurements of the CTR fluence and the bremsstrahlung generated by the electrons inside the target yield an electron temperature was about 300 keV. The divergence of the electron beam of 8° was very small, indicating that self-generated magnetic fields contribute to a collimation of the electron beam in the target.

At θ=45°, two distinct electron beams were emitted from the target rear side. One beam close to the target normal was generated by resonance absorption, whereas the second beam close to the laser direction was generated by $\boldsymbol{j}\times\boldsymbol{B}$ heating. This interpretation is confirmed by 3D PIC simulations. The number of electrons heated by resonance absorption exceeds the number of electrons produced by $\boldsymbol{j}\times\boldsymbol{B}$ heating by a factor of 5. The temperatures of the beams measured in the experiment are 0.78 MeV for resonance absorption and 1.5 MeV for $\boldsymbol{j}\times\boldsymbol{B}$ heating. These electron temperatures are close to published scaling laws obtained with longer laser pulses.

From these results, the currents transported by the electron beams can be estimated. Assuming a conversion efficiency of 20% from laser energy into fast electrons, currents in the Megaampere range are obtained. These currents are significantly above the Alfvén limit, indicating that cold return currents play an important role for the beam transport in dense plasmas.

In the FI scheme, the generation of strong currents with laser powers in the petawatt regime is proposed. Here, the transport of electron beams produced by petawatt laser pulses incident onto CH foam targets at 15 to 30 times overcritical densities was studied over long distances up to 750 µm. For this purpose, the CTR emitted by the electrons from the target rear surface was imaged with high resolution. In the experiments, the filamentation of the electron beams due to the Weibel instability was observed. The experimental observations are in agreement with PIC simulations, indicating that strong currents of about 1.8 MA are driven. A lose analysis of the spectra of the optical transition radiation suggests that the transport of the electrons is not purely ballistic. The strong decrease of the CTR fluence for the thick targets might be related to the filamentation and the interaction of the electron beam with quasistatic electric and magnetic fields during their transport.

For some applications, the transport of high electron fluxes is crucial for the performance. The capability of cone guiding for the generation of high electron fluxes was demonstrated in a number of studies in the past [78, 133]. Here, a systematic study of cone guiding for different experimental parameters is presented. Copper cones with different opening angles were used for the experiments. A method for the precise alignment of the targets was developed. Using this method, the effect of the laser focussing geometry on the electron transport was studied in detail, and the yield of hot electrons at the tip of the cones was optimized. Interesting results were obtained from cone targets with an extended tip. The transport of the electrons in the extended tip over distances of 60 µm was observed. The results are in agreement with PIC simulations.

For a more detailed understanding of the role of polarization effects and the magnetic fields involved in cone guiding, additional experiments were carried out. In these experiments, cones with a rectangular base (pyramid shaped targets) and wedge shaped targets were used. In these targets, the laser is either p- or s-polarized with respect to the inner surfaces.

The electron transport was significantly different from planar foil targets. CTR images obtained from the rear side suggest that guiding of the electrons along the inner surface is more efficient for the case of p-polarization. This observation is in agreement with [207], where the magnetic fields are predominantly generated in the plane of p-polarization.

8 Outlook

The physics of dense plasmas is a contemporary field of research and involves different areas of fundamental and applied science [164]. Future developments in the fields of laser technology, target engineering and plasma diagnostics will render possible new experiments for a deeper understanding of high energy density matter.

Laser systems are continuously being optimized in terms of contrast, pulse duration and power. Lasers generating pulses shorter than 10 fs at relativistic intensities are currently being developed. Techniques for the optimizations of the contrast, such as plasma mirrors and cross polarized wave generation (XPW) are available. These laser systems are promising tools for isochoric heating by direct laser irradiation or by laser driven electron beams in mass limited targets.

The experiment on isochoric heating with proton beams presented in this work demonstrates the potential of laser driven particle beams for the generation of dense plasmas. At the present time, there is a strong effort to optimize these beams for applications in fundamental and applied science. The generation of proton and ion beams with mono-energetic features has been demonstrated [101, 203, 231]. Techniques for focussing of laser driven particle beams using plasma devices [237] or magnetic quadrupole lenses [64] were developed. Using these optimized beams, the preparation of WDM states over a wider range in density-temperature space will be possible.

The experiments in this work also highlight the potential of an advanced target design to control important parameters of laser-plasma interaction. The generation of high fluxes of electrons in cone targets and the transport of electrons along thin wires are important examples [84, 133]. Other interesting target designs are currently being developed. Targets with regions of different resistivity were suggested for a collimated transport of relativistic electrons in dense plasmas [185]. The high energy density achieved in mass limited targets renders possible experiments on isochoric heating with laser driven electrons [2, 126, 158, 235]. The consequent implementation of an advanced target design in combination with optimized laser systems offers a high potential for novel experiments investigating the physics of dense plasmas.

Improved diagnostics will provide a direct view into the microscopic properties of dense plasmas. In the past years, new experiments investigating Thomson scattering of x-rays from dense plasmas were developed [93, 97, 106, 141, 184, 245]. Recently, measurements of the dynamic structure factor [196] and plasmons [94] in warm dense plasmas were demonstrated. In these experiments, x-rays were generated from laser irradiated foils. It is expected that substantial improvements will be possible using ultrabright x-rays produced by 4th generation light sources [146] (see below).

These new diagnostics allow for a direct comparison between experimental data and theoretical predictions. In Reference [196] it was demonstrated that a good agreement with the measured dynamic structure factor could be obtained in *ab initio* simulations using density functional theory (DFT) for the electrons and molecular dynamics (MD) for the ions [136–138].

Besides these improvements, it is expected that the research on dense plasmas will strongly benefit from the development of the new generations of heavy ion accelerators and x-ray free electron lasers (XFELs). A number of experiments have demonstrated the potential of heavy ion beams for the generation of high energy density matter. For existing heavy ion synchrotrons such as the SIS18 at GSI in Darmstadt, dense plasmas with a temperature of the order of 1 eV were produced [57, 104]. The new SIS100 synchrotron which is currently constructed at GSI within the Facility for Antiproton and Ion Research (FAIR) will provide heavy ion beams with a number of 2×10^{12} ions/bunch, an energy of up to 2.7 GeV/u at a bunch duration of 20-100 ns [70, 223]. A large number of design studies have demonstrated the potential of such intense heavy ion beams for the production of bulk samples of WDM over a wide range of parameters by isochoric heating of solid density matter [71, 104, 110, 223, 228, 229].

The production of warm, dense plasmas with temperatures of up to 40 eV by heating solid aluminium with XUV radiation from a free electron laser has recently been demonstrated at the FLASH facility at DESY [249]. Two XFELs, the XFEL at the

TESLA facility at DESY, Hamburg [234] and the Linac Coherent Light Source (LCLS) at Stanford Linear Accelerator [148], are currently being constructed. These XFELs will generate coherent x-ray pulses with tuneable energies up to the keV range, pulse durations on a femtosecond scale and an unprecedented brightness. These light sources will allow for volumetric heating of solid matter and for the development of new diagnostics such as x-rays scattering and pump-probe experiments investigating the atomic kinetics in dense plasmas [146].

The physics of dense plasmas is a rapidly evolving field of research with an increasing community of scientists worldwide. The close cooperation between different research facilities will open new horizons for a deeper understanding of dense plasmas and matter under extreme conditions in the future.

List of figures

Bibliography

1. P. Agostini, F. Fabre, G. Mainfray, G. Petite, and N.K. Rahman, *Free-Free Transitions Following Six-Photon Ionization of Xenon Atoms,* Phys. Rev. Lett. **42**, 1127-1130 (1979).

2. K.U. Akli, M.H. Key, H.K. Chung, S.B. Hansen, R.R. Freeman, M.H. Chen, G. Gregori, S. Hatchett, D. Hey, N. Izumi, J. King, J. Kuba, P. Norreys, A.J. Mackinnon, C.D. Murphy, R. Snavely, R.B. Stephens, C. Stoeckel, W. Theobald, and B. Zhang, *Temperature sensitivity of Cu* K_α *imaging efficiency using a spherical Bragg reflecting crystal,* Phys. Plasmas **14**, 23102 (2007).

3. H. Alfven, *On the Motion of Cosmic Rays in Interstellar Space,* Phys. Rev. **55**, 425 (1939).

4. M.V. Ammosov, N.B. Delone, and V.P. Krainov, *Tunnel Ionization of Complex Atoms and Atomic Ions in a Varying Electromagnetic-Field,* Zh. Eksp. Teor. Fiz. **91**, 2008-2013 (1986).

5. P. Antici, J. Fuchs, S. Atzeni, A. Benuzzi, E. Brambrink, M. Esposito, M. Koenig, A. Ravasio, J. Schreiber, A. Schiavi, and P. Audebert, *Isochoric heating of matter by laser-accelerated high-energy protons,* J. Phys. IV France **133**, 1077-1079 (2006).

6. T. Ao, Y. Ping, K. Widmann, D.F. Price, E. Lee, H. Tam, P.T. Springer, and A. Ng, *Optical Properties in Nonequilibrium Phase Transitions,* Phys. Rev. Lett. **96**, 4 (2006).

7. S. Atzeni, *Inertial fusion fast ignitor: Igniting pulse parameter window vs the penetration depth of the heating particles and the density of the precompressed fuel,* Phys. Plasmas **6**, 3316-3326 (1999).

8. S. Atzeni, *Laser-plasma interaction and high-pressure generation for inertial fusion and basic science,* Plasma Phys. Control. Fusion **42**, B143-B155 (2000).

9. P. Audebert, P. Renaudin, S. Bastiani-Ceccotti, J.P. Geindre, C. Chenais-Popovics, S. Tzortzakis, V. Nagels-Silvert, R. Shepherd, I. Matsushima, S. Gary, F. Girard, O. Peyrusse, and J.C. Gauthier, *Picosecond Time-Resolved*

X-Ray Absorption Spectroscopy of Ultrafast Aluminum Plasmas, Phys. Rev. Lett. **94**, 25004 (2005).

10. T. Auguste, P. Monot, La Lompre, G. Mainfray, and C. Manus, *Multiply charged ions produced in noble gases by a 1 ps laser pulse at λ=1053 nm,* J. Phys. B: At., Mol. Opt. Phys. **25**, 4181-4194 (1992).

11. A. Bar-Shalom, M. Klapisch, and J. Oreg, *Electron collision excitations in complex spectra of ionized heavy atoms,* Phys. Rev. A **38**, 1773-1784 (1988).

12. A. Bar-Shalom, M. Klapisch, and J. Oreg, *HULLAC, an integrated computer package for atomic processes in plasmas,* J. Quant. Spectrosc. Radiat. Transfer **71**, 169-188 (2001).

13. A. Bar-Shalom, J. Oreg, W.H. Goldstein, D. Shvarts, and A. Zigler, *Super-transition-arrays: A model for the spectral analysis of hot, dense plasma,* Phys. Rev. A **40**, 3183-3193 (1989).

14. D. Batani, C.J. Joachain, S. Martellucci, and A.N. Chester, *Atoms, Solids, and Plasmas in Super-intense Laser Fields* (Kluwer Academic/Plenum, New York, 2001).

15. S.D. Baton, M. Koenig, J. Fuchs, A. Benuzzi-Mounaix, P. Guillou, B. Loupias, T. Vinci, L. Gremillet, C. Rousseaux, M. Drouin, E. Lefebvre, F. Dorchies, C. Fourment, J.J. Santos, D. Batani, A. Morace, R. Redaelli, M. Nakatsutsumi, R. Kodama, A. Nishida, N. Ozaki, T. Norimatsu, Y. Aglitskiy, S. Atzeni, and A. Schiavi, *Inhibition of fast electron energy deposition due to preplasma filling of cone-attached targets,* Phys. Plasmas **15**, 42706 (2008).

16. S.D. Baton, J.J. Santos, F. Amiranoff, H. Popescu, L. Gremillet, M. Koenig, E. Martinolli, O. Guilbaud, C. Rousseaux, Le Gloahec, T. Hall, D. Batani, E. Perelli, F. Scianitti, and T.E. Cowan, *Evidence of ultrashort electron bunches in laser-plasma interactions at relativistic intensities,* Phys. Rev. Lett. **91**, 105001 (2003).

17. D. Bauer, P. Mulser, and W.H. Steeb, *Relativistic Ponderomotive Force, Uphill Acceleration, and Transition to Chaos,* Phys. Rev. Lett. **75**, 4622-4625 (1995).

18. F.N. Beg, A.R. Bell, A.E. Dangor, C.N. Danson, A.P. Fews, M.E. Glinsky, B.A. Hammel, P. Lee, P.A. Norreys, and M. Tatarakis, *A study of picosecond laser-solid interactions up to 10^{19} W cm^{-2},* Phys. Plasmas **4**, 447-457 (1997).

19. A.R. Bell, Davies, JR, and S.M. Guerin, *Magnetic field in short-pulse high-intensity laser-solid experiments,* Phys. Rev. E **58**, 2471-2473 (1998).

20. A.R. Bell, and R.J. Kingham, *Resistive collimation of electron beams in laser-produced plasmas,* Phys. Rev. Lett. **91**, 35003 (2003).

21. H.F. Berg, H.R. Griem, R. Lincke, and A.W. Ali, *Measurement of Stark Profiles of Neutral and Ionized Helium and Hydrogen Lines from Shock-Heated Plasmas in Electromagnetic T Tubes,* Phys. Rev. **125**, 199 (1962).

22. M.J. Berger, J.S. Coursey, M.A. Zucker, and J. Chang, *Stopping-Power and Range Tables for Electrons, Protons, and Helium Ions*, http://physics.nist.gov/PhysRefData/Star/Text/contents.html.

23. A. Bergmann, S. Huller, P. Mulser, and H. Schnabl, *Resonance absorption by nonlinear electron plasma waves,* Europhys. Lett. **14**, 661-666 (1991).

24. A. Bergmann, and P. Mulser, *Breaking of resonantly excited electron plasma waves,* Phys. Rev. E **47**, 3585-3589 (1993).

25. V.R. Bhardwaj, P.P. Rajeev, P.B. Corkum, and D.M. Rayner, *Strong field ionization inside transparent solids,* J. Phys. B: At., Mol. Opt. Phys. **39**, S397-S407 (2006).

26. C.K. Birdsall, and A.B. Langdon, *Plasma Physics Via Computer Simulation* (McGraw-Hill, New York, 1995).

27. R. Boehler, *Temperature in Earth's core from melting-point measurements of iron at high static pressures,* Nature **363**, 534-536 (1993).

28. M. Bonitz, and D. Semkat, *Introduction to Computational Methods in Many Body Physics* (Rinton, Paramus, New Jersey, 2006).

29. M. Borghesi, S. Kar, L. Romagnani, T. Toncian, P. Antici, P. Audebert, E. Brambrink, F. Ceccherini, C.A. Cecchetti, J. Fuchs, M. Galimberti, L.A. Gizzi, T. Grismayer, T. Lyseikina, R. Jung, A. Macchi, P. Mora, J. Osterholz, A. Schiavi, and O. Willi, *Impulsive electric fields driven by high-intensity laser matter interactions,* Laser Part. Beams **25**, 161-167 (2007).

30. M. Borghesi, A.J. Mackinnon, L. Barringer, R. Gaillard, La Gizzi, C. Meyer, O. Willi, A. Pukhov, and J. MeyerterVehn, *Relativistic channeling of a*

picosecond laser pulse in a near-critical preformed plasma, Phys. Rev. Lett. **78**, 879-882 (1997).

31. M. Borghesi, A.J. Mackinnon, A.R. Bell, G. Malka, C. Vickers, O. Willi, J.R. Davies, A. Pukhov, and J. Meyer-Ter-Vehn, *Observations of collimated ionization channels in aluminum-coated glass targets irradiated by ultraintense laser pulses,* Phys. Rev. Lett. **83**, 4309-4312 (1999).

32. M. Borghesi, A.J. Mackinnon, D.H. Campbell, D.G. Hicks, S. Kar, P.K. Patel, D. Price, L. Romagnani, A. Schiavi, and O. Willi, *Multi-MeV proton source investigations in ultraintense laser-foil interactions,* Phys. Rev. Lett. **92**, 55003 (2004).

33. M. Borghesi, A.J. Mackinnon, R. Gaillard, O. Willi, and D. Riley, *Absorption of subpicosecond uv laser pulses during interaction with solid targets,* Phys. Rev. E **60**, 7374-7381 (1999).

34. M. Borghesi, C.A. Cecchetti, T. Toncian, J. Fuchs, L. Romagnani, S. Kar, P.A. Wilson, P. Antici, P. Audebert, E. Brambrink, A. Pipahl, M. Amin, R. Jung, J. Osterholz, O. Willi, W. Nazarov, R.J. Clarke, M. Notley, D. Neely, P. Mora, T. Grismayer, G. Schurtz, A. Schiavi, Y. Sentoku, and E. d'Humieres, *Laser-driven proton beams: Acceleration mechanism, beam optimization, and radiographic applications,* IEEE T. Plasma Sci. **36**, 1833-1842 (2008).

35. M. Born, and E. Wolf, *Principles of Optics* (Cambridge University Press, Cambridge, 1970).

36. E. Brambrink, T. Schlegel, G. Malka, K.U. Amthor, M.M. Aléonard, G. Claverie, M. Gerbaux, F. Gobet, F. Hannachi, V. Méot, P. Morel, P. Nicolai, J.N. Scheurer, M. Tarisien, V. Tikhonchuk, and P. Audebert, *Direct evidence of strongly inhomogeneous energy deposition in target heating with laser-produced ion beams,* Phys. Rev. E **75**, 4 (2007).

37. F. Brandl, G. Pretzler, D. Habs, and E. Fill, *Cerenkov radiation diagnostics of hot electrons generated by fs-laser interaction with solid targets,* Europhys. Lett. **61**, 632-638 (2003).

38. F. Brunel, *Not-So-Resonant, Resonant Absorption,* Phys. Rev. Lett. **59**, 52-55 (1987).

39. F. Califano, D.D. Sarto, and F. Pegoraro, *Three-Dimensional Magnetic Structures Generated by the Development of the Filamentation (Weibel) Instability in the Relativistic Regime,* Phys. Rev. Lett. **96** (2006).

40. P.J. Catto, and R.M. More, *Sheath Inverse Bremsstrahlung in Laser-Produced Plasmas,* Phys. Fluids **20**, 704-705 (1977).

41. P. Celliers, and A. Ng, *Optical probing of hot expanded states produced by shock release,* Phys. Rev. E **47**, 3547-3565 (1993).

42. M. Cerchez, R. Jung, J. Osterholz, T. Toncian, O. Willi, P. Mulser, and H. Ruhl, *Absorption of ultrashort laser pulses in strongly overdense targets,* Phys. Rev. Lett. **100**, 245001 (2008).

43. L.M. Chen, J. Zhang, Q.L. Dong, H. Teng, T.J. Liang, L.Z. Zhao, and Z.Y. Wei, *Hot electron generation via vacuum heating process in femtosecond laser-solid interactions,* Phys. Plasmas **8**, 2925-2929 (2001).

44. M.H. Chen, E. Laiman, B. Crasemann, M. Aoyagi, and H. Mark, *Relativistic L-shell Auger and Coster-Kronig rates and fluorescence yields,* Phys. Rev. A **19**, 2253-2259 (1979).

45. M.L. Cherry, G. Hartmann, D. Muller, and T.A. Prince, *Transition radiation from relativistic electrons in periodic radiators,* Phys. Rev. D **10**, 3594-3607 (1974).

46. M.L. Cherry, and D. Muller, *Measurements of the Frequency Spectrum of Transition Radiation,* Phys. Rev. Lett. **38**, 5-8 (1977).

47. B.I. Cho, G.M. Dyer, S. Kneip, S. Pikuz, D.R. Symes, A.C. Bernstein, Y. Sentoku, N.R.-L. Galloudec, T.E. Cowan, and T. Ditmire, *Hot electron generation from intense laser irradiation of microtipped cone and wedge targets,* Phys. Plasmas **15**, 52701 (2008).

48. B.I. Cho, J. Osterholz, N.R.-L. Galloudec, A.C. Bernstein, G. Dyer, and T. Ditmire, *Study of hot electron transport in foil, wedge, and cone targets irradiated with ultraintense laser pulses,* J. Opt. Soc. Am. B **25**, B50-B56 (2008).

49. B.-I. Cho, J. Osterholz, A.C. Bernstein, G.M. Dyer, A. Karmakar, A. Pukhov, and T. Ditmire, *Observation of Two Distinct Hot Electron Beams in Intense Laser-Solid Interactions,* submitted to Phys. Rev. Lett.

50. H. Chung, M. Chen, W. Morgan, Y. Ralchenko, and R. Lee, *FLYCHK: Generalized population kinetics and spectral model for rapid spectroscopic analysis for all elements,* High Energy Density Physics **1**, 3-12 (2005).

51. H.K. Chung, W.L. Morgan, and R.W. Lee, *FLYCHK: an extension to the K-shell spectroscopy kinetics model FLY,* J. Quant. Spectrosc. Radiat. Transfer **81**, 107-115 (2003).

52. E.L. Clark, K. Krushelnick, J.R. Davies, M. Zepf, M. Tatarakis, F.N. Beg, A. Machacek, P.A. Norreys, M.I. Santala, I. Watts, and A.E. Dangor, *Measurements of energetic proton transport through magnetized plasma from intense laser interactions with solids,* Phys. Rev. Lett. **84**, 670-673 (2000).

53. G.W. Collins, L.D. Silva, P. Celliers, D.M. Gold, M.E. Foord, R.J. Wallace, A. Ng, S.V. Weber, K.S. Budil, and R. Cauble, *Measurements of the equation of state of deuterium at the fluid insulator-metal transition,* Science **281**, 1178-1181 (1998).

54. C.N. Danson, P.A. Brummitt, R.J. Clarke, J.L. Collier, B. Fell, A.J. Frackiewicz, S. Hancock, S. Hawkes, C. Hernandez-Gomez, P. Holligan, M.H.R. Hutchinson, A. Kidd, W.J. Lester, I.O. Musgrave, D. Neely, D.R. Neville, P.A. Norreys, D.A. Pepler, C.J. Reason, W. Shaikh, T.B. Winstone, R.W.W. Wyatt, and B.E. Wyborn, *Vulcan Petawatt--an ultra-high-intensity interaction facility,* Nucl. Fusion **44**, S239-S246 (2004).

55. J.R. Davies, *The Alfven limit revisited and its relevance to laser-plasma interactions,* Laser Part. Beams **24**, 299-310 (2006).

56. J.R. Davies, J.S. Green, and P.A. Norreys, *Electron beam hollowing in laser-solid interactions,* Plasma Phys. Control. Fusion **48**, 1181-1199 (2006).

57. E. Dewald, C. Constantin, S. Udrea, J. Jacoby, D.H. Hoffmann, C. Niemann, J. Wieser, N.A. Tahir, A. Kozyreva, A. Shutov, and A. Tauschwitz, *Studies of high energy density in matter driven by heavy ion beams in solid targets,* Laser Part. Beams **20**, 399-403 (2002).

58. T. Ditmire, E.W. Gaul, and M.D. Martinez, *Conceptual Design Report for the Texas Petawatt Laser* http://www.ph.utexas.edu/~utlasers/papers/petawatt_cdr.pdf

59. R. Drake, *High-energy-density Physics: Fundamentals, Inertial Fusion, and Experimental Astrophysics* (Springer, Berlin, 2006).

60. G. Dyer, R. Sheppherd, J. Kuba, E. Fill, A. Wootton, P. Patel, D. Price, and T. Ditmire, *Isochoric heating of solid aluminium with picosecond X-ray pulses,* Journal of Modern Optics **50**, 2495-2505 (2003).

61. G.M. Dyer, A.C. Bernstein, B.I. Cho, J. Osterholz, W. Grigsby, A. Dalton, R. Shepherd, Y. Ping, H. Chen, K. Widmann, and T. Ditmire, *Equation-of-state measurement of dense plasmas heated with fast protons,* Phys. Rev. Lett. **101**, 15002 (2008).

62. B. Edlen, and F. Tyren, *Atomic energy states of an unusual type,* Nature **143** (1939).

63. J. Edwards, K.T. Lorenz, B.A. Remington, S. Pollaine, J. Colvin, D. Braun, B.F. Lasinski, D. Reisman, J.M. McNaney, J.A. Greenough, R. Wallace, H. Louis, and D. Kalantar, *Laser-driven plasma loader for shockless compression and acceleration of samples in the solid state,* Phys. Rev. Lett. **92**, 75002 (2004).

64. T. Eichner, F. Grüner, S. Becker, M. Fuchs, D. Habs, R. Weingartner, U. Schramm, H. Backe, P. Kunz, and W. Lauth, *Miniature magnetic devices for laser-based, table-top free-electron lasers,* Phys. Rev. ST Accel. Beams **10**, 9 (2007).

65. K. Eidmann, U. Andiel, F. Pisani, P. Hakel, R.C. Mancini, G.C. Junkel-Vives, J. Abdallah, and K. Witte, *K-shell spectra from hot dense aluminum layers buried in carbon and heated by ultrashort laser pulses,* J. Quant. Spectrosc. Radiat. Transfer **81**, 133-146 (2003).

66. K. Eidmann, J. Meyer-Ter-Vehn, T. Schlegel, and S. Huller, *Hydrodynamic simulation of subpicosecond laser interaction with solid-density matter,* Phys. Rev. E **62**, 1202-1214 (2000).

67. K. Eidmann, R. Rix, T. Schlegel, and K. Witte, *Absorption of intense high-contrast sub-picosecond laser pulses in solid targets,* Europhys. Lett. **55**, 334-340 (2001).

68. S. Eliezer, *The Interaction of High-power Lasers with Plasmas* (Institute of Physics Publishing, Bristol, 2002).

69. D. Errandonea, *Phase behavior of metals at very high P-T conditions: A review of recent experimental studies,* J. Phys. Chem. Solids **67**, 2017-2026 (2006).

70. *FAIR Baseline Technical Report Executive Summary* (2006) http://www.gsi.de/fair/reports/btr.html.

71. *FAIR Baseline Technical Report Volume 5* (2006) http://www.gsi.de/fair/reports/btr.html.

72. J. Faure, V. Malka, Marques, JR, P.G. David, F. Amiranoff, K.T. Phuoc, and A. Rousse, *Effects of pulse duration on self-focusing of ultra-short lasers in underdense plasmas,* Phys. Plasmas **9**, 756-759 (2002).

73. R. Fedosejevs, R. Ottmann, R. Sigel, G. Kuhnle, S. Szatmari, and F.P. Schafer, *Absorption of Femtosecond Laser Pulses in High-Density Plasma,* Phys. Rev. Lett. **64**, 1250-1253 (1990).

74. R. Fedosejevs, X.F. Wang, and G.D. Tsakiris, *Onset of relativistic self-focusing in high density gas jet targets,* Phys. Rev. E **56**, 4615-4639 (1997).

75. T. Feurer, W. Theobald, R. Sauerbrey, I. Uschmann, D. Altenbernd, U. Teubner, P. Gibbon, E. Forster, G. Malka, and J.L. Miquel, *Onset of diffuse reflectivity and fast electron flux inhibition in 528-nm-laser solid interactions at ultrahigh intensity,* Phys. Rev. E **56**, 4608-4614 (1997).

76. E.E. Fill, *Kinetics of ultrashort relativistic electron pulses emitted from solid targets,* Phys. Rev. E **70**, 5 (2004).

77. E.E. Fill, *Ultrashort-pulse laser plasmas: Fraction of hot electrons escaping from the target and electron spectra in planar and spherical geometry,* Phys. Plasmas **12**, 52704 (2005).

78. K.A. Flippo, E. D‘humières, S.A. Gaillard, J. Rassuchine, D.C. Gautier, M. Schollmeier, F. Nürnberg, J.L. Kline, J. Adams, B. Albright, M. Bakeman, K. Harres, R.P. Johnson, G. Korgan, S. Letzring, S. Malekos, N. Renard-Legalloudec, Y. Sentoku, T. Shimada, M. Roth, T.E. Cowan, J.C. Fernández, and B.M. Hegelich, *Increased efficiency of short-pulse laser-generated proton beams from novel flat-top cone targets,* Phys. Plasmas **15**, 56709 (2008).

79. R.A. Fonseca, L.O. Silva, J.W. Tonge, W.B. Mori, and J.M. Dawson, *Three-dimensional Weibel instability in astrophysical scenarios,* Phys. Plasmas **10**, 1979 (2003).

80. M.E. Foord, D.B. Reisman, and P.T. Springer, *Determining the equation-of-state isentrope in an isochoric heated plasma,* Rev. Sci. Instrum. **75**, 2586 (2004).

81. J. Fuchs, P. Antici, E. D'humières, E. Lefebvre, M. Borghesi, E. Brambrink, C.A. Cecchetti, M. Kaluza, V. Malka, M. Manclossi, S. Meyroneinc, P. Mora, J. Schreiber, T. Toncian, H. Pépin, and P. Audebert, *Laser-driven proton scaling laws and new paths towards energy increase,* Nat. Phys. **2**, 48-54 (2006).

82. J. Fuchs, G. Malka, J.C. Adam, F. Amiranoff, S.D. Baton, N. Blanchot, A. Heron, G. Laval, J.L. Miquel, P. Mora, H. Pepin, and C. Rousseaux, *Dynamics of subpicosecond relativistic laser pulse self-channeling in an underdense preformed plasma,* Phys. Rev. Lett. **80**, 1658-1661 (1998).

83. A.H. Gabriel, and C. Jordan, *Long Wavelength Satellites to He-Like Ion Resonance Lines in Laboratory and in the Sun,* Nature **221**, 947 (1969).

84. N.R.-L. Galloudec, E. d'Humieres, B.-I. Cho, J. Osterholz, Y. Sentoku, and T. Ditmire, *Guiding, focusing and collimated transport of hot electrons in a canal in the extended tip of cone targets,* submitted to Phys. Rev. Lett.

85. N.R.-L. Galloudec, B.-I. Cho, J. Osterholz, and T. Ditmire, *Controlled reproducible alignment of cone targets and mitigation of preplasma in high intensity laser interactions,* Rev. Sci. Instrum. **79**, 83506 (2008).

86. G.M. Garibian, *Contribution to the theory of transition radiation,* Sov. Phys. JETP-USSR **6**, 1079-1085 (1958).

87. J.C. Gauthier, J.P. Geindre, P. Audebert, S. Bastiani, C. Quoix, G. Grillon, A. Mysyrowicz, A. Antonetti, and R.C. Mancini, *Theoretical and experimental studies of laser-produced plasmas driven by high-intensity femtosecond laser pulses,* Phys. Plasmas **4**, 1811-1817 (1997).

88. J.P. Geindre, P. Audebert, S. Rebibo, and J.C. Gauthier, *Single-shot spectral interferometry with chirped pulses,* Opt. Lett. **26**, 1612-1614 (2001).

89. P. Gibbon, and A.R. Bell, *Collisionless Absorption in Sharp-Edged Plasmas,* Phys. Rev. Lett. **68**, 1535-1538 (1992).

90. P. Gibbon, *Short Pulse Laser Interactions With Matter: An Introduction* (Imperial College Press, London, 2005).

91. V. Ginsburg, and I. Frank, *Radiation of a uniformly moving electron due to its transition from one medium into another,* Zh. Eksp. Teor. Fiz. **16**, 15-28 (1946).

92. V. Ginzburg, *The Propagation of Electromagnetic Waves in Plasmas* (Pergamon Press, Oxford, New York, 1970).

93. S.H. Glenzer, G. Gregori, R.W. Lee, F.J. Rogers, S.W. Pollaine, and O.L. Landen, *Demonstration of spectrally resolved x-ray scattering in dense plasmas,* Phys. Rev. Lett. **90**, 175002 (2003).

94. S.H. Glenzer, O.L. Landen, P. Neumayer, R.W. Lee, K. Widmann, S.W. Pollaine, R.J. Wallace, A. Höll, T. Bornath, R. Thiele, V. Schwarz, W.D. Kraeft, and R. Redmer, *Observations of Plasmons in Warm Dense Matter,* Phys. Rev. Lett. **98**, 4 (2007).

95. Y. Gontier, M. Poirier, and M. Trahin, *Multiphoton absorptions above the ionization threshold,* J. Phys. B: At., Mol. Opt. Phys. **13**, 1381-1387 (1980).

96. J.S. Green, V.M. Ovchinnikov, R.G. Evans, K.U. Akli, H. Azechi, F.N. Beg, C. Bellei, R.R. Freeman, H. Habara, R. Heathcote, M.H. Key, J.A. King, K.L. Lancaster, N.C. Lopes, T. Ma, A.J. Mackinnon, K. Markey, A. Mcphee, Z. Najmudin, P. Nilson, R. Onofrei, R. Stephens, K. Takeda, K.A. Tanaka, W. Theobald, T. Tanimoto, J. Waugh, L. van Woerkom, N.C. Woolsey, M. Zepf, J.R. Davies, and P.A. Norreys, *Effect of Laser Intensity on Fast-Electron-Beam Divergence in Solid-Density Plasmas,* Phys. Rev. Lett. **100**, 4 (2008).

97. G. Gregori, S.H. Glenzer, W. Rozmus, R.W. Lee, and O.L. Landen, *Theoretical model of x-ray scattering as a dense matter probe,* Phys. Rev. E **67**, 10 (2003).

98. H.R. Griem, *Principles of Plasma Spectroscopy*, (Cambridge University Press, Cambridge, 1997).

99. U. Happek, A.J. Sievers, and E.B. Blum, *Observation of Coherent Transition Radiation,* Phys. Rev. Lett. **67**, 2962-2965 (1991).

100. S.P. Hatchett, C.G. Brown, T.E. Cowan, E.A. Henry, J.S. Johnson, M.H. Key, J.A. Koch, A.B. Langdon, B.F. Lasinski, R.W. Lee, A.J. Mackinnon, D.M. Pennington, M.D. Perry, T.W. Phillips, M. Roth, T.C. Sangster, M.S. Singh, R.A. Snavely, M.A. Stoyer, S.C. Wilks, and K. Yasuike, *Electron, photon,*

and ion beams from the relativistic interaction of Petawatt laser pulses with solid targets, Phys. Plasmas **7**, 2076-2082 (2000).

101. B.M. Hegelich, B.J. Albright, J. Cobble, K. Flippo, S. Letzring, M. Paffett, H. Ruhl, J. Schreiber, R.K. Schulze, and J.C. Fernández, *Laser acceleration of quasi-monoenergetic MeV ion beams,* Nature **439**, 441-444 (2006).

102. B.L. Henke, E.M. Gullikson, and J.C. Davis, *X-ray interactions: photoabsorption, scattering, transmission, and reflection at E=50-30000 eV, Z=1-92,* Atomic Data and Nuclear Data Tables **54**, 181-342 (1993).

103. M. Hentschel, Z. Cheng, F. Krausz, and C. Spielmann, *Generation of 0.1-TW optical pulses with a single-stage Ti,* Appl. Phys. B: Lasers Opt. **70**, S161-S164 (2000).

104. D. Hoffmann, A. Blazevic, S. Korostiy, P. Ni, S. Pikuz, B. Rethfeld, O. Rosmej, M. Roth, N. Tahir, and S. Udrea, *Inertial fusion energy issues of intense heavy ion and laser beams interacting with ionized matter studied at GSI-Darmstadt,* Nuclear Instruments and Methods in Physics Research Section A: Accelerators, Spectrometers, Detectors and Associated Equipment **577**, 8-13 (2007).

105. K.S. Holian, *T-4 Handbook of Material Properties Data Bases Vol. Ic: Equations of State,* Los Alamos National Laboratory Report No LA-10160-MS UC-34, 382 (1984).

106. A. Höll, R. Redmer, G. Röpke, and H. Reinholz, *X-ray Thomson scattering in warm dense matter,* Eur. Phys. J. D **29**, 159-162 (2004).

107. M. Honda, J. Meyer-Ter-Vehn, and A. Pukhov, *Collective stopping and ion heating in relativistic-electron-beam transport for fast ignition,* Phys. Rev. Lett. **85**, 2128-2131 (2000).

108. J. Honrubia, and J. Meyer-Ter-Vehn, *Three-dimensional fast electron transport for ignition-scale inertial fusion capsules,* Nucl. Fusion **46**, L25 (2006).

109. H. Hora, *Laser Plasma Physics: Forces and the Nonlinearity Principle* (SPIE Press, Bellingham, WA, 2000).

110. K. Horioka, T. Kawamura, M. Nakajima, T. Sasaki, K. Kondo, Y. Yano, T. Ishii, M. Ogawa, Y. Oguri, and J. Hasegawa, *High-energy-density physics*

researches based on heavy ion accelerator and pulse power devices, Nuclear Instruments and Methods in Physics Research Section A: Accelerators, Spectrometers, Detectors and Associated Equipment **577**, 298-302 (2007).

111. W.F. Huebner, A.L. Merts, N.H. Magee, and M.F. Argo, *Astrophysical Opacity Library,* Los Alamos National Laboratory Report No LA-6760-M UC-34b (1977).

112. G. Huser, M. Koenig, A. Benuzzi-Mounaix, E. Henry, T. Vinci, B. Faral, M. Tomasini, B. Telaro, and D. Batani, *Temperature and melting of laser-shocked iron releasing into an LiF window,* Phys. Plasmas **12**, 60701 (2005).

113. S. Ichimaru, *Strongly coupled plasmas: high-density classical plasmas and degenerate electron liquids,* Rev. Mod. Phys. **54**, 1017-1059 (1982).

114. C.A. Iglesias, and F.J. Rogers, *Opacity tables for cepheid variables,* Astrophys. J. **371**, L73-L75 (1991).

115. C.A. Iglesias, F.J. Rogers, and B.G. Wilson, *Reexamination of the metal contribution to astrophysical opacity,* Astrophys. J. **322**, L45-L48 (1987).

116. Inglis, and E. Teller, *Ionic depression of series limits in one-electron spectra,* Astrophys. J. **90**, 439 (1939).

117. J.D. Jackson, *Classical Electrodynamics* (John Wiley & Sons, Hoboken, NJ, 1999).

118. R. Jung, J. Osterholz, K. Lowenbruck, S. Kiselev, G. Pretzler, A. Pukhov, O. Willi, S. Kar, M. Borghesi, W. Nazarov, S. Karsch, R. Clarke, and D. Neely, *Study of electron-beam propagation through preionized dense foam plasmas,* Phys. Rev. Lett. **94**, 195001 (2005).

119. A. Kaiser, B. Rethfeld, M. Vicanek, and G. Simon, *Microscopic processes in dielectrics under irradiation by subpicosecond laser pulses,* Phys. Rev. B **61**, 11437-11450 (2000).

120. S. Kar, M. Borghesi, C.A. Cecchetti, L. Romagnani, F. Ceccherini, T.V. Liseykina, A. Macchi, R. Jung, J. Osterholz, O. Willi, L.A. Gizzi, A. Schiavi, M. Galimberti, and R. Heathcote, *Dynamics of charge-displacement channeling in intense laser-plasma interactions,* New J. Phys. **9**, 402 (2007).

121. A. Karmakar, N. Kumar, A. Pukhov, O. Polomarov, and G. Shvets, *Three-dimensional filamentary structures of a relativistic electron beam in fast ignition plasmas,* Phys. Plasmas **15**, 120702 (2008).

122. W. Karzas, and R. Latter, *Electron Radiative Transitions in a Coulomb Field,* The Astrophysical Journal Supplement Series (1961).

123. L.V. Keldysh, *Ionization in the field of a strong electromagnetic wave,* Sov. Phys. JETP-USSR **20**, 1307 (1965).

124. R.L. Kelly, *Atomic and Ionic Spectrum Lines Below 2000 Angstroms: Hydrogen through Krypton,* Journal of Physical and Chemical Reference Data **16** (1987).

125. A.J. Kemp, and J. Meyer-Ter-Vehn, *An equation of state code for hot dense matter, based on the QEOS description,* Nucl. Instrum. Meth. A **415**, 674-676 (1998).

126. M.H. Key, K. Akli, F. Beg, M.H. Chen, H.K. Chung, R.R. Freeman, M.E. Foord, J.S. Green, P. Gu, G. Gregori, H. Habara, S.P. Hatchett, D. Hey, J.M. Hill, J.A. King, R. Kodama, J.A. Koch, K. Lancaster, B.F. Lasinski, B. Langdon, A.J. Mackinnon, C.D. Murphy, P.A. Norreys, N. Patel, P. Patel, J. Pasley, R.A. Snavely, R.B. Stephens, C. Stoeckl, M. Tabak, W. Theobald, K. Tanaka, R. Town, S.C. Wilks, T. Yabuuchi, and B. Zhang, *Study of electron and proton isochoric heating for fast ignition,* J. Phys. IV France **133**, 371-378 (2006).

127. J.C. Kieffer, P. Audebert, M. Chaker, J.P. Matte, H. Pepin, T.W. Johnston, P. Maine, D. Meyerhofer, J. Delettrez, D. Strickland, P. Bado, and G. Mourou, *Short-Pulse Laser Absorption in Very Steep Plasma Density Gradients,* Phys. Rev. Lett. **62**, 760-763 (1989).

128. J.C. Kieffer, A. Krol, Z. Jiang, C.C. Chamberlain, E. Scalzetti, and Z. Ichalalene, *Future of laser-based X-ray sources for medical imaging,* Applied Physics B: Lasers and Optics **74**, S75-S81 (2002).

129. P. Kirkpatrick, and A.V. Baez, *Formation of optical images by x-rays,* J. Opt. Soc. Am. **38**, 766-774 (1948).

130. T. Kita, T. Harada, N. Nakano, and H. Kuroda, *Mechanically ruled aberration-corrected concave gratings for a flat-field grazing-incidence spectrograph,* Appl. Optics **22**, 512-513 (1983).

131. M.D. Knudson, D.L. Hanson, J.E. Bailey, C.A. Hall, J.R. Asay, and C. Deeney, *Principal Hugoniot, reverberating wave, and mechanical reshock measurements of liquid deuterium to 400 GPa using plate impact techniques,* Phys. Rev. B **69**, 20 (2004).

132. R. Kodama, *Nuclear fusion - Fast heating scalable to laser fusion ignition,* Nature **418**, 933-934 (2002).

133. R. Kodama, Y. Sentoku, Z.L. Chen, G.R. Kumar, S.P. Hatchett, Y. Toyama, T.E. Cowan, R.R. Freeman, J. Fuchs, Y. Izawa, M.H. Key, Y. Kitagawa, K. Kondo, T. Matsuoka, H. Nakamura, M. Nakatsutsumi, P.A. Norreys, T. Norimatsu, R.A. Snavely, R.B. Stephens, M. Tampo, K.A. Tanaka, and T. Yabuuchi, *Plasma devices to guide and collimate a high density of MeV electrons,* Nature **432**, 1005-1008 (2004).

134. N. Krall, and A.W. Trivelpiece, *Principles of Plasma Physics* (San Francisco Press, San Francisco, 1986).

135. H.A. Kramers, *On the theory of X-ray absorption and the continuous X-ray Spectrum,* Philosophical Magazine **46**, 836 (1923).

136. G. Kresse, and J. Furthmuller, *Efficient iterative schemes for ab initio total-energy calculations using a plane-wave basis set,* Phys. Rev. B **54**, 11169-11186 (1996).

137. G. Kresse, and J. Hafner, *Ab initio molecular dynamics for liquid metals,* Phys. Rev. B **47**, 558-561 (1993).

138. G. Kresse, and J. Hafner, *Ab initio molecular-dynamics simulation of the liquid-metal-amorphous-semiconductor transition in germanium,* Phys. Rev. B **49**, 14251-14269 (1994).

139. W.L. Kruer, and K. Estabrook, *JxB heating by very intense laser light,* Phys. Fluids **28**, 430-432 (1985).

140. W. Kruer, *The Physics of Laser Plasma Interactions* (Westview Press, Boulder, CO, 2003).

141. O.L. Landen, S.H. Glenzer, M.J. Edwards, R.W. Lee, G.W. Collins, R.C. Cauble, W.W. Hsing, and B.A. Hammel, *Dense matter characterization by X-ray Thomson scattering,* J. Quant. Spectrosc. Radiat. Transfer **71**, 465-478 (2001).

142. J.T. Larsen, and S.M. Lane, *HYADES - A Plasma Hydrodynamics Code for Dense-Plasma Studies,* J. Quant. Spectrosc. Radiat. Transfer **51**, 179-186 (1994).

143. R.W. Lee, *Plasma line shapes for selected transitions in hydrogen-, helium- and lithium-like ions,* J. Quant. Spectrosc. Radiat. Transfer **40**, 561-568 (1988).

144. R.W. Lee, *The How To For FLY* (1995) http://nlte.nist.gov/FLY/Doc/FLY95.pdf.

145. R.W. Lee, *The How To For FLYCHK @ NIST* (2008) http://nlte.nist.gov/FLY/Doc/Manual_FLYCHK_Nov08.pdf.

146. R.W. Lee, H.A. Baldis, R.C. Cauble, O.L. Landen, J.S. Wark, A. Ng, S.J. Rose, C. Lewis, D. Riley, J.C. Gauthier, and P. Audebert, *Plasma-based studies with intense X-ray and particle beam sources,* Laser Part. Beams **20**, 527-536 (2002).

147. R.W. Lee, and J.T. Larsen, *A time-dependent model for plasma spectroscopy of K-shell emitters,* J. Quant. Spectrosc. Radiat. Transfer **56**, 535-556 (1996).

148. *Linac Coherent Light Source* (2005) http://ssrl.slac.stanford.edu/lcls/downloads/lcls_brochure_print_opt.pdf.

149. J.D. Lindl, *Inertial Confinement Fusion: The Quest for Ignition and Energy Gain Using Indirect Drive* (Springer, Berlin, Heidelberg, 1998).

150. J.D. Lindl, P. Amendt, R.L. Berger, S.G. Glendinning, S.H. Glenzer, S.W. Haan, R.L. Kauffman, O.L. Landen, and L.J. Suter, *The physics basis for ignition using indirect-drive targets on the National Ignition Facility,* Phys. Plasmas **11**, 339 (2004).

151. W. Lochte-Holtgreven, *Plasma Diagnostics* (AIP Press, New York, 1968).

152. K. Lorenz, M. Edwards, A. Jankowski, S. Pollaine, R. Smith, and B. Remington, *High pressure, quasi-isentropic compression experiments on the Omega laser,* High Energy Density Physics **2**, 113-125 (2006).

153. W. Lotz, *An empirical formula for electron-impact ionization cross-section,* Z Phys **206**, 205 (1967).

154. W. Lotz, *Electron-impact ionization cross-sections and ionization rate coefficients for atoms and ions from hydrogen to calcium,* Z Phys **216**, 241 (1968).

155. A.H. Lumpkin, R. Dejus, W.J. Berg, M. Borland, Y.C. Chae, E. Moog, N.S. Sereno, and B.X. Yang, *First observation of z-dependent electron-beam microbunching using coherent transition radiation,* Phys. Rev. Lett. **86**, 79-82 (2001).

156. A. Maksimchuk, S. Gu, K. Flippo, D. Umstadter, and V.Y. Bychenkov, *Forward ion acceleration in thin films driven by a high-intensity laser,* Phys. Rev. Lett. **84**, 4108-4111 (2000).

157. A. Maksimchuk, M. Nantel, G. Ma, S. Gu, C.Y. Cote, D. Umstadter, S.A. Pikuz, I.Y. Skobelev, and A.Y. Faenov, *X-ray radiation from matter in extreme conditions,* J. Quant. Spectrosc. Radiat. Transfer **65**, 367-385 (2000).

158. E. Martinolli, M. Koenig, S.D. Baton, J.J. Santos, F. Amiranoff, D. Batani, E. Perelli-Cippo, F. Scianitti, L. Gremillet, R. Mélizzi, A. Decoster, C. Rousseaux, T.A. Hall, M.H. Key, R. Snavely, A.J. Mackinnon, R.R. Freeman, J.A. King, R. Stephens, D. Neely, and R.J. Clarke, *Fast-electron transport and heating of solid targets in high-intensity laser interactions measured by $K\alpha$ fluorescence,* Phys. Rev. E **73**, 5 (2006).

159. D.D. Meyerhofer, *High-intensity-laser-electron scattering,* IEEE J. Quantum Elect. **33**, 1935-1941 (1997).

160. P. Mora, *Plasma expansion into a vacuum,* Phys. Rev. Lett. **90**, 185002 (2003).

161. P. Mulser, and H. Ruhl, *Collisionless Laser-Energy Conversion by Anharmonic Resonance,* Phys. Rev. Lett. **101**, 4 (2008).

162. M.M. Murnane, H.C. Kapteyn, and R.W. Falcone, *High-Density Plasmas Produced by Ultrafast Laser Pulses,* Phys. Rev. Lett. **62**, 155-158 (1989).

163. M. Nantel, G. Ma, S. Gu, C.Y. Cote, J. Itatani, and D. Umstadter, *Pressure ionization and line merging in strongly coupled plasmas produced by 100-fs laser pulses,* Phys. Rev. Lett. **80**, 4442-4445 (1998).

164. National Research Council, Committee on High Energy Density Plasma Physics, *Frontiers in High Energy Density Physics: The X-games of Contemporary Science* (National Academy Press, Washington, DC, 2003).

165. N.M. Naumova, J.A. Nees, Sokolov, IV, B. Hou, and G.A. Mourou, *Relativistic generation of isolated attosecond pulses in a lambda(3) focal volume,* Phys. Rev. Lett. **92**, 63902 (2004).

166. A. Ng, T. Ao, F. Perrot, M.W. Dharma-Wardana, and M.E. Foord, *Idealized slab plasma approach for the study of warm dense matter,* Laser Part. Beams **23**, 527-537 (2005).

167. J. Nuckolls, A. Thiessen, L. Wood, and G. Zimmerman, *Laser Compression of Matter to Super-High Densities: Thermonuclear (CTR) Applications,* Nature **239**, 139 (1972).

168. J. Oostens, S. Prunster, C.L. Wang, and L.C. Yuan, *Transition radiation from relativistic charged particles and its energy dependence,* Phys. Rev. Lett. **19**, 541 (1967).

169. J. Osterholz, F. Brandl, M. Cerchez, T. Fischer, D. Hemmers, B. Hidding, A. Pipahl, G. Pretzler, S.J. Rose, and O. Willi, *Extreme ultraviolet emission from dense plasmas generated with sub-10-fs laser pulses,* Phys. Plasmas **15**, 103301 (2008).

170. J. Osterholz, F. Brandl, T. Fischer, D. Hemmers, M. Cerchez, G. Pretzler, O. Willi, and S.J. Rose, *Production of dense plasmas with sub-10-fs laser pulses,* Phys. Rev. Lett. **96**, 85002 (2006).

171. P.K. Patel, A.J. Mackinnon, M.H. Key, T.E. Cowan, M.E. Foord, M. Allen, D.F. Price, H. Ruhl, P.T. Springer, and R. Stephens, *Isochoric heating of solid-density matter with an ultrafast proton beam,* Phys. Rev. Lett. **91**, 125004 (2003).

172. A.M. Perelomov, V.S. Popov, and M.V. Terentev, *Ionization of atoms in an alternating electric field,* Sov. Phys. JETP-USSR **23**, 924 (1966).

173. M.D. Perry, D. Pennington, B.C. Stuart, G. Tietbohl, J.A. Britten, C. Brown, S. Herman, B. Golick, M. Kartz, J. Miller, H.T. Powell, M. Vergino, and V. Yanovsky, *Petawatt laser pulses,* Opt. Lett. **24**, 160-162 (1999).

174. G.J. Pert, *The analytic theory of linear resonant absorption,* Plasma Phys. Control. Fusion **20**, 175-188 (1978).

175. *Petawatt High Energy Laser for Heavy-Ion Experiments,* GSI Report, 44 (1998) http://www.gsi.de/onTEAM/grafik/1080122497/Phelix_A.pdf.

176. A. Pistelok, *Entwicklung eines OPCPA-Systems zur Verstärkung ultrakurzer Pulse bis in den Terawattbereich,* PhD Thesis in Physics at the Heinrich-Heine-University Düsseldorf (2006).

177. H. Popescu, S.D. Baton, F. Amiranoff, C. Rousseaux, M. Rabec Le Gloahec, J.J. Santos, L. Gremillet, M. Koenig, E. Martinolli, T. Hall, J.C. Adam, A. Heron, and D. Batani, *Subfemtosecond, coherent, relativistic, and ballistic electron bunches generated at* ω_0 *and* $2\omega_0$ *in high intensity laser-matter interaction,* Phys. Plasmas **12**, 63106 (2005).

178. G. Pretzler, T. Schlegel, E. Fill, and D. Eder, *Hot-electron generation in copper and photopumping of cobalt,* Phys. Rev. E **62**, 5618-5623 (2000).

179. D.F. Price, R.M. More, R.S. Walling, G. Guethlein, R.L. Shepherd, R.E. Stewart, and W.E. White, *Absorption of Ultrashort Laser-Pulses by Solid Targets Heated Rapidly to Temperatures 1-1000 eV,* Phys. Rev. Lett. **75**, 252-255 (1995).

180. A. Pukhov, *Three-dimensional electromagnetic relativistic particle-in-cell code VLPL (Virtual Laser Plasma Lab),* J. Plasma. Phys. **61**, 425-433 (1999).

181. A. Pukhov, and J. MeyerterVehn, *Relativistic magnetic self-channeling of light in near-critical plasma: Three-dimensional particle-in-cell simulation,* Phys. Rev. Lett. **76**, 3975-3978 (1996).

182. B. Quesnel, and P. Mora, *Theory and simulation of the interaction of ultraintense laser pulses with electrons in vacuum,* Phys. Rev. E **58**, 3719-3732 (1998).

183. D. Riley, La Gizzi, F.Y. Khattak, A.J. Mackinnon, S.M. Viana, and O. Willi, *Plasma Conditions Generated by Interaction of a High Brightness, Prepulse Free, Raman Amplified KrF Laser Pulse with Solid Targets,* Phys. Rev. Lett. **69**, 3739-3742 (1992).

184. D. Riley, N.C. Woolsey, D. McSherry, I. Weaver, A. Djaoui, and E. Nardi, *X-ray diffraction from a dense plasma,* Phys. Rev. Lett. **84**, 1704-1707 (2000).

185. A.P. Robinson, and M. Sherlock, *Magnetic collimation of fast electrons produced by ultraintense laser irradiation by structuring the target composition,* Phys. Plasmas **14**, 83105 (2007).

186. F.J. Rogers, and C.A. Iglesias, *Astrophysical Opacity,* Science **263**, 50-55 (1994).

187. L. Romagnani, M. Borghesi, C.A. Cecchetti, S. Kar, P. Antici, P. Audebert, S. Bandhoupadjay, F. Ceccherini, T. Cowan, J. Fuchs, M. Galimberti, L.A. Gizzi, T. Grismayer, R. Heathcote, R. Jung, T.V. Liseykina, A. Macchi, P. Mora, D. Neely, M. Notley, J. Osterholz, C.A. Pipahl, G. Pretzler, A. Schiavi, G. Schurtz, T. Toncian, P.A. Wilson, and O. Willi, *Proton probing measurement of electric and magnetic fields generated by ns and ps laser-matter interactions,* Laser Part. Beams **26**, 241-248 (2008).

188. L. Romagnani, J. Fuchs, M. Borghesi, P. Antici, P. Audebert, F. Ceccherini, T. Cowan, T. Grismayer, S. Kar, A. Macchi, P. Mora, G. Pretzler, A. Schiavi, T. Toncian, and O. Willi, *Dynamics of Electric Fields Driving the Laser Acceleration of Multi-MeV Protons,* Phys. Rev. Lett. **95**, 4 (2005).

189. S.J. Rose, *Calculations of radiative opacity of laser-produced plasmas,* J. Phys. B: At., Mol. Opt. Phys. **25**, 1667-1681 (1992).

190. A. Rousse, C. Rischel, and J.C. Gauthier, *Colloquium: Femtosecond x-ray crystallography,* Rev. Mod. Phys. **73**, 17-31 (2001).

191. W. Rozmus, V.T. Tikhonchuk, and R. Cauble, *A model of ultrashort laser pulse absorption in solid targets,* Phys. Plasmas **3**, 360-367 (1996).

192. H. Ruhl, T. Cowan, and J. Fuchs, *The generation of micro-fiducials in laser-accelerated proton flows, their imaging property of surface structures and application for the characterization of the flow,* Phys. Plasmas **11**, L17-L20 (2004).

193. G. Rybicki, and A.P. Lightman, *Radiative Processes in Astrophysics* (John Wiley & Sons, New York, 1979).

194. A. Saemann, and K. Eidmann, *Absolute calibration of a flat field spectrometer in the wavelength range 10-70 angstrom,* Rev. Sci. Instrum. **69**, 1949-1954 (1998).

195. A. Saemann, K. Eidmann, I.E. Golovkin, R.C. Mancini, E. Andersson, E. Forster, and K. Witte, *Isochoric heating of solid aluminum by ultrashort laser pulses focused on a tamped target,* Phys. Rev. Lett. **82**, 4843-4846 (1999).

196. E.G. Saiz, G. Gregori, D.O. Gericke, J. Vorberger, B. Barbrel, R.J. Clarke, R.R. Freeman, S.H. Glenzer, F.Y. Khattak, M. Koenig, O.L. Landen, D. Neely, P. Neumayer, M.M. Notley, A. Pelka, D. Price, M. Roth, M. Schollmeier, C. Spindloe, R.L. Weber, L. van Woerkom, K. Wünsch, and D. Riley, *Probing warm dense lithium by inelastic X-ray scattering,* Nat. Phys. **4**, 940-944 (2008).

197. D. Salzmann, *Atomic Physics in Hot Plasmas* (Oxford University Press, New York, Oxford, 1998).

198. M.I. Santala, M. Zepf, I. Watts, F.N. Beg, E. Clark, M. Tatarakis, K. Krushelnick, A.E. Dangor, T. Mccanny, I. Spencer, R.P. Singhal, K.W. Ledingham, S.C. Wilks, A.C. Machacek, J.S. Wark, R. Allott, R.J. Clarke, and P.A. Norreys, *Effect of the plasma density scale length on the direction of fast electrons in relativistic laser-solid interactions,* Phys. Rev. Lett. **84**, 1459-1462 (2000).

199. J.J. Santos, F. Amiranoff, S.D. Baton, L. Gremillet, M. Koenig, E. Martinolli, Le Gloahec, C. Rousseaux, D. Batani, A. Bernardinello, G. Greison, and T. Hall, *Fast electron transport in ultraintense laser pulse interaction with solid targets by rear-side self-radiation diagnostics,* Phys. Rev. Lett. **89**, 25001 (2002).

200. J.J. Santos, A. Debayle, P. Nicolai, V. Tikhonchuk, M. Manclossi, D. Batani, A. Guemnie-Tafo, J. Faure, V. Malka, and J.J. Honrubia, *Fast-electron transport and induced heating in aluminum foils,* Phys. Plasmas **14**, 103107 (2007).

201. R. Sauerbrey, J. Fure, S.P. Le Blanc, B. van Wonterghem, U. Teubner, and F.P. Schafer, *Reflectivity of laser-produced plasmas generated by a high-intensity ultrashort pulse,* Phys. Plasmas **1**, 1635-1642 (1994).

202. D. Saumon, G. Chabrier, D.J. Wagner, and X. Xie, *Modeling pressure-ionization of hydrogen in the context of astrophysics,* High Pressure Res. **16**, 331-343 (2000).

203. H. Schwoerer, S. Pfotenhauer, O. Jäckel, K.U. Amthor, B. Liesfeld, W. Ziegler, R. Sauerbrey, K. W. D Ledingham, and T. Esirkepov, *Laser-plasma acceleration of quasi-monoenergetic protons from microstructured targets,* Nature **439**, 445-448 (2006).

204. H. Schwoerer, J. Magill, and B. Beleites, *Lasers and Nuclei: Applications of Ultrahigh Intensity Lasers in Nuclear Science* (Springer, Berlin, 2006).

205. M.J. Seaton, Y. Yan, D. Mihalas, and A.K. Pradhan, *Opacities for stellar envelopes,* Mon. Not. R. Astron. Soc. **266**, 805-828 (1994).

206. Y. Sentoku, and A. Kemp, *Numerical methods for particle simulations at extreme densities and temperatures: Weighted particles, relativistic collisions and reduced currents,* J. Comput. Phys. **227**, 6846-6861 (2008).

207. Y. Sentoku, K. Mima, H. Ruhl, Y. Toyama, R. Kodama, and T.E. Cowan, *Laser light and hot electron micro focusing using a conical target,* Phys. Plasmas **11**, 3083 (2004).

208. Y. Shibata, K. Ishi, T. Takahashi, T. Kanai, M. Ikezawa, K. Takami, T. Matsuyama, K. Kobayashi, and Y. Fujita, *Observation of coherent transition radiation at millimeter and submillimeter wavelengths,* Phys. Rev. A **45**, R8340-R8343 (1992).

209. A. Siegman, *Lasers* (University Science Books, Mill Valley, CA, 1986).

210. R.F. Smith, J.H. Eggert, P. Celliers, A. Jankowski, T. Lorenz, S. Moon, M.J. Edwards, and G. Collins, *Laser driven quasi-isentropic compression experiments (ICE) for dynamically loading materials at high strain rates,* J. Phys. IV France **134**, 529-534 (2006).

211. R.A. Snavely, M.H. Key, S.P. Hatchett, T.E. Cowan, M. Roth, T.W. Phillips, M.A. Stoyer, E.A. Henry, T.C. Sangster, M.S. Singh, S.C. Wilks, A. MacKinnon, A. Offenberger, D.M. Pennington, K. Yasuike, A.B. Langdon, B.F. Lasinski, J. Johnson, M.D. Perry, and E.M. Campbell, *Intense high-energy proton beams from petawatt-laser irradiation of solids,* Phys. Rev. Lett. **85**, 2945-2948 (2000).

212. *SOHO, Solar and Heliospheric Observatory* http://sohowww.nascom.nasa.gov/gallery/images/cutaway00.html.

213. K. Sokolowski-Tinten, C. Blome, J. Blums, A. Cavalleri, C. Dietrich, A. Tarasevitch, I. Uschmann, E. Förster, M. Kammler, M. Horn-Von-Hoegen, and Dietrich Von Der Linde, *Femtosecond X-ray measurement of coherent lattice vibrations near the Lindemann stability limit,* Nature **422**, 287-289 (2003).

214. S. Sorge, A. Wierling, G. Ropke, W. Theobald, R. Sauerbrey, and T. Wilhein, *Diagnostics of a laser-induced dense plasma by hydrogen-like carbon spectra,* J. Phys. B: At., Mol. Opt. Phys. **33**, 2983-3000 (2000).

215. P. Sprangle, E. Esarey, J. Krall, and G. Joyce, *Propagation and Guiding of Intense Laser Pulses in Plasmas,* Phys. Rev. Lett. **69**, 2200-2203 (1992).

216. J. Stein, E. Fill, D. Habs, G. Pretzler, and K. Witte, *Hot electron diagnostics using X-rays and Cerenkov radiation,* Laser Part. Beams **22**, 315-321 (2004).

217. R.B. Stephens, R.A. Snavely, Y. Aglitskiy, F. Amiranoff, C. Andersen, D. Batani, S.D. Baton, T. Cowan, R.R. Freeman, T. Hall, S.P. Hatchett, J.M. Hill, M.H. Key, J.A. King, J.A. Koch, M. Koenig, A.J. Mackinnon, K.L. Lancaster, E. Martinolli, P. Norreys, E. Perelli-Cippo, M Rabec Le Gloahec, C. Rousseaux, J.J. Santos, and F. Scianitti, *K_alpha fluorescence measurement of relativistic electron transport in the context of fast ignition,* Phys. Rev. E **69**, 7 (2004).

218. J.C. Stewart, and K.D. Pyatt, *Lowering of ionization potentials in plasmas,* Astrophys. J. **144**, 1203 (1966).

219. D. Strickland, and G. Mourou, *Compression of amplified chirped optical pulses,* Opt. Commun. **56**, 219-221 (1985).

220. H.A. Sumeruk, S. Kneip, D.R. Symes, I.V. Churina, A.V. Belolipetski, G. Dyer, J. Landry, G. Bansal, A. Bernstein, T.D. Donnelly, A. Karmakar, A. Pukhov, and T. Ditmire, *Hot electron and x-ray production from intense laser irradiation of wavelength-scale polystyrene spheres,* Phys. Plasmas **14**, 62704 (2007).

221. S. Svanberg, *Some applications of ultrashort laser pulses in biology and medicine,* Meas. Sci. Technol. **12**, 1777-1783 (2001).

222. M. Tabak, J. Hammer, M.E. Glinsky, W.L. Kruer, S.C. Wilks, J. Woodworth, E.M. Campbell, M.D. Perry, and R.J. Mason, *Ignition and high gain with ultrapowerful lasers,* Phys. Plasmas **1**, 1626-1634 (1994).

223. N.A. Tahir, C. Deutsch, V.E. Fortov, V. Gryaznov, D. H. H Hoffmann, M. Kulish, I.V. Lomonosov, V. Mintsev, P. Ni, D. Nikolaev, A.R. Piriz, N. Shilkin, P. Spiller, A. Shutov, M. Temporal, V. Ternovoi, S. Udrea, and D. Varentsov, *Proposal for the Study of Thermophysical Properties of High-Energy-Density Matter Using Current and Future Heavy-Ion Accelerator Facilities at GSI Darmstadt,* Phys. Rev. Lett. **95**, 4 (2005).

224. T. Tajima, and G. Mourou, *Zettawatt-exawatt lasers and their applications in ultrastrong-field physics,* Phys. Rev. Spec. Top.-Acc. Beams **5**, 31301 (2002).

225. T. Takizuka, and H. Abe, *A Binary Collision Model for Plasma Simulation with a Particle Code,* J. Comput. Phys. **25**, 205-219 (1977).

226. T.H. Tan, G.H. McCall, and A.H. Williams, *Determination of laser intensity and hot-electron temperature from fastest ion velocity-measurement on laser-produced plasma,* Phys. Fluids **27**, 296-301 (1984).

227. M. Tatarakis, J.R. Davies, P. Lee, P.A. Norreys, N.G. Kassapakis, F.N. Beg, A.R. Bell, M.G. Haines, and A.E. Dangor, *Plasma formation on the front and rear of plastic targets due to high-intensity laser-generated fast electrons,* Phys. Rev. Lett. **81**, 999-1002 (1998).

228. A. Tauschwitz, J. Maruhn, D. Riley, G. Naz, F. Rosmej, and S. Borneis, *Quasi-isochoric ion beam heating using dynamic confinement in spherical geometry for X-ray scattering experiments in WDM regime,* High Energy Density Physics **3**, 371-378 (2007).

229. A. Tauschwitz, J.A. Maruhn, D. Riley, F.B. Rosmej, S. Borneis, A. Tauschwitz, and K. Witte, *Target design for studies of radiative properties in warm dense matter at GSI and FAIR - the WDM collaboration,* J. Phys.: Conf. Ser. **112**, 32074 (2008).

230. F. Tavella, Y. Nomura, L. Veisz, V. Pervak, A. Marcinkevicius, and F. Krausz, *Dispersion management for a sub-10-fs, 10 TW optical parametric chirped-pulse amplifier,* Opt. Lett. **32**, 2227-2229 (2007).

231. S. Ter-Avetisyan, M. Schnürer, P.V. Nickles, M. Kalashnikov, E. Risse, T. Sokollik, W. Sandner, A. Andreev, and V. Tikhonchuk, *Quasimonoenergetic*

Deuteron Bursts Produced by Ultraintense Laser Pulses, Phys. Rev. Lett. **96**, 4 (2006).

232. S. Ter-Avetisyan, M. Schnürer, T. Sokollik, P.V. Nickles, W. Sandner, H.R. Reiss, J. Stein, D. Habs, T. Nakamura, and K. Mima, *Proton acceleration in the electrostatic sheaths of hot electrons governed by strongly relativistic laser-absorption processes,* Phys. Rev. E **77**, 5 (2008).

233. U. Teubner, T. Missalla, I. Uschmann, E. Forster, W. Theobald, and C. Wulker, *X-ray spectra from highly ionized dense plasmas produced by ultrashort laser pulses,* Appl. Phys. B: Lasers Opt. **62**, 213-220 (1996).

234. *The European X-Ray Free Electron Laser Technical Design Report*, 646 (2007)
http://xfel.desy.de/tdr/tdr.

235. W. Theobald, K. Akli, R. Clarke, J.A. Delettrez, R.R. Freeman, S. Glenzer, J. Green, G. Gregori, R. Heathcote, N. Izumi, J.A. King, J.A. Koch, J. Kuba, K. Lancaster, A.J. Mackinnon, M. Key, C. Mileham, J. Myatt, D. Neely, P.A. Norreys, H.S. Park, J. Pasley, P. Patel, S.P. Regan, H. Sawada, R. Shepherd, R. Snavely, R.B. Stephens, C. Stoeckl, M. Storm, B. Zhang, and T.C. Sangster, *Hot surface ionic line emission and cold K-inner shell emission from petawatt-laser-irradiated Cu foil targets,* Phys. Plasmas **13**, 43102 (2006).

236. *Titan Leads the Way in Laser-Matter Science*
https://www-pls.llnl.gov/?url=science_and_technology-physics-titan.

237. T. Toncian, M. Borghesi, J. Fuchs, E. d'Humieres, P. Antici, P. Audebert, E. Brambrink, C.A. Cecchetti, A. Pipahl, L. Romagnani, and O. Willi, *Ultrafast laser-driven microlens to focus and energy-select mega-electron volt protons,* Science **312**, 410-413 (2006).

238. K.S. Trainor, *Construction of a wide-range tabular equation of state for copper,* J. Appl. Phys. **54**, 2372-2379 (1983).

239. A. Tremaine, J.B. Rosenzweig, S. Anderson, P. Frigola, M. Hogan, A. Murokh, C. Pellegrini, D.C. Nguyen, and R.L. Sheffield, *Observation of self-amplified spontaneous-emission-induced electron-beam microbunching using coherent transition radiation,* Phys. Rev. Lett. **81**, 5816-5819 (1998).

240. L. Wartski, S. Roland, J. Lasalle, M. Bolore, and G. Filippi, *Interference phenomenon in optical transition radiation and its application to particle beam diagnostics and multiple-scattering measurements,* J. Appl. Phys. **46**, 3644-3653 (1975).

241. E.S. Weibel, *Spontaneously growing transverse waves in a plasma due to an anisotropic velocity distribution,* Phys. Rev. Lett. **2**, 83-84 (1959).

242. K. Widmann, G. Guethlein, M.E. Foord, R.C. Cauble, F.G. Patterson, D.F. Price, F.J. Rogers, P.T. Springer, R.E. Stewart, A. Ng, T. Ao, and A. Forsman, *Interferometric investigation of femtosecond laser-heated expanded states,* Phys. Plasmas **8**, 3869-3872 (2001).

243. S.C. Wilks, W.L. Kruer, M. Tabak, and A.B. Langdon, *Absorption of Ultra-Intense Laser Pulses,* Phys. Rev. Lett. **69**, 1383-1386 (1992).

244. N.C. Woolsey, B.A. Hammel, C.J. Keane, C.A. Back, J.C. Moreno, J.K. Nash, A. Calisti, C. Mosse, R. Stamm, B. Talin, A. Asfaw, L.S. Klein, and R.W. Lee, *Competing effects of collisional ionization and radiative cooling in inertially confined plasmas,* Phys. Rev. E **57**, 4650-4662 (1998).

245. N.C. Woolsey, D. Riley, and E. Nardi, *Kilovolt x-ray scattering from a plasma,* Rev. Sci. Instrum. **69**, 418-424 (1998).

246. T.Y. Yang, W.L. Kruer, R.M. More, and A.B. Langdon, *Absorption of laser light in overdense plasmas by sheath inverse bremsstrahlung,* Phys. Plasmas **2**, 3146-3154 (1995).

247. H. Yoneda, H. Morikami, K. Ueda, and R. More, *Ultra-short pulse laser pump-probe experiments for investigation of warm dense plasmas,* J. Quant. Spectrosc. Radiat. Transfer **99**, 690-696 (2006).

248. L.C. Yuan, C.L. Wang, and S. Prunster, *X-ray transition radiation applied to the detection of superhigh-energy particles,* Phys. Rev. Lett. **23**, 496 (1969).

249. U. Zastrau, C. Fortmann, R.R. Fäustlin, L.F. Cao, T. Döppner, S. Düsterer, S.H. Glenzer, G. Gregori, T. Laarmann, H.J. Lee, A. Przystawik, P. Radcliffe, H. Reinholz, G. Röpke, R. Thiele, J. Tiggesbäumker, N.X. Truong, S. Toleikis, I. Uschmann, A. Wierling, T. Tschentscher, E. Förster, and R. Redmer, *Bremsstrahlung and line spectroscopy of warm dense aluminum plasma heated by xuv free-electron-laser radiation,* Phys. Rev. E **78**, 5 (2008).

250. Y.B. Zel‘dovich, and Y.P. Raizer, *Physics of Shock Waves and High-Temperature Hydrodynamic Phenomena*, 944 (2002).

251. J. Zheng, K.A. Tanaka, T. Miyakoshi, Y. Kitagawa, R. Kodama, T. Kurahashi, and T. Yamanaka, *Spectrum of transition radiation from hot electrons generated in ultra-intense laser plasma interaction,* Phys. Plasmas **9**, 3610-3616 (2002).

252. J. Zheng, K.A. Tanaka, T. Miyakoshi, Y. Kitagawa, R. Kodama, T. Kurahashi, and T. Yamanaka, *Theoretical study of transition radiation from hot electrons generated in the laser-solid interaction,* Phys. Plasmas **10**, 2994-3003 (2003).

253. J. Zheng, K.A. Tanaka, T. Sato, T. Yabuuchi, T. Kurahashi, Y. Kitagawa, R. Kodama, T. Norimatsu, and T. Yamanaka, *Study of hot electrons by measurement of optical emission from the rear surface of a metallic foil irradiated with ultraintense laser pulse,* Phys. Rev. Lett. **92**, 165001 (2004).

254. J.F. Ziegler, J.P. Biersack, and U. Littmark, *The Stopping and Range of Ions in Solids* (1985).

Acknowledgements

At this point, I would like to thank all the people who have supported me in the recent years.

I am very grateful to Prof. Oswald Willi who has made this work possible by giving me the opportunity to join his group at the Institute for Laser and Plasmaphysics at the Heinrich-Heine-University Düsseldorf. My special thanks to Prof. Georg Pretzler who has contributed to this work with many fruitful scientific discussions. Many thanks also to our group in Düsseldorf, in particular Felix Brandl, Mirela Cerchez, Thomas Fischer, Dirk Hemmers, Bernhard Hidding, Ralph Jung, and Ariane Pipahl. The support of Prof. Alexander Pukhov, Anupam Karmakar, and Sergey Kiselev from the Institute for Theoretical Physics with PIC simulations is acknowledged.

I thank Prof. Todd Ditmire for giving me the chance to join his group at the Texas Center for High Intensity Laser Science at the University of Texas at Austin for a one year research stay. Special thanks to my office mate Aaron Bernstein, Byoung Ick Cho and Gilliss Dyer for valuable discussions and the close collaboration during the experiments.

Special thanks also to Prof. Nathalie Renard-Le Galloudec from the University of Nevada at Reno for providing the cone targets and contributing her expertise in advanced target manufacturing techniques.

I thank Marco Borghesi and his group from Queen’s University Belfast for the productive collaboration during our experiments at the Rutherford Appleton Laboratory.

I would like to thank Prof. Steven Rose from Imperial College London and Richard Lee from Lawrence Livermore National Laboratory for sharing their expertise in radiative properties of dense plasmas.

I gratefully acknowledge the financial support of the DFG with a research fellowship and within the SFB Transregio 18.

Finally, I thank my wife Stephanie and my daughters Lena and Merle who were always by my side and who gave me strength after long working days.

Published works

1. A. P. Higginbotham, O. Semonin, S. Bruce, C. Chan, M. Maindi, T. D. Donnelly, M. Maurer, W. Bang, I. Churina, J. Osterholz, I. Kim, A. C. Bernstein, and T. Ditmire
   Generation of Mie size microdroplet aerosols with applications in laser-driven fusion experiments
   Review of Scientific Instruments **80**, 063503 (2009)

2. N. Renard-Le Galloudec, E. D'Humieres, B. I. Cho, J. Osterholz, Y. Sentoku, and T. Ditmire
   Guiding, focusing, and collimated transport of hot electrons in a canal in the extended tip of cone targets
   Phys. Rev. Lett. **102**, 205003 (2009)

3. F. Brandl, B. Hidding, J. Osterholz, D. Hemmers, A. Karmakar, A. Pukhov, and G. Pretzler
   Directed Acceleration of Electrons from a Solid Surface by sub-10-fs Laser Pulses
   Phys. Rev. Lett. **102**, 195001 (2009)

4. L. Romagnani, M. Borghesi, C.A. Cecchetti, S. Kar, P. Antici, P. Audebert, S. Bandhoupadjay, F. Ceccherini, T. Cowan, J. Fuchs, M. Galimberti, L.A. Gizzi, T. Grismayer, R. Heathcote, R. Jung, T.V. Liseykina, A. Macchi, P. Mora, D. Neely, M. Notley, J. Osterholz, C.A. Pipahl, G. Pretzler, A. Schiavi, G. Schurtz, T. Toncian, P.A. Wilson, and O. Willi
   Proton probing measurement of electric and magnetic fields generated by ns and ps laser-matter interactions
   Laser and Particle Beams **26**, 241 (2008)

5. J. Osterholz, F. Brandl, M. Cerchez, T. Fischer, D. Hemmers, B. Hidding, A. Pipahl, G. Pretzler, S. Rose, and O. Willi
   Extreme ultraviolet emission from dense plasmas generated with sub-10-fs laser pulses
   Phys. Plasmas **15**, 103301 (2008)

6. N. Renard-Le Galloudec, B. I. Cho, J. Osterholz, and T. Ditmire
   Controlled reproducible alignment of cone targets and mitigation of preplasma in high intensity laser interactions
   Rev. Sci. Instr. **79**, 083506 (2008)

7. G. M. Dyer, A. C. Bernstein, B. I. Cho, J. Osterholz, W. Grigsby, A. Dalton, R. Shepherd, Y. Ping, H. Chen, K. Widmann, and T. Ditmire
Equation-of-state measurement of dense plasmas heated with fast protons
Phys. Rev. Lett. **101**, 015002 (2008)

8. M. Cerchez, R. Jung, J. Osterholz, T. Toncian, O. Willi, P. Mulser, and H. Ruhl
Absorption of ultrashort laser pulses in strongly overdense targets
Phys. Rev. Lett. **100**, 245001 (2008)

9. M. Borghesi, C. A. Cecchetti, T. Toncian, J. Fuchs, L. Romagnani, S. Kar, P. A. Wilson, P. Antici, P. Audebert, E. Brambrink, A. Pipahl, M. Amin, R. Jung, J. Osterholz, O. Willi, W. Nazarov, R. J. Clarke, M. Notley, D. Neely, P. Mora, T. Grismayer, G. Schurtz, A. Schiavi, Y. Sentoku, E. d'Humieres
Laser-driven proton beams: acceleration mechanism, beam optimization and radiographic applications
IEEE Transactions of Plasma Science **36**, 1833 (2008)

10. B. I. Cho, J. Osterholz, N. Renard-Le Galloudec, A. C. Bernstein, G. Dyer, and T. Ditmire
Study of hot electron transport in foil, wedge and cone targets irradiated with ultraintense laser pulses
J. Opt. Soc. Am. B **25**, B50 (2008)

11. S. Kar, M. Borghesi, C. A. Cecchetti, L. Romagnani, F. Ceccherini, T. V. Liseykina, A. Macchi, R. Jung, J. Osterholz, O. Willi, L. A. Gizzi, M. Galimberti, A. Schiavi, and R. Heathcote
Dynamics of charge-displacement channeling in intense laser-plasma interactions
New Journal of Physics **9**, 402 (2007)

12. M. Borghesi, S. Kar, L. Romagnani, T. Toncian, P. Antici, P. Audebert, E. Brambrink, F. Ceccherini, C. A. Cecchetti, J. Fuchs, M. Galimberti, L. A. Gizzi, T. Grismayer, T. Lyseikina, R. Jung, A. Macchi, P. Mora, J. Osterholz, A. Schiavi, O. Willi
Impulsive electric fields driven by high-intensity laser matter interactions
Laser and Particle Beams **25**, 161-167 (2007)

13. M. Borghesi, S. Kar, L. Romagnani, C. A. Cecchetti, P. Antici, P. Audebert, J. Fuchs, R. Jung, J. Osterholz, T. Toncian, O. Willi, M. Galimberti, L. A. Gizzi, F. Ceccherini, T. V. Liseykina, A. Macchi, T. Grismayer, P. Mora, and A. Schiavi
    MeV proton sources for plasma dynamics investigations on ps timescales
    International Journal of Modern Physics B **21**, 300-311 (2007)

14. J. Osterholz, F. Brandl, T. Fischer, D. Hemmers, M. Cerchez, G. Pretzler, O. Willi, and S. J. Rose
    Production of Dense Plasmas with sub-10-fs Laser Pulses
    Phys. Rev. Lett. **96**, 085002 (2006)

15. R. Jung, J. Osterholz, K. Löwenbrück, S. Kiselev, G. Pretzler, A. Pukhov, O. Willi, S. Kar, M. Borghesi, W. Nazarov, S. Karsch, R. Clarke, and D. Neely
    Study of electron beam propagation through pre-ionized dense foam plasmas
    Phys. Rev. Lett. **94**, 195001 (2005)

16. A. Terenji, S. Willmann, J. Osterholz, P. Hering, and H. J. Schwarzmaier
    Measurement of the coagulation dynamic of bovine liver using the modified microscopic Beer-Lambert law
    Las. Surg. Med. **36**, 365 (2005)

17. S. Willmann, A. Terenji, J. Osterholz, J. Meister, P. Hering, and H. J. Schwarzmaier
    Small Volume Frequency-Domain Oximetry: Phantom Experiments and first in vivo Results
    J. Biomed. Opt. **8**, 618 (2003)

18. S. Willmann, A. Terenji, J. Osterholz, H. J. Schwarzmaier, and P. Hering
    Absolute absorber quantification in turbid media at small source-detector separations
    Appl. Phys. B **74**, 589 (2002)